TECHNISCHE
UNIVERSITÄT
WIEN

DISSERTATION

Ramsey Spectroscopy of Gravitationally Bound Quantum States of Ultracold Neutrons

Ausgeführt zum Zwecke der Erlangung des akademischen Grades eines Doktors der technischen Wissenschaften unter Leitung von

Univ. Prof. Dipl.-Phys. Dr. rer. nat. Hartmut Abele
Dipl.-Phys. Dr. rer. nat. Tobias Jenke
E 141 - Atominstitut

eingereicht an der Technischen Universität Wien
Fakultät für Physik

von

Dipl.-Ing. Tobias Wilhelm Rechberger

Matrikelnummer 00626129
Stiegengasse 9/19, A-1060 Wien

Wien, am 24. Oktober 2018   Tobias Rechberger

Kurzfassung

Das Standardmodell der Teilchenphysik beschreibt erfolgreich drei der vier bekannten Grundkräfte der Physik. Lediglich die vergleichsweise schwache Gravitation entzieht sich bisher einer quantenmechanischen Beschreibung, sowie einer Einbindung in das Standardmodell. Obwohl die allgemeine Relativitätstheorie als Beschreibung der Gravitation und als Eckpfeiler moderner Kosmologie äußerst erfolgreich ist, werfen starke Hinweise auf die Existenz dunkler Energie und dunkler Materie neue Fragen auf.

Neutronen bieten sich auf Grund ihrer geringen elektrischen Polarisierbarkeit und ihrer verschwindenden elektrischen Ladung an, um die Gravitation bei kleinen Abständen zu testen: Im Gravitationsfeld der Erde können ultrakalte Neutronen gebundene Zustände annehmen. Diese Zustände sind quantenmechanischer Natur und ihre Eigenenergien nicht äquidistant. Daher lassen sie den Einsatz spektroskopischer Methoden zu. Dies macht sich das qBOUNCE Experiment zu Nutze, um die Eigenenergien der ultrakalten Neutronen sehr genau zu vermessen. In bisherigen qBOUNCE Experimenten wurden Rabi-artige spektroskopische Experimente realisiert, was zum Beispiel zu Grenzen auf Dark Energy und Dark Matter Modelle führte — diese würden die Eigenenergien des Neutrons beeinflussen.

Diese Arbeit beschreibt den logischen Schritt um die Präzision der qBOUNCE Experimente weiter zu erhöhen: Die erstmalige Realisierung von Norman F. Ramseys Methode separierter oszillierender Felder zur Anwendung auf quantenmechanische Zustände der Neutronen im Gravitationsfeld der Erde. Gleichzeitig stellt das Experiment (nach Kenntnis des Autors) die erste Umsetzung von Ramsey's Methode dar, welche nicht auf elektromagnetischer Wechselwirkung (sondern auf mechanischen Oszillationen) beruht.

Aufgrund der Erweiterung von einem Rabi-artigen auf einen Ramsey-artigen Experimentaufbau und dem damit einhergehenden erhöhten Platzbedarf, wurde dafür ein vollkommen neues Instrument realisiert. Das Ramsey-Experiment mit fünf aneinandergereihten Neutronenspiegeln wurde geplant, gebaut und in Betrieb genommen. Es gelang der erste Nachweis von Ramseys Resonanzmethode mit gravitativ gebundenen, ultrakalten Neutronen und mechanisch oszillierenden Neutronenspiegeln.

Abstract

The Standard Model of particle physics successfully describes three of the four fundamental forces in physics. Only gravitation, which is comparatively weak, eludes a quantum mechanical description as well as an embedding into the Standard Model. Although general relativity is a successful description of gravitation and a cornerstone of modern cosmology, new questions arise by strong indications of the existence of dark energy and dark matter.

Due to their small electrical polarisability and their vanishing electrical charge, neutrons represent excellent test particles to test gravitation at short distances: Ultracold neutrons can form bound states in the gravity potential of the Earth. These states are formed due to quantum mechanics and are non-equidistant. Therefore, spectroscopic methods are applicable. The qBOUNCE experiment takes advantage of this feature to measure the eigenenergies of the ultracold neutrons very precisely. Rabi-like spectroscopic methods have been realised in previous qBOUNCE experiments, which lead for example to limits on dark energy and dark matter models that would alter the eigenenergies of the neutrons.

This thesis presents the next logical step to further increase the precision of qBOUNCE experiments: The realisation of Norman F. Ramsey's method of separated oscillatory fields applied to quantum mechanical states of neutrons in the gravitational field of the Earth. In addition, the experiment presented is (to the author's best knowledge) the first realisation of Ramsey's method that is not based on electromagnetic interaction but purely on mechanical oscillations.

Due to the extension from a Rabi-like to a Ramsey-like setup and the increased required space, a whole new instrument was developed. The Ramsey experiment, consisting of five aligned neutron mirrors, was planned, constructed, and put into operation. The first proof of Ramsey's method with gravitationally bound, ultracold neutrons and mechanically oscillating neutron mirrors succeeded.

Contents

Contents

Part I

Introduction

1. Standard Model and Gravitation

1.1. Overview and Thesis Outline

With the Standard Model of particle physics indisputably being a tremendous success of the twentieth century and the discovery of the Higgs boson in 2012 recently validating the Standard Model, there are still plenty of open questions in practically all fields of physics. One big question is whether a Grand Unified Theory exists, where the electromagnetic, the weak, and the strong interaction can be explained by manifestations of a single underlying force. Another problem is the integration of gravitation into such theories. The driving factor behind the accelerated expansion of the universe remains yet another mystery.

As gravitation plays a major role in several of those open questions, it is subject to many experimental tests, from astrophysical scales down to table top experiments. At small distances (tens of micrometer), qBOUNCE is a table top experiment probing gravity. The qBOUNCE experiment represents a unique ***q***uantum mechanical system, whose eigenenergies are solely defined by natural constants, and the Earth's gravitational acceleration. Ultracold neutrons, which **Bounce** along flat surfaces, are ideal test particles for gravity because they represent a systematically advantageous system: The neutron's electrical neutrality and its small electrical polarisability let it widely bypass any electromagnetic perturbations. Together with spectroscopic methods that are well developed and understood, this system of bound ultracold neutrons can test Newtonian gravity or cosmological models. Although spectroscopic methods are usually used by means of electromagnetic radiation, qBOUNCE exhibits **spectroscopy by means of mechanical oscillations**. Several different experiments have previously been realised within qBOUNCE, in the form of Rabi-type setups and the measurement of the Quantum Bouncing Ball (**Jenke** (2008, 2011); **Cronenberg** (2016); **Thalhammer** (2019)).

The goal of this thesis was the construction of an advanced setup in the form of a Ramsey-type experiment. Ramsey spectroscopy with bouncing ultracold neutrons has never been realised before. With such a setup, the precision for testing Newtonian gravity at small distances increases in comparison to previously realised methods. However, in the author's opinion, a mechanically controlled, coherent superposition of energy eigenstates of a single neutron over the distance of more than 30 cm, bouncing along an experiment of the length of almost one metre, shows significant motivation for the experiment on its own.

The implementation of Ramsey spectroscopy lead to the planning and con-

struction of a whole new instrument, within which the new experiment was set up, commissioned and put into initial operation. The planning, construction, and many systematic tests took place at the Atominstitut of the TU Wien. The final setup was installed and started running at the Institut Laue-Langevin in Grenoble, France, during the years 2016 and 2017, and is operating (at experimental beamtimes) until at least the end of 2018.

This thesis is arranged in four parts. In the present introductory part, a motivation for qBOUNCE experiments is given in the face of the Standard Model of particle physics, gravity, dark energy, and dark matter, which are presented in a qualitative overview. A brief summary of ultracold neutrons as well as an overview of qBOUNCE and Gravity Resonance Spectroscopy (GRS) are shown in the subsequent sections.
Part II summarises theoretical aspects of the experiment, as well as a simulation for the classical expectations of selected measurement schemes. In part III, the planning and the technical realisation of the experiment as well as results are presented, before part IV concludes with a summary and an outlook.

The aim of the following sections 1.2 and 1.3 is to motivate the experiment presented in this thesis by providing examples from particle physics or for dark energy and dark matter models, which are in principle verifiable by qBOUNCE. A brief and qualitative overview about the currently most established theories of particle physics (section 1.2), gravitation, and cosmology (section 1.3) is given.

1.2. Standard Model of Particle Physics

Overview

The Standard Model of particle physics is extremely successful in describing the electromagnetic, the weak, and the strong interaction in the frame of a quantum field theory. It features 17 elementary particles, from which all (ordinary) matter and forces (except gravity) can be generated: Six quarks, six leptons, four vector gauge bosons and one scalar boson (the Higgs particle). The underlying theory to those particles is an $SU(3) \otimes SU(2) \otimes U(1)$ local symmetrical gauge quantum field theory.
The $SU(3)$ gauge group describes the strong interaction between quarks and is called quantum chromodynamics, whereas the $SU(2) \otimes U(1)$ describes the electroweak theory — the unification of electromagnetic and weak interactions. Below an energy scale of around $250\,\text{GeV}$, spontaneous symmetry breaking due to the Higgs mechanism leads to the production of $W^{\pm}$ and Z^0 bosons (mediators of the weak interaction) and photons (mediator of electromagnetism). The weak interaction is also the reason why the free neutron is not stable and decays via β^- decay. By flavour change of one down quark to an up quark, the neutron decays into a proton, an electron and an electron antineutrino. The inverse process of β^+ decay is suppressed for free protons, because the neutron's mass is greater

than the mass of the proton.

Despite its predominant consistency with experiments, there also are problems with the Standard Model: Seemingly arbitrary coupling constants, the baryon asymmetry of the universe (in favour for matter over anti-matter), absent neutrino masses, or the fact that dark energy, dark matter, or quantum gravity are not part of the model (**Patrignani and Group** (2016)). All these issues lead to the justified assumption that the Standard Model of particle physics is either not complete, or there is another underlying theory yet to discover. Currently, string theoretical models are an important part of research in such a direction, although increasingly accurate cosmological observations and model building will be an important factor in the search for a Grand Unification (**Patrignani and Group** (2016)).

Beyond the Standard Model

In (supersymmetric) string theoretical approaches for a unified theory, more than three spatial dimensions are necessary, with a minimum of ten. The solution to comply with observations is that extra dimensions are compactified, in the sense of being curled or rolled up. Depending on the size and dimension of the compactified strings, this leads to a deviation of the gravitational constant G, at distances smaller than the compactification radius. In general, theories of this type can be described by adding a Yukawa term to the Newtonian gravitational potential for two masses M and m:

$$V(r) = -G\frac{Mm}{r}\left(1 - \alpha\,e^{-r/\lambda}\right),\qquad(1.1)$$

with strength factor α, and range λ of the hypothetical force. In such a way, best limits at the time on non-Newtonian forces have already set by the gravitationally bound states of ultracold neutrons above a neutron mirror (**Abele et al.** (2003); **Nesvizhevsky and Protasov** (2004)).

Other such deviations from Newton's law have been proposed for supersymmetric large extra dimensions (SLEDs), which could account for dark energy (which will be the topic of section 1.3). In theories of this kind, the size of the extra dimensions is in the order of micrometer (**Callin and Burgess** (2005)) — in the same range as the energy levels of gravitationally bound ultracold neutrons.

In summary, different theories altering the Newtonian gravitational potential are a good motivation to increase the sensitivity of qBOUNCE experiments, to test gravity at small distances.

1.3. Gravitation, Dark Energy and Dark Matter

Overview

Gravitation is described by the theory of general relativity (GR), developed by Albert Einstein. Just as the Standard Model of particle physics in 2012 with the

discovery of the Higgs boson (**The ATLAS Collaboration** (2012)), Einstein's theory was once again confirmed with first observations of gravitational waves in 2015 and 2016 — about one hundred years after their prediction (**LIGO and Virgo Collaboration et al.** (2016)). This gives rise for a whole new field of astronomy, complementary to electromagnetic observations. Although there are indications that general relativity is incomplete (for example due to the lack of a quantum mechanical description), no measurement yet yielded results that deviate significantly from the predictions of general relativity. Justified motivations for some sort of quantum gravity are for example the search for unified theories, or attempts to understand the thermodynamics of black holes.

The development of GR also marked the start of increasing cosmological considerations. Applying GR to the universe and assuming only two boundary conditions (isotropy and homogeneity), the ΛCDM model originates. The lambda **C**old **D**ark **M**atter model[1], sometimes referred to as Standard Cosmology, is a widely used cosmology model that involves a Big Bang. It contains a cosmological constant Λ, initially added to general relativity by Einstein to counteract the contraction through gravity, in order to describe a static universe.

Two terms have occurred excessively in particle physics and cosmology over past decades: *dark matter* and *dark energy*. At the time Einstein published the theory of general relativity in 1915, the (accelerated) expansion of the universe was not yet discovered, and neither was the **C**osmic **M**icrowave **B**ackground (CMB). The CMB corresponds to a black body radiation at around 2.7 K, being measurable from all directions of the sky.[2] Only when looking at deviations in the order of 10^{-5}, the radiation is not perfectly isotropic and homogeneous anymore. On this scale, the CMB map of the sky reveals precious information about the composition as well as the history of the universe. By studying the angular power spectrum of the CMB, the energy budget of the universe can be extracted. Figure 1.1 shows data measured by the Planck telescope (**Adam et al.** (2016)). The two largest fraction are represented by dark energy and dark matter, and baryonic matter accounts only for 4.9 % of the total budget. These results are also confirmed through complementary observations (see e. g. **Clowe et al.** (2006) for dark matter detection via collision of galaxy clusters or **Kwan et al.** (2017) for matter constraints via galaxy clustering and lensing).

The largest fraction of the energy budget, **dark energy**, is often connected to the cosmological constant Λ in general relativity. Without Λ, general relativity

---

[1]Cold refers to non-relativistic particles, whereas hot dark matter implies relativistic particles involved. Cold dark matter is mostly preferred due to simulations, where hot dark matter is not able to explain the full amount of dark matter estimated in the universe.

[2]The CMB's origin dates back to around 400 000 years after the Big Bang to the phase of recombination, when the universe became transparent for photons, as ions and free electrons formed neutral atoms. Before that, photons Thomson scattered with free electrons and the photons' mean free path was smaller than the expansion rate of the universe. Thus, the CMB looks back to this decoupling of photons and baryons, the farthest possible in terms of electromagnetic radiation.
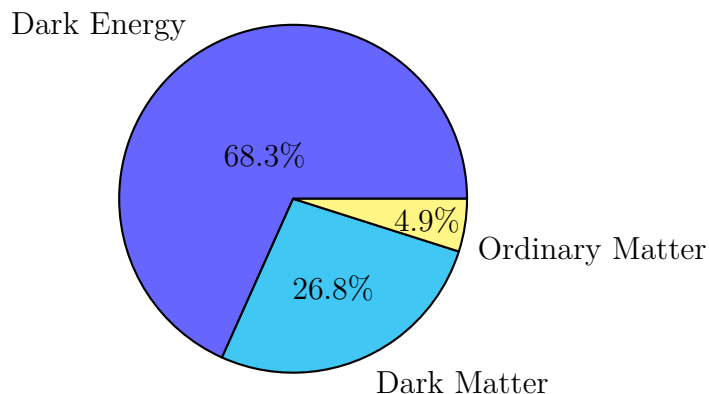
[3] `http://sci.esa.int/planck/51557-planck-new-cosmic-recipe/`

Figure 1.1.: Currently most precise numbers for the energy budget in the universe, according to the Planck Collaboration[3].

is rigorously tested (see e. g. **Will** (1993)). The idea of equating the curvature of space-time with the energy-momentum tensor of any matter or radiation, has proven itself to be most accurate description of gravity until today. With the cosmological constant Λ, the Einstein equations read

$$R_{\mu\nu} - \frac{1}{2}g_{\mu\nu}R + \Lambda g_{\mu\nu} = \frac{8\pi G}{c^4}T_{\mu\nu} \,, \tag{1.2}$$

where the Ricci tensor $R_{\mu\nu}$ describes the curvature of space-time, the Ricci scalar R stands for the deviation from Euclidean space, $g_{\mu\nu}$ is the metric tensor, G is Newton's gravitational constant, c the speed of light, and $T_{\mu\nu}$ is the symmetric energy-momentum tensor. The terms on the left-hand side, $R_{\mu\nu}$ and R, are solely dependent on the metric $g_{\mu\nu}$ (describing the geometrical properties of space-time), $T_{\mu\nu}$ on the right-hand side describes all matter. While Einstein originally thought of creating a static universe, Λ receives many different interpretations nowadays. Many theories introduce new fields or particles (e. g. quintessence theories or scalar fields with screening mechanisms), or on the other hand modify gravity itsef (e. g. Einstein-Cartan theory or brane-world models of string theory). Broader reviews of different origins of the cosmological constant are given for example in **Joyce et al.** (2015), **Copeland et al.** (2006), or **Clifton et al.** (2012) (focussed more on modified gravity).

With different theories at hand, the only way to proceed is to test them experimentally. Astrophysical observations can often set upper or lower bounds on parameters of hypothetical particles or fields. Within terrestrial experiments, besides for example torsion pendulum (**Kapner et al.** (2007); **Brax and Fichet** (2018)), atom interferometer (e. g. **Brax and Davis** (2016)), or parallel plate experiments (**Almasi et al.** (2015)), qBOUNCE is sensitive to a range of dark energy candidates. Some of them are covered in the following section.

Selected Dark Energy Models

Like the Higgs mechanism is giving mass to fundamental particles, it is possible that dark energy is a scalar field with long range coupling mechanism. But to conform with experimental tests, these long range forces have to be suppressed by screening mechanisms. The coupling of the scalar field to matter can be made dependent on different parameters, all yielding different theories. This screening mechanism would explain why no terrestrial or orbiting experiment up to now has found significant hints for dark energy.

Tests with gravitationally bound neutrons are of special interest because of their ability to test distance ranges inaccessible by astrophysics, where few experiments at all are able to search (**Baeßler et al.** (2007); **Abele et al.** (2010)).

Chameleon

For the chameleon, the mass of the scalar field depends on the local matter density. On Earth, the interaction range is of the order of one millimetre, whereas in the solar system it increases to 10^1–10^4 ua (**Khoury and Weltman** (2004))[4]. Because of the dependence on matter, a chameleon would be detectable through violations of the equivalence principle, however due to the screening mechanism, these violations would only show in space, but not on or around the Earth.

An effective potential for the chameleon field ϕ can be written in the form

$$V_{\text{eff}}(\phi) = V(\phi) + \rho e^{\frac{\beta\phi}{M_{Pl}}} \ , \tag{1.3}$$

with $V(\phi) = M^{4+n}\phi^{-n}$, a constant n, mass of the chameleon M, the reduced Planck mass M_{Pl}, energy density ρ, and coupling constant β. With a high background density of matter, the chameleon becomes heavier and more suppressed. In the cosmos, however, the chameleon can mediate a long-range force. The **screening mechanism** therefore manifests **via the changing mass of the chameleon field**.
Due to the thin-shell effect, the force between the Sun and the planets is also rather small. For large objects with constant ϕ within, only a small outer layer contributes to the force mediated by the chameleon, because of its proportionality to $\vec{\nabla}\phi$. The fraction of the thin shell to the actual size of the object is small (e. g. **Mota and Shaw** (2007)). It is due to this effect, that astronomical observations cannot rule out larger parameter spaces of the chameleon theory.

For the potential shown in equation (1.3), qBOUNCE could already excluded chameleons with two different setups: A single region damped Rabi-like system, and a full three region Rabi setup (a description follows in section 3.3.1).
In the one-part setup, for $2 \leq n \leq 4$, $\beta > 5.8 \times 10^8$ was measured at 95% confidence level (**Jenke et al.** (2014)). A neutron mirror-absorber setup was used, realising damped Rabi oscillations of gravitationally bound ultracold neutrons

---

[4]One astronomical unit (ua), is defined as the distance between Earth and Sun, around 150 million kilometres.
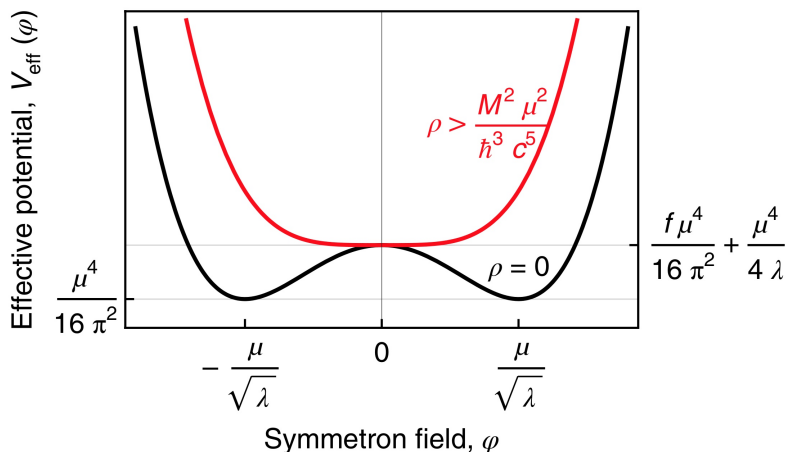
Figure 1.2.: Effective symmetron potential in matter (red) and in vacuum (mass density $\rho = 0$). The potential has two minima in vacuum, at finite values of the effective potential due to vacuum fluctuations. Here, M is a coupling parameter to matter, $\lambda > 0$ is a self interaction parameter, and μ is the symmetron mass. Image taken from **Cronenberg et al.** (2018), 3, fig. 3.

(**Jenke** (2011)). For the three part setup, the limits were improved by around two orders of magnitude and yielded $\beta > 9.1 \times 10^6$ for $n = 5$ (**Cronenberg** (2016)).

At the moment, the most stringent limits for the chameleon come from atom interferometry (**Jaffe et al.** (2017); **Banahene-Sabulsky** (2018)). For the role of the chameleon in Einstein-Cartan gravity with torsion, see **Ivanov and Wellenzohn** (2016a,b).

Symmetron

Another hypothetical particle that can mediate long-range forces in space, but still remains undetected in terrestrial or orbital gravity tests, is the symmetron. Here, the **screening mechanism** is realised **via the coupling to matter**, which vanishes for a sufficiently high ambient matter density (**Hinterbichler and Khoury** (2010)). This leads to a $\phi \to -\phi$ symmetry, just like in the Higgs potential, and gives rise to the particle's name. The effective symmetron potential is shown in figure 1.2. In matter for example (red, upper curve), the symmetry potential has its minimum at zero field. In vacuum, however, the effective symmetron potential is symmetry broken, and exhibits two minima. This Mexican hat potential exhibits a non-vanishing vacuum expectation value, as vacuum fluctuations lift the effective potential to a finite value. Thus, the symmetron is a dark energy candidate, possibly responsible for the expansion of the universe.

Recently, stringent constraints have been set on the existence of the symmetron for a large parameter space by qBOUNCE (**Cronenberg et al.** (2018)). In a

full Rabi-like neutron mirror setup (compare section 3.3.1), transitions between energy states of gravitationally bound neutrons have been examined, and their energy difference measured. Symmetrons would change the gravitational potential and therefore change the individual eigenenergies of the neutrons. Such an effect, however, has not been observed, up to a resolution of $\Delta E = 2 \times 10^{-15}$ eV, resulting in the limits presented.

Exact analytical solutions for the symmetron field in one- and two-mirror systems have been presented in **Brax and Pitschmann** (2018).

Dilaton

The dilaton field occurs naturally in string theory. When trying to unify all fundamental forces in physics, most unified theories require a fundamental spin-zero field — the dilaton field. The dilaton can act as a gravitational scalar field with finite-range forces between objects (**Fujii** (2003)). In space, it acts as a massless field, being able to account for dark energy. As with the chameleon, the screening mechanism is realised via coupling to matter. Besides being a candidate for dark energy, the dilaton represents an interesting candidate to proving string theories with gravity experiments (see also section 1.2).

Dark Matter

Starting with **Zwicky** (1933) where first strong evidence of dark matter was reported[5], evidence for dark matter is well founded today. Flattened galaxy rotation curves (**Corbelli and Salucci** (2000)), analysis of the CMB (**Adam et al.** (2016)), or colliding clusters of galaxies (**Clowe et al.** (2004)), all support the existence of dark matter.

However, it is not clear how dark matter can be explained. That dark matter is some form of baryonic matter ("MACHOs", **M**assive **A**strophysical **C**ompact **H**alo **O**bjects), is strongly rejected by microlensing measurements by the EROS Collaboration, setting an upper limit to the fraction of halo mass of $8\,\%$ (**Tisserand et al.** (2007)). MOND (Modified Newtonian Gravity) theories usually cannot adequately explain the bullet cluster, the colliding clusters of galaxies mentioned above. Other than the restriction to non-baryonic matter, there are not many other restrictions to possible dark matter candidates, besides that their interaction to ordinary matter must be very small. Jim Peebles presented a candidate for cold dark matter in the form of massive, weakly interacting particles (WIMPs, **Peebles** (1982)).

---

[5]Fritz Zwicky used the virial theorem to estimate the relation between dark and luminous matter in the Coma cluster of galaxies to be very large—in favour of dark matter. Relating the total kinetic energy T of gravitationally bound stars in a galaxy, with the galaxy's total potential energy U by $2T = -U$. With estimates of $T \sim Mv^2/2$ and $U \sim GM^2/R$, one obtains $M \sim v^2R/G$, for total galaxy mass M, mean star velocity v and gravitational constant G.

Within qBOUNCE, ultracold neutrons are sensitive to all forms of dark matter that alter gravity in the micrometer range (see end of section 1.2). Another class of particles that can be tested within qBOUNCE are particles, which exhibit a spin-mass coupling. This is one possible feature of an axion particle.

Axion

This hypothetical particle is of special interest because it can solve two problems at once: The strong CP-problem, and the origin of dark matter. Quantum chromodynamics is, as far as experiments suggest, CP (charge plus parity) conserving. As there is no theoretical reason for this in the Standard Model, Peccei and Quinn introduced a pseudoparticle — later named the axion — into the Lagrangian that is CP violating (**Peccei and Quinn** (1977)). The axion, however, turns out to be also a dark matter candidate.

There is a wide range of axion and axion-like particles proposed (see **Patrignani and Group** (2016), 686, for an overview of searches). A two-photon vertex exists, which is the basis of many axion searches. However, for the very light and electromagnetically neutral boson, there are two possibilities of coupling to fermions: the scalar vertex and the pseudoscalar vertex (**Moody and Wilczek** (1984)). In the neutron case, the axion would be responsible for the mediation of a CP-violating interaction between the spin of the neutron and a nucleon. For such an interaction between neutron and neutron mirror, limits on the existence of axions have been derived from previous qBOUNCE experiments (**Jenke et al.** (2014)). Other limits, for different couplings, come from astrophysical observations (e. g. **Raffelt** (2007)). In **Mantry et al.** (2014), mercury EDM measurements have been used to set bounds for axion and axion-like particles and were compared to other bounds.

2. Ultracold Neutrons

2.1. Properties of the Neutron

The same properties that kept the neutron from being discovered (**Chadwick** (1932b)), often make the neutron a very interesting and versatile measurement tool. The neutron itself can be used as an object in numerous research fields. Because of its electrical neutrality ($(-0.2 \pm 0.8) \times 10^{-21} e$, see **Patrignani and Group** (2016)), the neutron cannot directly ionise matter. Thus, for example absorption in an atomic nucleus is needed to produce ionising radiation or particles within a detector volume, for instance a bubble chamber or a ^{3}He counter tube. The neutron's electrical neutrality on the other hand allows neutrons to be used as a measurement tool in non-destructive imaging or material analysis techniques, penetrating matter without Coulomb repulsion and revealing information in optically or mechanically inaccessible domains.
Already in 1932 Chadwick estimated the mass of the neutron to be similar to the mass of the proton, based on kinematic considerations on elastic neutron scattering (**Chadwick** (1932a)). This ratio close to one between proton and neutron mass turns out to be advantageous for moderating neutrons via neutron-proton collisions. In addition, the mass of the neutron gives thermal neutrons (with velocities around $2200\,\mathrm{m/s}$) a de Broglie wavelength within the range of interatomic distances, well suited for solid state body examinations.
While being electromagnetically neutral, the neutron exhibits a magnetic moment. For a long time its nature was unclear (see for example **Breit and Rabi** (1934)) and the possibility that a magnetic moment indicates a composite structure of the neutron was only confirmed after the development of the quark model in the 1960s, trying to classify a zoo of hadronic particles that had meanwhile been discovered. Compared to atoms, the electromagnetic polarisability of neutrons is small and also due to its internal structure of two down and one up quark. The free neutron is unstable, decaying into a proton, an electron, and an electron antineutrino, with a mean lifetime of $880\,\mathrm{s}$. More on the characteristics of the neutron can be found in literature, for example in **Abele** (2008). Table 2.1 lists numerical values for the properties of most interest within this thesis.

The already mentioned electrical neutrality of the neutron is measured to a precision of 10^{-21} elementary charges, and the most precise direct measurement was performed in the 1980s (**Baumann et al.** (1988)). A finite but very small hypothetical electrical charge of the neutron could therefore raise questions about charge quantization. Different extensions of the Standard Model predict different outcomes of (neutron) charge measurements, be it charge quantization or also

Table 2.1.: Numerical values for selected properties of the neutron. The magnetic moment is expressed in units of nuclear magnetons, $\mu_{\mathrm{N}} = (e\hbar)/\left(2m_{\mathrm{p}}\right)$, and the electric charge in units of the elementary charge e. All values taken from **Patrignani and Group** (2016).

The Neutron	
Mass	$m_{\mathrm{n}} = (939.5654133 \pm 0.0000058)\ \mathrm{MeV/c^2}$
Spin	$s = 1/2$
Mean lifetime	$\tau_{\mathrm{n}} = (880.2 \pm 1.0)\ \mathrm{s}$
Magnetic moment	$\mu_{\mathrm{n}} = (-1.91304273 \pm 0.00000045)\,\mu_{\mathrm{N}}$
Electric polarisability	$\alpha_{\mathrm{n}} = (11.8 \pm 1.1) \times 10^{-4}\ \mathrm{fm^3}$
Magnetic polarisability	$\beta_{\mathrm{n}} = (3.7 \pm 1.2) \times 10^{-4}\ \mathrm{fm^3}$
Electric charge	$q_{\mathrm{n}} = (-0.2 \pm 0.8) \times 10^{-21}\ e$

a zero charge for the neutron, as predicted in Grand Unified Theories (**Abele** (2008)). Similarly, measurements of the electric dipole moment (EDM) of the neutron also aim at probing extension models of the Standard Model. Non-Standard Model contributions would add more CP (charge and parity) violating terms, which enlarges the expected value of the EDM. A non-zero neutron EDM would violate T (time reversal) as well as P symmetry, and if CPT symmetry is to be assumed, CP symmetry is also violated. Even though the first measurements were performed in 1950 (results published in **Smith et al.** (1957)), no non-zero value for the neutron EDM has been published until today. In the experiment of 1950 Ramsey's resonance method (the basis of the experiment of this thesis) was used and is still applied in many follow-up experiments. To explain for example the baryon-antibaryon asymmetry that is observed in the universe, a minimum neutron EDM was calculated to be around $10^{-28}\,e\,\mathrm{cm}$. While the current upper limit is $|d_n| < 3.0 \times 10^{-26}\,e\,\mathrm{cm}$ (**Pendlebury et al.** (2015)) and many constraints on baryogenesis and beyond Standard Model theories have already been set, future EDM experiments with increased sensitivities will be of much interest for particle physics and cosmology. Arguments in this paragraph taken from, and further information on the topic can be found in **Lamoreaux and Golub** (2009), **Dubbers and Schmidt** (2011) and **Abele** (2008).

2.2. Definition of Ultracold Neutrons

All experiments that deal with neutrons have to be located close to a neutron source due to the finite lifetime of the free neutron. Typically, high flux neutron sources are either nuclear fission reactors or spallation sources. The neutrons used within the experiments of qBOUNCE fall into the category of ultracold neutrons (UCNs). Due to the need of a high and continuous flux of UCNs, the experiment is taking place at the PF2, which is one of the UCN sources of the research reactor of the Institut Laue-Langevin in Grenoble, France (see section 2.3).

Table 2.2.: Real parts of Fermi pseudopotentials for selected elements. Scattering lengths taken from NIST Center for Neutron Research, and element data taken from the Wolfram Knowledgebase[2]. For positive Fermi potentials, the critical velocity v_c for total reflection under all angles of incidence is given. The critical velocity is calculated with the real part of the relation $m_n v_n^2 / 2 \cos^2 \theta_c = V_F$ (**Golub et al.** (1991)), with critical angle $\theta_c = 0$ and neutron mass m_n.

Element	Ti	V	Si	Al	Pb	Cu	C	Fe	^{65}Cu	Ni	Be	^{58}Ni
V_F [neV]	-51	-7	54	54	81	171	196	209	230	245	250	347
v_c [m/s]			3.2	3.2	3.9	5.7	6.1	6.3	6.6	6.8	6.9	8.2

Neutrons coming to experiments from a fission reactor will naturally have velocities distributed as a Maxwell-Boltzmann distribution (thermal spectrum), peaking at around 2200 m/s. Ultracold neutrons however, have velocities in the range of several meters per second. An appropriate definition for UCNs is via their capability of being totally reflected from surfaces at all angles of incidence (**Golub et al.** (1991)). This definition is dependent on the material the neutrons are reflecting on.

For every material a Fermi pseudopotential[1] can be calculated:

$$V = \frac{2\pi\hbar^2}{m} N a \, , \tag{2.1}$$

where m is the neutron mass, N is the number density in the material, and a is its coherent scattering length. As can be seen in table 2.2 where Fermi pseudopotentials for some materials are listed, the potential can also become negative when the coherent scattering length is negative. The scattering length is in general a complex quantity, where the real part contributes to the reflection, whereas the imaginary part determines the reflection loss, which shall not be covered here. For negative scattering lengths, the potential is attractive and neutrons will not be reflected. For a glancing angle smaller than the critical angle, the vertical component of the kinetic energy of neutrons can be smaller than the potential barrier of a material surface, given by the Fermi pseudopotential. This effect is used for example for manufacturing neutron beam guides, minimising losses when transferring neutrons from the reactor core to experiments. For UCNs (e. g. 5 m/s correspond to ≈ 130 neV), the condition for total reflection is, as stated above, fulfilled for all angles of incidence for certain materials (compare with table 2.2), opening new possibilities for neutron experiments.

---

[1]Or effective potential, named after Enrico Fermi who first had the idea that neutrons could be totally reflected (**Golub et al.** (1991)).

[2]https://www.nist.gov/ncnr/neutron-scattering-lengths-list and https://reference.wolfram.com/language/note/ElementDataSourceInformation.html.

Predicted by **Zel'dovich** (1959), first ultracold neutrons were extracted almost simultaneously by **Luschikov et al.** (1969) and **Steyerl** (1969).

Besides being able to store UCNs in bottles and determining the lifetime of the neutron (see **Wietfeldt and Greene** (2011) for an overview of neutron lifetime measurements), or using UCNs for neutron EDM measurements (see section 2.1), UCNs can be bound in the gravity potential of the Earth. The so-called ***Quantum Bouncer*** was proposed in **Langhoff** (1971) and **Gibbs** (1975) as an educational text book example for students. It describes a quantum particle or a point mass, falling due to gravity and bouncing off a flat surface. The concept was also applied to atoms (see for example **Wallis et al.** (1992)) and photons (**Della Valle et al.** (2009)). The first proposal to apply the Quantum Bouncer to ultracold neutrons was published in **Luschikov and Frank** (1978), already suggesting an experimental design to separate the first eigenstate of UCNs that are trapped in a gravity potential on a plane. Solving the Schrödinger equation for a neutron as a Quantum Bouncer in the gravity potential of the Earth $V(z) = mgz$, the eigenstates of the neutron are governed by the mathematical Airy function $\mathrm{Ai}(x)$. More on this system as well as a graphical representation follows in section 3.1.

2.3. Ultracold Neutron Source at the Institut Laue-Langevin

The Institut Laue-Langevin (ILL) is located in the French alps in the city of Grenoble. One of the world's most powerful research reactors (thermal power of 58.3 MW) is operating within this international research centre. In the 1980s, the instrument known today as **PF2** (**P**hysique **F**ondamentale **2**) originated with the installation of a new source for cold and ultracold neutrons (see **Steyerl et al.** (1986) and **Golub et al.** (1991), which were used for the following description). Figure 2.1 gives a schematic view of the components in use.

As pointed out in section 2.1, the similarity of the proton's and the neutron's mass is advantageous for moderating neutrons. Thermal neutrons are converted to ultracold neutrons primarily via two principles: thermalisation in the cold source with liquid deuterium, and Doppler shifting (through scattering) with a neutron turbine (**Steyerl** (1975)). After first being thermalised by surrounding D_2O, the neutrons coming from the reactor core eventually enter the cold source. There, further moderation of the neutrons occurs in liquid deuterium ($T \approx 25\,\mathrm{K}$). From the cold source, a curved nickel guide leads the neutrons to the neutron turbine. Half of the beam will then be guided to the very-cold neutron (VCN) beam port. Neutrons arriving at the turbine with $v \approx 50\,\mathrm{m\,s^{-1}}$ will be Doppler shifted by several reflections on the turning wheels of the turbine (peripheral velocity of $v = 25\,\mathrm{m\,s^{-1}}$) that are coated with nickel. Ultracold neutrons will then leave the turbine and are distributed to four beam ports where they may be used for experiments. A characteristic feature of the PF2 facility is that three of the
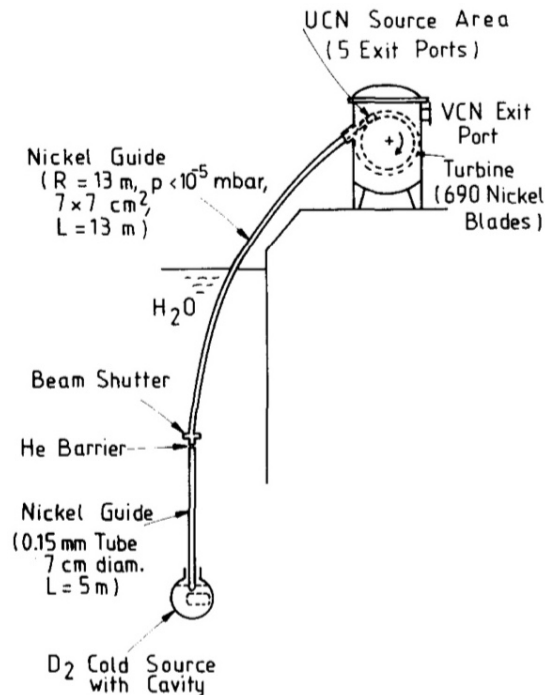
Figure 2.1.: PF2 instrument layout at the ILL. Image taken from **Steyerl et al.** (1986), 348, fig. 1.

four beamports are usually assigned to the UCN beam in cyclic order. Originally implemented for storage experiments (where UCNs are needed when a UCN bottle is filled but increase background when counting remaining neutrons in the bottle after a certain time), the neutrons are guided to each experimental place for around 200 s, before a switcher directs them to the next. For qBOUNCE, this measurement scheme allows for measuring the background rate in the detector repetitively during the complete measurement cycle.

The conversion of faster neutrons to ultracold neutrons close to the actual experiments is advantageous because faster neutrons undergo fewer reflections in the neutron guides, which leads to fewer losses. The bent neutron guide additionally separates very-cold neutrons from faster neutrons and gamma rays, and by extracting vertically from the cold source the neutrons lose kinetic energy gravitationally (1.7×10^{-6} eV for a rise of 17 m) while travelling upwards.

The vertical extraction from a cold source of UCNs and the use of a neutron turbine at the ILL as just described, is only one possibility of UCN production. Others are using for example phonon scattering in solid deuterium at pulsed reactors (**Kahlenberg et al.** (2017)) or spallation sources (**Lauss** (2014); **Ito et al.** (2018)), or superfluid helium at research reactors (**Leung et al.** (2016)) or spallation sources (**Ahmed et al.** (2018)). Other ultracold neutron sources are operating all around the world, and some are under construction. Several sources are compared in **Bison et al.** (2017). Due to the demand of the qBOUNCE

experiments for a steady high flux of UCNs, the PF2 is the source of choice up until today.

3. *q*Bounce and the Development of Gravity Resonance Spectroscopy

3.1. Neutrons in a Gravitational Field

In 2002, gravitationally bound states of ultracold neutrons were discovered (**Nesvizhevsky et al.** (2002) and see also **Nesvizhevsky et al.** (2003, 2005)). A quantum mechanical description of the experiment is given in **Westphal et al.** (2007).
Any particle that is put into a sufficiently deep and wide potential well will form quantum mechanical bound states. This fact alone is not surprising and visible in many systems, like electrons bound in an atom or nuclei being bound states of protons and neutrons. But a system that has its eigenstates defined by gravity is peculiar, because gravity is so weak compared to the other fundamental forces[1]. Due to the neutron's electric neutrality, a system like the Quantum Bouncer (compare section 2.2) can be prepared in a systematically clean way, so that the eigenstates of a neutron in the gravity potential of the Earth above a flat surface (a *neutron mirror*) can be measured.

Solving the problem of the Quantum Bouncer, the corresponding Schrödinger equation with the linearised gravity potential reads

$$\left(-\frac{\hbar^2}{2m} \frac{\mathrm{d}^2}{\mathrm{d}z^2} + mgz \right) \psi(z) = E\psi(z) \, , \tag{3.1}$$

with the conditions $\psi(z \leq 0) = \psi(z \to \infty) = 0$. Here, m is the neutron mass, g the gravitational acceleration, and E the energy of the wave function $\psi(z)$. Substituting $\tilde{z} = z/z_0$ with $z_0 = \left(\hbar^2/(2m^2 g) \right)^{1/3}$, and $\tilde{E} = E/E_0$ with $E_0 = mgz_0$, equation (3.1) becomes

$$-\frac{\mathrm{d}^2 \psi(\tilde{z})}{\mathrm{d}\tilde{z}^2} + (\tilde{z} - \tilde{E}) \, \psi(\tilde{z}) = 0 \, . \tag{3.2}$$

The quantities $z_0 = 5.9\,\mu\text{m}$ and $E_0 = 0.6\,\text{peV}$ define the characteristic length and energy scale of the system, respectively. Raising a neutron up by the length z_0 in

---

[1]The approximate strengths of the fundamental forces compared to gravity (set to 1) are: 10^{24} (weak), 10^{36} (electromagnetic), and 10^{38} (strong force).

the gravitational field of the Earth, corresponds to a gain in potential energy of E_0.

The differential equation equation (3.2) is special, in the sense that it can be solved by Airy functions Ai.[2] Therefore, the equation is sometimes referred to as *Airy differential equation*, and the function as *Airy rainbow function*[3]. Obeying the boundary conditions at $z = 0$, the wave functions read

$$\psi_n\left(\tilde{z}\right) = A_n \operatorname{Ai}\left(\tilde{z} - \tilde{E}\right), \tag{3.3}$$

where A_n are scaling constants. At $\tilde{z} = 0$, the wave functions have to vanish, which yields

$$\operatorname{Ai}(-\tilde{E}) = 0. \tag{3.4}$$

The outcome is therefore a quantisation of allowed energy levels of the system. They are defined by the zeros $\tilde{E}_n$ of the Airy functions.

A graphical representation of this system is shown in figure 3.1a. The first four eigenenergies are marked on the ordinate (neutron mirror), where the here arbitrarily scaled illustrations of the corresponding wave functions $\psi_n(\tilde{z})$ vanish. The abscissa shows the height above the mirror, and the potential V represents the potential term of equation (3.1). Figure 3.1b shows that the energy states of the neutron are shifted when the value of g changes. The experimental setup as well as the result from **Nesvizhevsky et al.** (2002) can be seen in figure 3.2. Neutrons enter the setup from the left, through a collimator that limits the horizontal velocity component. The UCNs then bounce along a neutron mirror, before being detected by an adjacent detector. Above the neutron mirror, an absorber scatters neutrons that interact with it out of the system. The height of the absorber above the neutron mirror was varied and the neutron flux through the system measured, leading to the measurement points shown in figure 3.2b. The classically expected curve (solid line) cannot describe the measurements properly. A quantum mechanical description for the neutron transmission rate confirms quantised states (figure 3.1).

The evidence of gravitationally bound ultracold neutrons was of course followed by other experiments. In general, a direct spatially resolving detection of the absolute value of square of the wave function of the neutrons is desirable. Furthermore, as the eigenenergies of the system are not equidistant, spectroscopic methods can be applied to measure the energy difference between the states. Two groups are engaged in experiments of these types. The Granit collaboration (see e. g. **Nesvizhevsky** (2012)) and the qBounce collaboration.

---

[2]In case of a second boundary condition, e. g. an absorber mirror on top, the solution is a linear combination of the functions Ai and Bi.

[3]The function was introduced in 1838 by Geroge Biddell Airy, describing the phenomena of caustics (e. g. rainbows) mathematically.

[4]All data plots and data analyses within this thesis have been generated/performed with Wolfram Mathematica 10 & 11, Student Edition. In parts, packages written by Hanno Filter, Jörg Herzinger, Tobias Jenke, and Martin Thalhammer have been used.
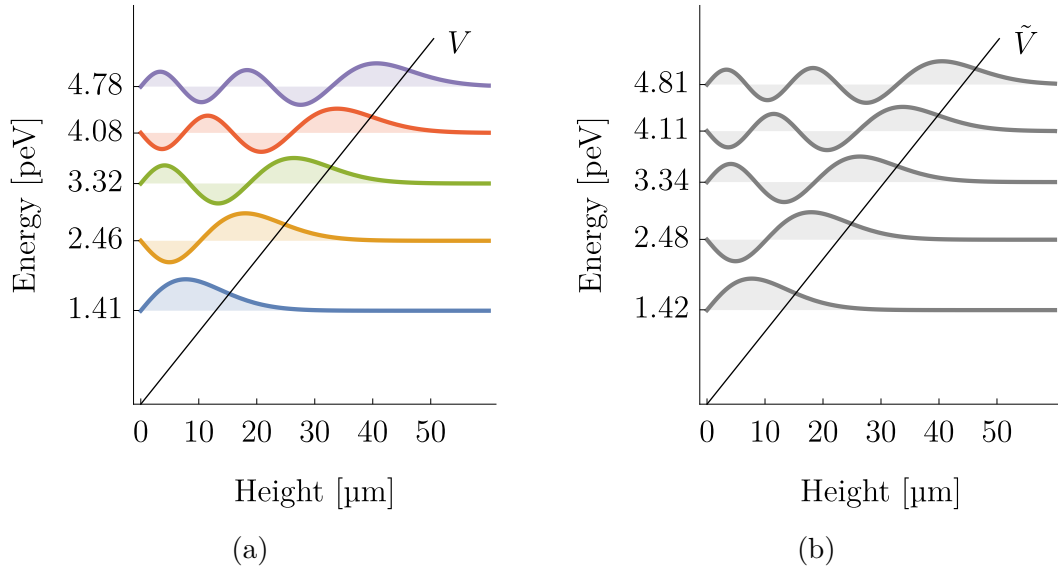
Figure 3.1.: (a) The first five eigenstates of a neutron gravitationally (potential V with $g = 9.805 \, \text{m/s}^2$) confined above a flat surface (y-axis) are displayed. (b) The energy states get shifted for a different potential $\tilde{V}$ with $g = 9.9 \, \text{m/s}^2$. Without constraints in positive height direction and without other forces present, the energy eigenstates are purely depending on the value of g and physical constants.[4]
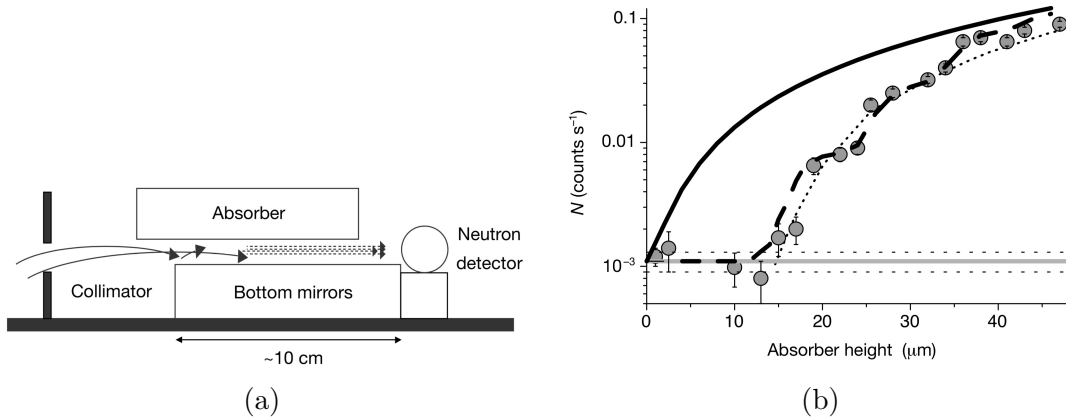

Figure 3.2.: Experimental setup (a) and part of the results (b) from **Nesvizhevsky et al.** (2002), 298, fig. 2 & 299, fig. 4. Varying the height of the absorber yields results predicted by quantum mechanics (dashed line) and does not fit to classical predictions (solid line).
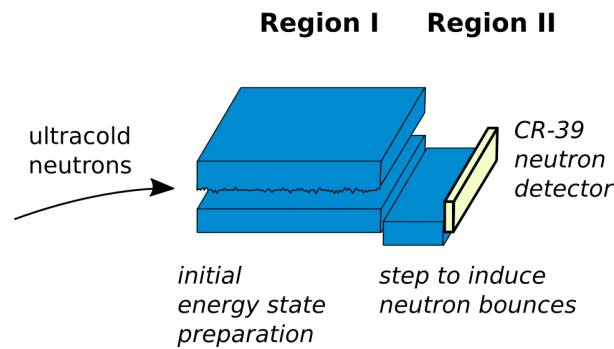
Region I   Region II

Figure 3.3.: Schematic view of the Quantum Bouncing Ball experiment. A neutron mirror-absorber system with a step in height down to a neutron mirror is followed by a spatial resolution neutron detector.

Section 3.2 briefly discusses the dynamics of a wave packet in a linear gravity potential, the so-called *Quantum Bouncing Ball.* In section 3.3, a short status quo as well as the main experiment of this thesis will be covered, both dealing with spectroscopic methods for UCNs in the gravity potential of the Earth — *Gravity Resonance Spectroscopy.*

3.2. The Quantum Bouncing Ball

The Quantum Bouncing Ball (QBB) experiment studies the dynamics of a wave packet — a neutron — in a linear gravity potential. Similar to the experiment in **Nesvizhevsky et al.** (2002), neutrons are prepared in an initial state (ground state) via a neutron mirror-absorber system, see figure 3.3. Afterwards, the prepared wave packet drops down a step of certain height, around 20–30 µm. The gain in kinetic energy leads to superposition of the initial state with higher states (compare figure 3.1). By using a detector with a spatial resolution, these quantum interferences can be visualised by measuring the absolute value of the square of the wave function after certain distances behind the step.

Measurements with a high level of statistical significance of such a quantum carpet succeeded in 2014 with the *q*BOUNCE experiment at the ILL (**Thalhammer** (2019)). Mirrors with different lengths were used in region II, after which detectors with a spatial resolution (boron coated CR-39) were placed.

3.3. Gravity Resonance Spectroscopy

Gravity Resonance Spectroscopy (GRS) (**Jenke et al.** (2011)) combines the powerful technique of spectroscopy with the unique system of gravitationally bound states of neutrons. While spectroscopic methods have been established for many years and are more important than ever (e. g. atomic clocks or Raman spectroscopy), they usually use electromagnetic radiation for achieving resonance

in the system of interest. A transition between two states is induced and their difference in energy measured.

Taking a setup described in section 3.1 and figure 3.1 of bound states of UCNs above a neutron mirror, spectroscopic methods can be applied, as the energy differences between any two states are unique. Transitions between two states can be induced by means of oscillatory magnetic field gradients (planned by the GRANIT collaboration), or via mechanical oscillations of the neutron mirror(s) in the interaction region(s) (*q*BOUNCE). For a Rabi-type spectrometer setup within *q*BOUNCE, measurements have been performed and will be summarised in the following section 3.3.1.

From a historical point of view, implementing a Rabi-type experiment will naturally be followed by a Ramsey-type setup, as the gain in sensitivity and versatility is usually worth a more complex experimental setup. Before Norman F. Ramsey invented his method of separated oscillating fields (**Ramsey** (1949)), his mentor and inventor of the molecular beam resonance method (**Rabi et al.** (1939)) in fact tried to keep Ramsey from staying in this very field of research. This was not until the beam resonance method was invented but according to Rabi, there was not much to be gained as the most interesting measurements (magnetic moments of proton and deuteron to $\approx 10\,\%$) have been done[5]. The field began to flourish after the first Rabi-type experiments delivered new and unexpected results (e. g. the discovery of the quadrupole moment of the deuteron) and only became even more essential with the development of Ramsey's method.

In the following, both methods will be described within the context of *q*BOUNCE.

3.3.1. Rabi-type Gravity Resonance Spectroscopy

A full Rabi-like setup consists of three regions — a preparation region, an interaction region, and an analyser region. Within *q*BOUNCE, a damped Rabi setup was realised in **Jenke** (2011) for the first time. All three regions were combined into one, which leads to an effective three-state system. Not only a proof of concept could be made (**Jenke et al.** (2011)), but also constraints on dark energy and dark matter models were set (**Jenke et al.** (2014), compare section 1.3).

In **Cronenberg** (2016), the first full three-part Rabi-like setup was realised within *q*BOUNCE. A schematic overview can be seen in figure 3.4. Ultracold neutrons enter the setup from the left. In the first region, the state preparation takes place. Just like in previous experiments mentioned, a mirror-absorber system scatters higher energy eigenstates out of the system. Ideally, only neutrons in their ground state arrive at region II, in which the neutron mirror (without a scatterer on top) oscillates mechanically. When hitting a resonance frequency, transitions from the

---

[5]Interview of Norman Ramsey by Katherine Sopka on 1976 November 23, Niels Bohr Library & Archives, American Institute of Physics, College Park, MD USA, `http://www.aip.org/history-programs/niels-bohr-library/oral-histories/32459`.
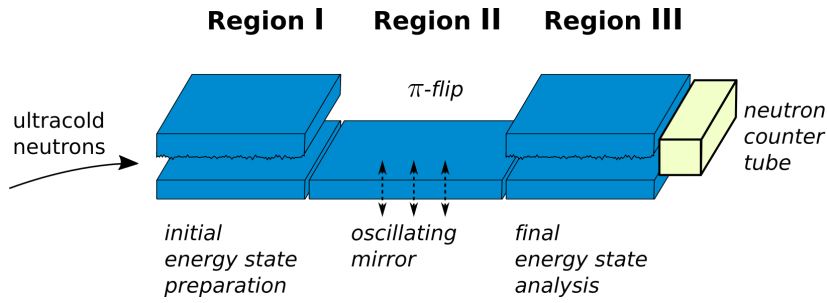
Figure 3.4.: Schematic view of a Rabi-type GRS experiment. In between two mirror-absorber systems to filter the ground state, an oscillating neutron mirror is placed to mechanically induce transitions between energy states of the neutrons. Count rates are measured with a counter tube.

first to a higher state can be driven. This is exactly the case when

$$\sigma_R \, \tilde{\tau} = \pi, \tag{3.5}$$

where σ_R is the Rabi-frequency that depends on the oscillation strength and the overlap integral between initial and final state (see chapter 4), and $\tilde{\tau}$ is the interaction time, the time the neutron spends in region II. Naturally, this is called a π-flip. Having a vector in a Bloch sphere for a two-state system in mind that is pointing to one of the poles, this corresponds to a transition of the vector to point to the other pole. Region III then again selects neutrons in the ground state and only those are detected in a neutron counter tube. The mathematical formulation of the problem can be found in many text books, in chapter 4, and can be looked-up in **Jenke** (2011) and **Cronenberg** (2016).

Besides setting constraints on a chameleon dark energy model or probing the weak equivalence principle (although for this more precise measurements by other experiments exist), the full three-part Rabi setup led to constraints for the hypothetical symmetron particle to be the origin of dark matter (**Cronenberg et al.** (2018)). The neutron mirror lengths of regions I, II, and III, were 150, 200, and 150 mm respectively.

The success of the implementations of Rabi's method within qBOUNCE is good motivation to take the next step in GRS to increase sensitivity: the implementation of Ramsey's method of spearated oscillating fields.

3.3.2. Ramsey-type Gravity Resonance Spectroscopy

Extending a Rabi-type setup to a Ramsey-type setup, the three main experimental regions will become five. This is due to the trick of Norman Ramsey who had the idea of splitting the interaction region into two parts, with a non-interaction region in between. This increases the precision of the experiment drastically and also enables numerous extensions of the system. In fact, the measurement principle of separated oscillating fields is nowadays used in atomic clocks and
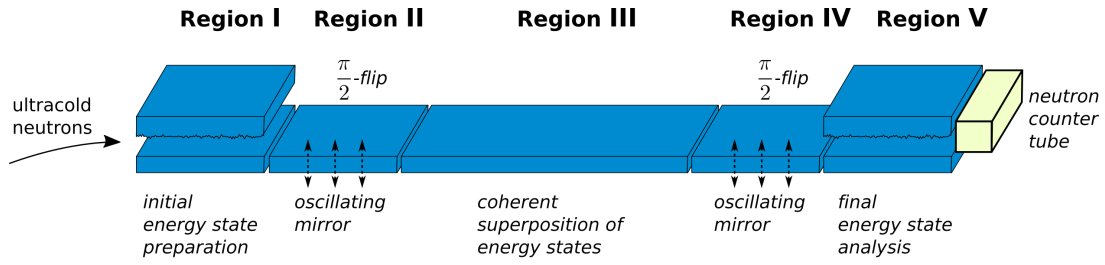
Figure 3.5.: Schematic view of a Ramsey-type GRS experiment. The interaction region between two neutron-absorber systems is split into two halves, with a region for free phase evolution of the coherent superposition of two energy states in between. Ground state neutrons are detected with a counter tube.

in the definition of the International System of Units (SI) of the second. One second is defined as 9 192 631 770 periods of the radiation corresponding to the transition between the two hyperfine levels of the ground state of the ^{133}Cs atom. Its special configuration with only one 6s electron (spin 1/2) and 54 electrons in xenon-configuration (total spin zero), make for a hyperfine splitting caused by the interaction of the electron spin with the nuclear spin (7/2). This is despite the fact that the electron moves around 55 000 times further away from the centre of the atom than the radius of the nucleus is. Using microwave radiation in a Ramsey-type setup, the electron spin can change from being anti-parallel to the nucleus (total spin 3) to parallel configuration (spin 4). This happens only at resonance, yielding the corresponding resonance frequency. As this process is very stable, it represents a good basis for the definition of the second.

A powerful tool like atomic clocks is not only used for the definition of the second. State of the art experiments use atoms to test gravity, search for dark matter, and dark energy (see e. g. **Burrage et al.** (2015); **Jaffe et al.** (2017); **Banahene-Sabulsky** (2018)). However, the application of Ramsey's method stretches even further, with neutron electric dipole measurements, ion mass measurements, the closely related spin-echo technique, or nuclear magnetic resonance (NMR) experiments.

For a Ramsey setup within qBounce, as has been proposed in **Abele et al.** (2010), a schematic overview can be seen in figure 3.5. Again, UCNs enter from the left. Region I is the same preparation region as before, the rough upper mirror scatters higher states out of the system. Ideally, only neutrons in the ground state, the initial state $|i\rangle$, enter the first interaction region II, where a mechanically oscillating mirror applies a $\frac{\pi}{2}$-flip. This leads to a coherent superposition of the initial state and the desired final state at the end of region II: $1/\sqrt{2}\left(|i\rangle + |f\rangle\right)$. Analogous to equation (3.5), the condition for this reads

$$\sigma_R \tau = \frac{\pi}{2}\,, \tag{3.6}$$

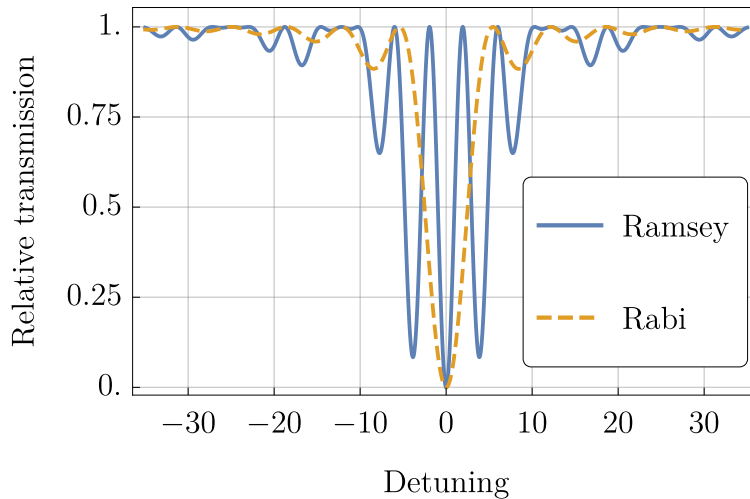3. qBounce and the Development of Gravity Resonance   Spectroscopy

Figure 3.6.: Typical Ramsey and Rabi fringes for a qBounce experiment. The detuning is with respect to the resonance frequency for the given transition. The total length of the oscillating regions for both experiments are the same, but for the Ramsey-setup an additional middle region of the same length is inserted.

where τ is the flight time through one perturbation region. On the Bloch sphere, this corresponds to a transition from a vector pointing to a pole, to a vector pointing to the equator. It is important to keep in mind that this transition is induced purely mechanically, which is an absolute novelty for a Ramsey-type setup.

The free precession of the phase of the superposition can evolve in region III. The longer the flight time T through region III is, the higher the energy resolution of the setup will be. Tiny deviations from the resonant frequency in region II will lead to the Bloch vector not pointing to the equator, and therefore ultimately lead to increasing phase differences, as the vector rotates around the vertical axis. The dependence of the energy resolution on T will be shown in more detail in the theoretical description in chapter 4.

Region IV is identical to region II and oscillates in phase, and in the case of perfect resonance this second $\frac{\pi}{2}$-flip will complete the transition of the neutron to the final state $|f\rangle$, the opposite pole of $|i\rangle$ on the Bloch sphere. If, however, the oscillations of region II and IV are off resonance, $\omega_r - \omega \neq 0$, the transition probability will decrease. As region V is identical to region I and only lets neutrons in state $|i\rangle$ pass, the count rate will be zero for a perfect transition and at most when no transition takes place.

A typical measurement pattern for such a Ramsey-type experiment in comparison with a Rabi-setup is shown in figure 3.6. While the total length of the interaction regions for both setups is the same, an additional region of free propagation of the coherent superposition of initial and final state is inserted in between the interaction regions of the Ramsey-setup. Its length is chosen to

be $L = Tv_n = 2\tau v_n$ for this graph, with the vertical velocity component of the neutrons v_n. For $L \to 0$, the Ramsey curve will become the Rabi curve.

While the full width at half maximum (FWHM) is significantly smaller for the Ramsey curve in this figure (which is desirable as steeper slopes increase the precision), this is only the case when the total length of the setup increases. For identical setup lengths, the FWHM are similar. Still, a major advantage of the Ramsey method is that by inserting a non-oscillating (and therefore technically more easy to handle) region, the sensitivity is increased.

Even with similar setup lengths, however, the Ramsey method is superior to the Rabi method. As can be seen in figure 3.6, the Ramsey curve has more prominent side maxima, which increase the precision with which a theory function can be fitted to measurement data. These side maxima are not achievable with a Rabi setup.

The lengths of the neutron mirrors of the first realisation of Ramsey-type GRS presented here, are 150, 152, 340, 152, and 152 mm, for regions I to V, adding up to 946 mm in total.

Part II

Gravity Resonance Spectroscopy: Theoretical Considerations

4. Ramsey's Method of Separated Oscillating Fields

In the following section of this thesis theoretical concepts of a Ramsey-type experiment within qBOUNCE will be treated. The first section will introduce the Ramsey method. This done by starting with a single oscillating mirror, which is the Rabi method. The result will be generalised and Ramsey's method will be applied.

The subsequent sections will then focus on the qualitative behaviour of such a system within qBOUNCE, experimental parameters for the first realisation will be introduced, and possible measurement methods discussed. In the last section, Monte Carlo simulations for the purely classical analogue are compared to the quantum mechanical predictions.

4.1. Rabi's Method

This section presents Rabi's method for solving the problem of a neutron in a gravitational field above an oscillating mirror. It will be shown to be the basis for arriving at Ramsey's formula for separated oscillating fields, or, in this case, mirrors.

The **unperturbed solution** of neutrons in a gravitational field above a flat surface is just the solution of the Quantum Bouncer (section 3.1). The Schrödinger equation is one-dimensional, as the solutions in the plane of the surface are separable and given by plane waves:

$$\hat{H}_0 \tilde{\psi}^{(0)}\left(\tilde{z}, \tilde{t}\right) = i\hbar \frac{\partial}{\partial \tilde{t}} \, \tilde{\psi}^{(0)}\left(\tilde{z}, \tilde{t}\right) \ , \tag{4.1}$$

with

$$\hat{H}_0 = \left(-\frac{\hbar^2}{2m} \frac{\partial^2}{\partial \tilde{z}^2} + mg\tilde{z} \right) \ . \tag{4.2}$$

Here, symbols marked by a tilde indicate the frame of reference to be the inertial frame and quantities with superscript *(0)* refer to the unperturbed system. When introducing a **perturbation** (in this case an oscillating boundary condition, that is, an oscillating neutron mirror), another term is added to the left-hand side of equation (4.1) and the corresponding Schrödinger equation reads

$$\left[\hat{H}_0 + \hat{W}\left(\tilde{z}, \tilde{t}\right) \right] \tilde{\psi}\left(\tilde{z}, \tilde{t}\right) = i\hbar \frac{\partial}{\partial \tilde{t}} \, \tilde{\psi}\left(\tilde{z}, \tilde{t}\right) \ , \tag{4.3}$$

4. Ramsey's Method of Separated Oscillating Fields

with

$$\hat{W}\left(\tilde{z}, \tilde{t}\right) = V \, \Theta\left(-\tilde{z} + a \sin \omega t\right) \ . \tag{4.4}$$

The Fermi pseudopotential V of the neutron mirror represents the boundary condition via the Heaviside function Θ, where the oscillation of the mirror with amplitude a and angular frequency ω is taken into account with the sine term. Solving equation (4.3) will give a description of how the wave function of a neutron is influenced by the oscillation of the mirror and corresponds to the **solution of a Rabi-like system**, in which a perturbation is switched on once, for a finite time. For a Ramsey-like setup, where the perturbation acts two (or multiple) times with sections of free evolution of the neutron in between, the outcome will be an intermediate result.

The solution follows **Landau and Lifshitz** (1981) and **Pitschmann** (2018). To get rid of the time dependency of Θ, a transformation to the non-inertial frame via

$$\begin{aligned} t &= \tilde{t} \\ z &= \tilde{z} - a \sin \omega \tilde{t} \ , \end{aligned} \tag{4.5}$$

and $\tilde{\psi}\left(\tilde{z}, \tilde{t}\right) = \psi\left(z, t\right)$ is useful and yields[1]

$$\begin{aligned} \frac{\partial}{\partial \tilde{z}} &= \frac{\partial}{\partial z} \\ \frac{\partial}{\partial \tilde{t}} &= -a\omega \cos \omega t \frac{\partial}{\partial z} + \frac{\partial}{\partial t} \ . \end{aligned} \tag{4.6}$$

With this, equation (4.3) becomes

$$\left[\hat{H}_0 + \hat{V}\left(z, t\right)\right] \psi\left(z, t\right) = i\hbar \frac{\partial}{\partial t} \, \psi\left(z, t\right) \tag{4.7}$$

$$\left(-\frac{\hbar^2}{2m} \frac{\partial^2}{\partial z^2} + mgz + mga \sin \omega t + \hbar a\omega \cos \omega t \frac{\partial}{\partial z}\right) \psi\left(z, t\right) = i\hbar \frac{\partial}{\partial t} \, \psi\left(z, t\right) \ , \tag{4.8}$$

with

$$\hat{V} = mga \sin \omega t + \hbar a\omega \cos \omega t \frac{\partial}{\partial z} \ . \tag{4.9}$$

A solution can be found in the form of

$$\psi\left(z, t\right) = \sum_k a_k(t)\psi_k^{(0)}(z, t) \ , \tag{4.10}$$

where the $\psi_k^{(0)}(z, t)$ are the (time dependent) wave functions of the unperturbed system (corresponding to $\hat{H}_0$, see equation (4.1)) and the time dependent a_k are

---

[1]Through $\frac{\partial}{\partial x^i} = \frac{\partial y^j}{\partial x^i} \frac{\partial}{\partial y^j}$, for two sets of variables x^i and y^j.

expansion coefficients.

Equation (4.7) then becomes

$$i\hbar \sum_k \frac{\mathrm{d}}{\mathrm{d}t}\psi_k^{(0)}(z,t)\,a_k = \sum_k a_k \hat{V}\psi_k^{(0)}(z,t) \ . \tag{4.11}$$

Multiplying from the left with $\psi_m^{(0)*}(z,t)$ and integrating yields

$$i\hbar \frac{\mathrm{d}a_m}{\mathrm{d}t} = \sum_k V_{mk}(t)a_k \ , \tag{4.12}$$

due to orthogonality of the unperturbed wave functions. The matrix elements of the perturbation V_{mk} for a transition between states m and k arise with $\omega_{mk} = (E_m^{(0)} - E_k^{(0)})/\hbar$:

$$
\begin{aligned}
V_{mk}(t) &= \int \psi_m^{(0)*}(z,t)\,\hat{V}\,\psi_k^{(0)}(z,t)\,\mathrm{d}z \\
&= \int \psi_m^{(0)*}(z)\,\hat{V}\,\psi_k^{(0)}(z)\,e^{i\omega_{mk}t}\,\mathrm{d}z \\
&= V_{mk}\,e^{i\omega_{mk}t} \ .
\end{aligned}
\tag{4.13}
$$

Equation (4.12) represents the Schrödinger equation with the ansatz from equation (4.10), hence describes the evolution of a certain quantum state in the perturbed system of a neutron above an oscillating mirror.

The operator $\hat{V}$ of the perturbation is periodic with respect to time and is (using Euler's formula and equation (4.9)) of the form

$$
\begin{aligned}
\hat{V} &\equiv \hat{F}e^{-i\omega t} + \hat{F}^\dagger e^{i\omega t} \\
&= mga\frac{e^{i\omega t} - e^{-i\omega t}}{2i} + i\hbar a\omega \frac{e^{i\omega t} + e^{-i\omega t}}{2}\frac{\partial}{\partial z} \ .
\end{aligned}
\tag{4.14}
$$

The time independent part can be separated:

$$\hat{F} = i\frac{mga}{2} + i\hbar\frac{a\omega}{2}\frac{\partial}{\partial z} \ , \tag{4.15}$$

and with equation (4.13) the matrix elements of the perturbation become

$$V_{kn}(t) = F_{kn}e^{i(\omega_{kn}-\omega)t} + F_{nk}^* e^{i(\omega_{kn}+\omega)t} \ . \tag{4.16}$$

Together with equation (4.16), equation (4.12) can be used to describe this system with

$$
\begin{aligned}
i\hbar\frac{\mathrm{d}a_m}{\mathrm{d}t} &= \sum_k a_k \left(F_{mk}e^{i(\omega_{mk}-\omega)t} + F_{km}^* e^{i(\omega_{mk}+\omega)t} \right) \ , \\
i\hbar\frac{\mathrm{d}a_n}{\mathrm{d}t} &= \sum_k a_k \left(F_{nk}e^{i(\omega_{nk}-\omega)t} + F_{kn}^* e^{i(\omega_{nk}+\omega)t} \right) \ .
\end{aligned}
\tag{4.17}
$$

4. Ramsey's Method of Separated Oscillating Fields

Equation (4.17) seems rather difficult to solve analytically without loss of generality. Therefore, from here on, only a **transition between two states** m and n is considered. Near a resonance,

$$E_m^{(0)} - E_n^{(0)} = \hbar(\omega + \varepsilon) , \tag{4.18}$$

and $\varepsilon \ll \omega$.[2] With this, the sum in equation (4.17) has only two terms. In addition, the second terms in the brackets on the right-hand side in equation (4.17) oscillate rapidly in comparison to the first terms for sufficiently large observations periods, (which is usually the case), average out and can therefore be neglected. Only one term of the sum remains:

$$
\begin{aligned}
i\hbar\frac{\mathrm{d}a_m}{\mathrm{d}t} &= a_n F_{mn} e^{i\varepsilon t} , \\
i\hbar\frac{\mathrm{d}a_n}{\mathrm{d}t} &= a_m F_{mn}^* e^{-i\varepsilon t} .
\end{aligned}
\tag{4.19}
$$

This system of equations can be solved by substituting $a_n e^{i\varepsilon t} = b_n$, which leads to

$$
\begin{aligned}
i\hbar\dot{a}_m &= F_{mn} b_n , \\
i\hbar(\dot{b}_n - i\varepsilon b_n) &= F_{mn}^* a_m .
\end{aligned}
\tag{4.20}
$$

Eliminating a_m gives

$$\ddot{b}_n - i\varepsilon\dot{b}_n + \frac{|F_{mn}|^2 b_n}{\hbar^2} = 0 . \tag{4.21}$$

A solution can be found through the ansatz $b_n(t) = e^{i\lambda t}$:

$$\lambda^2 + \varepsilon\lambda - \frac{|F_{mn}|^2}{\hbar^2} = 0 , \tag{4.22}$$

where

$$\lambda = -\frac{\varepsilon}{2} \pm \Omega , \tag{4.23}$$

and

$$\Omega = \sqrt{\frac{|F_{mn}|^2}{\hbar^2} + \frac{\varepsilon^2}{4}} . \tag{4.24}$$

Here, $\Omega = (\Omega_R + \Delta\omega^2)^{1/2}$ can be identified with the generalised Rabi frequency, depending on the Rabi frequency Ω_R at resonance, and the detuning $\Delta\omega^2$.

This gives a solution for a_n and through equation (4.19) also for a_m:

$$
\begin{aligned}
a_n(t) &= A e^{-i(\frac{\varepsilon}{2}-\Omega)t} + B e^{-i(\frac{\varepsilon}{2}+\Omega)t} , \\
a_m(t) &= \frac{A\hbar}{F_{mn}^*}\left(\frac{\varepsilon}{2}-\Omega\right) e^{i(\frac{\varepsilon}{2}+\Omega)t} + \frac{B\hbar}{F_{mn}^*}\left(\frac{\varepsilon}{2}+\Omega\right) e^{i(\frac{\varepsilon}{2}-\Omega)t} ,
\end{aligned}
\tag{4.25}
$$

---

[2]N.B.: For positive ω, $E_m^{(0)} > E_n^{(0)}$.

where A and B are constants, which have to be determined by initial conditions. Remembering equation (4.10) gives

$$\psi(z,t) = \left(-\frac{\hbar A}{F^*_{mn}} \left(\frac{\varepsilon}{2} - \Omega \right) e^{i\Omega t} + \frac{\hbar B}{F^*_{mn}} \left(\frac{\varepsilon}{2} + \Omega \right) e^{-i\Omega t} \right) e^{i\frac{\varepsilon}{2}t} \psi_m^{(0)}(z,t)$$
$$+ \left(A e^{i\Omega t} + B e^{-i\Omega t} \right) e^{-i\frac{\varepsilon}{2}t} \psi_n^{(0)}(z,t) . \quad (4.26)$$

To obtain a final result, for $t = 0$ let only the state m to be occupied: $\psi(z,0) = \psi_m^{(0)}(z,0)$. This then yields

$$A = -\frac{F^*_{mn}}{2\hbar\Omega} , \qquad \text{and} \qquad B = \frac{F^*_{mn}}{2\hbar\Omega} . \quad (4.27)$$

Finally, inserting yields the **wave function $\psi(z,t)$ for a Rabi-like perturbation of an initially populated m-state**:

$$\psi(z,t) = \left(-\frac{1}{2\Omega} \left(\frac{\varepsilon}{2} - \Omega \right) e^{i\Omega t} + \frac{1}{2\Omega} \left(\frac{\varepsilon}{2} + \Omega \right) e^{-i\Omega t} \right) e^{i\frac{\varepsilon}{2}t} \psi_m^{(0)}(z,t)$$
$$+ \left(-\frac{F^*_{mn}}{2\hbar\Omega} e^{i\Omega t} + \frac{F^*_{mn}}{2\hbar\Omega} e^{-i\Omega t} \right) e^{-i\frac{\varepsilon}{2}t} \psi_n^{(0)}(z,t) . \quad (4.28)$$

Rewriting in terms of sine and cosine functions, the result takes on a more compact form:

$$\psi(z,t) = \left(\cos\Omega t - \frac{i\varepsilon}{2\Omega} \sin\Omega t \right) e^{i\frac{\varepsilon}{2}t} \psi_m^{(0)}(z,t) - \frac{iF^*_{mn}}{\hbar\Omega} \sin\Omega t \, e^{-i\frac{\varepsilon}{2}t} \psi_n^{(0)}(z,t) . \quad (4.29)$$

The corresponding probabilities of finding the neutron in state m or n can readily be obtained via $|a_m(t)|^2$ and $|a_n(t)|^2$, which for the state n yields

$$|a_n(t)|^2 = \frac{|F_{mn}|^2}{\hbar^2 \Omega^2} \sin^2 \Omega t , \quad (4.30)$$

and $\left(|a_m(t)|^2 = 1 - |a_n(t)|^2 \right)$. For a Rabi-like setup, it is therefore desirable to have $\Omega t = \pi$ for a full transition to the state n, whereas for a Ramsey-like setup an equal superposition of m and n states demands for $\Omega t = \frac{\pi}{2}$. Experimentally, the probability for a specific transition at angular frequency ω can be tuned via the duration of the perturbation t and the amplitude of the oscillating mirror a, which occur in Ω (equation (4.24)) because

$$|F_{mn}|^2 = \frac{(\hbar a\omega)^2}{4} \left(\int \psi_m^{(0)*} \frac{\partial}{\partial z} \psi_n^{(0)} \mathrm{d}z \right) = \frac{(\hbar a\omega)^2}{4} Q_{mn}^2 . \quad (4.31)$$

For a so-called $\frac{\pi}{2}$-flip it follows that at resonance the optimal oscillation amplitude arises through

$$\Omega t \stackrel{!}{=} \frac{\pi}{2} = t \frac{|F_{mn}|}{\hbar}$$
$$\frac{\pi}{2} = t \frac{a\omega}{2} Q_{nm} , \quad (4.32)$$

which yields with $t = l/v$ (length l of the neutron mirror and velocity v of the neutron):

$$a_x = \frac{v\pi}{l\omega Q_{nm}} \quad \text{and} \quad a_v = \frac{v\pi}{lQ_{nm}} \ . \tag{4.33}$$

Here, a_x denotes the spatial amplitude of the oscillation and a_v the corresponding velocity. Tables for the transition frequencies between two states, as well as the overlap integrals $\int \psi_m^{(0)*} \frac{\partial}{\partial z} \psi_n^{(0)} \mathrm{d}z = Q_{mn}$, can be found in tables A.1 and A.2, respectively.

4.2. Ramsey's Method

The result just obtained corresponds to the wave function after the first perturbation region II in a Ramsey-like setup. To proceed with a Ramsey-like setup, equation (4.29) is nevertheless impractical, as repeated application for more than one oscillating region presumes full population of only the initial state m, at the beginning of all oscillating regions. Therefore, the constants A and B have to be kept general, before the results may be applied to a Ramsey-setup within qBOUNCE.

Generalisation

The perturbation is supposed to start at an arbitrary time $t = t_1$. To generalise A and B in equation (4.26), the coefficients of the wave functions are set to time-depending values $C_m(t_1)$ and $C_n(t_1)$, respectively. Taking the time evolution out of the wave functions (i. e. $\psi_i^{(0)}(z,t) = \mathrm{e}^{-i\frac{E_i}{\hbar}t}\psi_i^{(0)}(z, t = 0) = \mathrm{e}^{-i\omega_i t}\psi_i^{(0)}(z)$), and using equation (4.18), equation (4.26) yields

$$\left(\frac{\hbar A}{F_{mn}^*} \left(\frac{\varepsilon}{2} - \Omega \right) e^{i\Omega t_1} + \frac{\hbar B}{F_{mn}^*} \left(\frac{\varepsilon}{2} + \Omega \right) e^{-i\Omega t_1} \right) e^{-i(\omega_m + \omega_n + \omega)\frac{t_1}{2}} = C_m(t_1) \ , \tag{4.34a}$$

$$\left(A e^{i\Omega t_1} + B e^{-i\Omega t_1} \right) e^{-i(\omega_m + \omega_n - \omega)\frac{t_1}{2}} = C_n(t_1) \ . \tag{4.34b}$$

Taking

$$B e^{-i\Omega t_1} = C_n(t_1) e^{i(\omega_m + \omega_n - \omega)\frac{t_1}{2}} - A e^{i\Omega t_1} \tag{4.35}$$

from equation (4.34b) and inserting into equation (4.34a), yields the constant A and therefore also B:

$$
A = \frac{e^{-\frac{1}{2}it_1(-w_m - w_n + \omega + 2\Omega)} \left(\frac{\hbar}{F_{mn}^*} C_n(t_1)(\varepsilon + 2\Omega) - 2C_m(t_1)e^{it_1\omega} \right)}{4\frac{\hbar}{F_{mn}^*}\Omega} \ ,
$$

$$
B = \frac{e^{\frac{1}{2}it_1(w_m + w_n - \omega + 2\Omega)} \left(-\frac{\hbar}{F_{mn}^*} C_n(t_1)(\varepsilon - 2\Omega) + 2C_m(t_1)e^{it_1\omega} \right)}{4\frac{\hbar}{F_{mn}^*}\Omega} \ .
\tag{4.36}
$$

For a duration τ of a perturbation that starts at $t = t_1$, equation (4.26) becomes

$$
\begin{aligned}
\psi(z, t_1 + \tau) = {}& \left(-\frac{\hbar A}{F_{mn}^*} \left(\frac{\varepsilon}{2} - \Omega \right) e^{i\Omega(t_1+\tau)} + \frac{\hbar B}{F_{mn}^*} \left(\frac{\varepsilon}{2} + \Omega \right) e^{-i\Omega(t_1+\tau)} \right) \\
& \times e^{-i(\omega_m+\omega_n+\omega)\frac{t_1+\tau}{2}} \psi_m^{(0)}(z) + \left(A e^{i\Omega(t_1+\tau)} + B e^{-i\Omega(t_1+\tau)} \right) \\
& \times e^{-i(\omega_m+\omega_n-\omega)\frac{t_1+\tau}{2}} \psi_n^{(0)}(z) \,.
\end{aligned}
\tag{4.37}
$$

This can be read as

$$
\psi(z, t_1 + \tau) = C_m(t_1 + \tau)\psi_m^{(0)}(z) + C_n(t_1 + \tau)\psi_n^{(0)}(z) \,.
\tag{4.38}
$$

Often, only the coefficients $C(t)$ are of interest, as the probability of finding the neutron in state m at time t is given by $|C_m(t)|^2$. Inserting A and B from equation (4.36) into equation (4.37) results in

$$
\begin{aligned}
C_m(t_1 + \tau) = {}& \frac{1}{8\Omega} e^{-\frac{i}{2}(\omega+\omega_m+\omega_n)\tau} e^{-i\omega t_1} e^{-i\Omega\tau} \left[\frac{\hbar}{F_{mn}^*} C_n(t1) \left(-1 + e^{2i\Omega\tau} \right) \right. \\
& \left. \times \left(\varepsilon^2 - 4\Omega^2 \right) + 2C_m(t_1)e^{i\omega t_1} \left(\varepsilon + 2\Omega + e^{2i\Omega\tau}(-\varepsilon + 2\Omega) \right) \right] \,,
\end{aligned}
\tag{4.39a}
$$

$$
\begin{aligned}
C_n(t_1 + \tau) = {}& \frac{F_{mn}^*}{4\Omega\hbar} e^{\frac{i}{2}\tau(\omega-\omega_m-\omega_n)} e^{-i\Omega\tau} \left[-2C_m(t_1)e^{i\omega t_1} \left(-1 + e^{2i\Omega\tau} \right) \right. \\
& \left. + \frac{\hbar}{F_{mn}^*} C_n(t_1) \left(-\varepsilon + 2\Omega + e^{2i\Omega\tau}(\varepsilon + 2\Omega) \right) \right] \,.
\end{aligned}
\tag{4.39b}
$$

Expanding, using $\varepsilon^2 - 4\Omega^2 = -4F_{mn}^*/\hbar$, and rewriting in terms of sine and cosine functions finally yields

$$
\begin{aligned}
C_m(t_1 + \tau) = {}& \left[-\frac{iF_{mn}^*}{\hbar\Omega} e^{-i\omega t_1} \sin\Omega\tau \, C_n(t_1) \right. \\
& \left. + \left(-\frac{i\varepsilon}{2\Omega} \sin\Omega\tau + \cos\Omega\tau \right) C_m(t_1) \right] e^{-i(\omega_m+\omega_n+\omega)\frac{\tau}{2}} \,,
\end{aligned}
\tag{4.40a}
$$

$$
\begin{aligned}
C_n(t_1 + \tau) = {}& \left[-\frac{iF_{mn}^*}{\hbar\Omega} e^{i\omega t_1} \sin\Omega\tau \, C_m(t_1) \right. \\
& \left. + \left(\frac{i\varepsilon}{2\Omega} \sin\Omega\tau + \cos\Omega\tau \right) C_n(t_1) \right] e^{i(+\omega-\omega_m-\omega_n)\frac{\tau}{2}} \,.
\end{aligned}
\tag{4.40b}
$$

This corresponds to equation (4) in **Ramsey** (1950), with which the following identifications can be made to compare the results:

$$m \triangleq q \, , \qquad\qquad \frac{F_{mn}}{\hbar} = \frac{F_{nm}^*}{\hbar} \triangleq b \, ,$$

$$n \triangleq p \, , \qquad\qquad \frac{F_{mn}}{\hbar\Omega} \triangleq \sin\theta \, , \qquad\qquad (4.41)$$

$$2\Omega \triangleq a \, , \qquad\qquad \frac{\varepsilon}{2\Omega} \triangleq \cos\theta \, .$$

Equations (4.40a) and (4.40b) are **the weights of the corresponding wave functions after the first perturbation region**, with arbitrary initial weights $C_m(t_1)$ and $C_n(t_1)$.

Region III, a **section of free evolution** of the neutron follows, for which the oscillation amplitude $a = 0$, and therefore also $F_{mn}^*/\hbar = 0$. With this, equations (4.40a) and (4.40b) become[3]

$$C_m(t_1 + \tau) = C_m(t_1)\, e^{-i\omega_m \tau} \, , \qquad\qquad (4.42a)$$

$$C_n(t_1 + \tau) = C_n(t_1)\, e^{-i\omega_n \tau} \, , \qquad\qquad (4.42b)$$

which are merely the time evolutions of the wave functions. This is an important cross-check.

With the same approach as in **Ramsey** (1950), subsequent applications of equation (4.40) and equation (4.42) for the interaction regions II and IV and the non-interaction region III, respectively, yield the corresponding weights for the wave functions (and hence also the states' occupation probabilities) for arbitrary times $t > t_1$.

Application of Results

Starting with a neutron prepared in state n at the beginning of region II in a five mirror setup at time $t = 0$, the wave function of the neutron leaving the perturbation region at time τ reads[4]

$$\psi_{II}(z, \tau) = -\frac{iF_{mn}^*}{\hbar\Omega} \sin\Omega\tau \; e^{-i(\omega_m + \omega_n + \omega)\frac{\tau}{2}} \; \psi_m^{(0)}(z)$$

$$+ \left(\frac{i\varepsilon}{2\Omega} \sin\Omega\tau + \cos\Omega\tau \right) e^{i(+\omega - \omega_m - \omega_n)\frac{\tau}{2}} \; \psi_n^{(0)}(z) \, . \quad (4.43)$$

Region III is a free evolution of $\psi_{II}(z, \tau)$ of duration T. As qBounce is driving transitions by mechanical means, it is legitimate to assume the value of the energy

---

[3]Using $\cos\frac{\varepsilon}{2}\tau \pm i\sin\frac{\varepsilon}{2}\tau = e^{\pm i(\omega_m - \omega_n - \omega)\frac{\tau}{2}}$.

[4]The derivation allows for any initial occupations, this one is chosen for comparison to the results in the literature and for keeping equations shorter.

states n and m to be and stay unchanged from their initial values[5]. Thus, there is no necessity of introducing a space mean value of ω_n and ω_m as is described in **Ramsey** (1950). Using equation (4.42), the neutron wave function after region III becomes

$$
\begin{aligned}
\psi_{III}(z, \tau + T) = & -\frac{iF_{mn}^*}{\hbar\Omega}\sin\Omega\tau\; e^{-i(\omega_m+\omega_n+\omega)\frac{\tau}{2}}\; e^{-i\omega_m T}\; \psi_m^{(0)}(z) \\
& + \left(\frac{i\varepsilon}{2\Omega}\sin\Omega\tau + \cos\Omega\tau\right) e^{i(+\omega-\omega_m-\omega_n)\frac{\tau}{2}}\; e^{-i\omega_n T}\; \psi_n^{(0)}(z)\;.
\end{aligned}
$$
(4.44)

Finally, another perturbation acts on the neutron, which is represented by $\psi_{III}(z, \tau + T)$ upon entering the the second perturbation region IV. After this region, the wave function is described by

$$
\begin{aligned}
\psi_{IV}(z, 2\tau + T) = & \left[-\frac{iF_{mn}^*}{\hbar\Omega}e^{-i\omega(\tau+T)}\sin\Omega\tau\; C_{n,III}(\tau+T) \right. \\
& \left. + \left(-\frac{i\varepsilon}{2\Omega}\sin\Omega\tau + \cos\Omega\tau\right)C_{m,III}(\tau+T)\right] e^{-i(\omega_m+\omega_n+\omega)\frac{\tau}{2}}\psi_m^{(0)}(z) \\
& + \left[-\frac{iF_{mn}^*}{\hbar\Omega}e^{i\omega(\tau+T)}\sin\Omega\tau\; C_{m,III}(\tau+T) \right. \\
& \left. + \left(\frac{i\varepsilon}{2\Omega}\sin\Omega\tau + \cos\Omega\tau\right)C_{n,III}(\tau+T)\right] e^{i(+\omega-\omega_m-\omega_n)\frac{\tau}{2}}\; \psi_n^{(0)}(z)\;.
\end{aligned}
$$
(4.45)

Here, $C_{m,III}(\tau + T)$ and $C_{n,III}(\tau + T)$ represent the weights in front of the unperturbed wave functions from equation (4.44) (compare with equation (4.38)). The probability of finding a neutron in state m after region IV is then given by (**Ramsey** (1950))

$$
\begin{aligned}
P_m &= \left|C_{m,IV}(2\tau+T)\right|^2 \\
&= 4\frac{F_{mn}^2}{\hbar^2\Omega^2}\sin^2\Omega\tau\left(\cos\frac{\varepsilon}{2}T\cos\Omega\tau - \frac{\varepsilon}{2\Omega}\sin\frac{\varepsilon}{2}T\sin\Omega\tau\right)^2\;.
\end{aligned}
$$
(4.46)

For arbitrary parameters, the behaviour of equation (4.46) is shown in figure 4.1, where the probability of a neutron being in state n, $P_n = 1 - P_m$, after region IV is shown. Typical Ramsey fringes arise.

For this derivation, one aspect of the qBOUNCE experiment was not taken into account: The initial states ψ_k (equation (4.10)) potentially exhibit a phase factor $e^{-i\phi_k}$. For a two state system, a phase difference $\phi_{mn} = \phi_m - \phi_n$ arises, yielding a

---

[5]Neglecting steps between mirrors and waviness of the mirrors' surfaces.
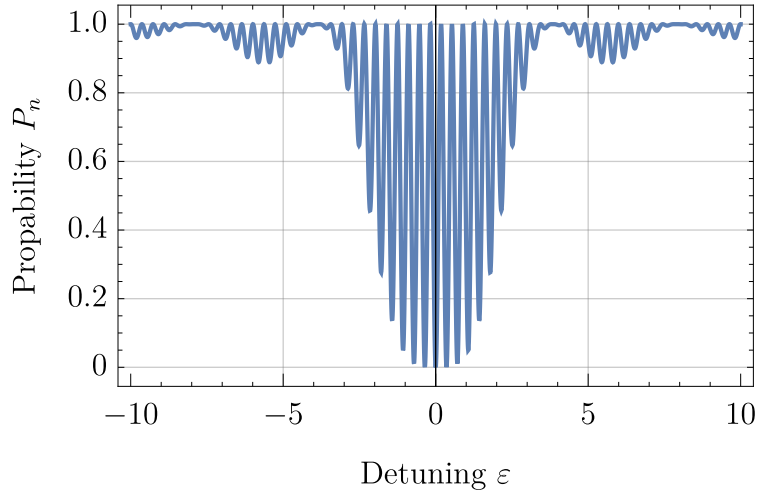
Figure 4.1.: Typical Ramsey fringes show the results derived. Here, the length of the intermediate region of free evolution was chosen to be 10 times the length of one perturbation region. A relative transmission of one corresponds to a transmission of the setup with all neutron mirrors at rest.

phase factor $e^{-i\phi_{mn}}$. As this phase difference is not measurable in the experiment, this phase is integrated over in the final result of the wave function. For the probabilities of finding the neutron in a certain state, this phase vanishes in any case by taking square of the absolute value of the wave function.

Close to resonance, $\omega - \omega_{mn} \ll \omega$, and equation (4.46) becomes (**Riehle** (2004))

$$P_m \approx \frac{1}{2} \sin^2 \frac{F_{mn}}{\hbar} \left(1 + \cos 2\pi(\omega - \omega_{mn})T\right) \ , \tag{4.47}$$

out of which the full width at half maximum of the resonance curve can be calculated to be

$$\Delta\nu = \frac{1}{2T} \ . \tag{4.48}$$

This shows that the energy resolution of the setup is depending on T, and therefore the length L of region III.

Phase Difference Between the Oscillating Regions II and IV

Experimentally, the phase difference between the oscillating regions has to be known. Often, a phase difference is unwanted and poses a systematic effect that needs to be investigated. However, as will be shown in the next section, some measurement schemes are based on the tuning of the relative phase difference in regions II and IV. The corresponding transition probabilities and a resulting shift of the resonance frequency shall therefore be provided in the following.

For a phase difference η between the oscillating regions II and IV, the resonance frequency $\nu_{mn} = \frac{\omega_{mn}}{2\pi}$ shifts. From (**Riehle** (2004))

$$P_m \approx \frac{1}{2} \sin^2 \frac{F_{mn}}{\hbar} \left(1 + \cos 2\pi(\omega - \omega_{mn})T + \eta\right) , \qquad (4.49)$$

and the phase sensitivity is obtained as

$$\frac{\Delta\nu_\eta}{\nu_{mn}} = -\frac{\eta}{2\pi\nu_{mn}T} . \qquad (4.50)$$

Suppose a phase shift η occurs in the second perturbation region of a Ramsey setup within qBOUNCE. In the wave function after region IV (equation (4.45)), the terms $\omega(\tau + T)$ are replaced by $\omega(\tau + T) + \eta$ (**Ramsey** (1986)). The wave function therefore becomes

$$\begin{aligned}
_\eta\psi_{IV}(z, 2\tau + T) = &\left[-\frac{iF_{mn}^*}{\hbar\Omega} e^{-i\left(\omega(\tau+T)+\eta\right)} \sin\Omega\tau \; C_{n,III}(\tau + T) \right.\\
&\left. + \left(-\frac{i\varepsilon}{2\Omega} \sin\Omega\tau + \cos\Omega\tau \right) C_{m,III}(\tau + T) \right] e^{-i(\omega_m+\omega_n+\omega)\frac{\tau}{2}} \psi_m^{(0)}(z)\\
&+ \left[-\frac{iF_{mn}^*}{\hbar\Omega} e^{i\left(\omega(\tau+T)+\eta\right)} \sin\Omega\tau \; C_{m,III}(\tau + T) \right.\\
&\left. + \left(\frac{i\varepsilon}{2\Omega} \sin\Omega\tau + \cos\Omega\tau \right) C_{n,III}(\tau + T) \right] e^{i(+\omega-\omega_m-\omega_n)\frac{\tau}{2}} \psi_n^{(0)}(z) .
\end{aligned}$$
$$(4.51)$$

Again, the probability of finding a neutron in state m after region IV is then given by (**Ramsey** (1986))

$$\begin{aligned}
_\eta P_m &= \left|_\eta C_{m,IV}(2\tau + T)\right|^2\\
&= 4\frac{F_{mn}^2}{\hbar^2\Omega^2} \sin^2\Omega\tau \left(\cos\frac{1}{2}(\varepsilon T - \eta) \cos\Omega\tau - \frac{\varepsilon}{2\Omega} \sin\frac{1}{2}(\varepsilon T - \eta) \sin\Omega\tau \right)^2 ,
\end{aligned}$$
$$(4.52)$$

which near a resonance reduces to

$$_\eta P_m = \sin^2 \frac{2F_{mn}}{\hbar}\tau \cos^2 \frac{1}{2}(\varepsilon T - \eta) . \qquad (4.53)$$

Therefore, varying η close to, or on resonance will yield a sinusoidal behaviour. This will be shown in the next section and is an important result to interpret the experimental realisation of Ramsey's method within qBOUNCE in section 9.6.

5. Investigation of Ramsey's Method within *q*Bounce

Within this chapter, the results derived in section 4.2 shall be analysed with experimental parameters used in the first realisation of Ramsey's method within *q*BOUNCE. The first section 5.1 starts with considering the chosen lengths of the five mirrors for the first realisation of a Ramsey setup within *q*BOUNCE. Results after convolution with the velocity spectrum as well as after taking the measured state population after regions I and V into account, are presented in section 5.2. Sections 5.2.1 and 5.2.2 discuss measurement techniques with a Ramsey setup within *q*BOUNCE.

5.1. Mirror Dimensions of First Realisation

The number of Ramsey fringes (dips between two subsequent maxima in the oscillatory behaviour of the transmission) shown in figure 4.1 of the previous chapter is only achievable with large times T. This corresponds to a long free evolution of the neutrons in region III (of length L) of a Ramsey setup. For the first realisation within *q*BOUNCE, T is about 2.2 times τ (neutron flight time for length l of one perturbation region). Mirror lengths of $l = 152\,\text{mm}$ and $L = 340\,\text{mm}$ were chosen. The corresponding fringes for these lengths of neutron mirrors are shown in figure 5.1. A transmission of one corresponds to the transmission with all neutron mirrors at rest.

Interesting cases to look at are the ones for varying T and τ times, or $l = v_n\tau$ and $L = v_nT$. Figure 5.2 shows the effect of varying L. Starting from $L = 0$, this equals a Rabi-type setup with the two oscillating mirrors acting as one large mirror of double length. As L increases up until two times the length used in the experiment, more and more side fringes arise and the middle peak becomes sharper. These two effects are both desirable, as they both increase the sensitivity of a theory function that is fitted to the data.

Varying l mainly has effects on the side fringes. For shorter l, more side fringes arise, although it should be noted that this also increases the oscillation amplitude needed to drive a $\frac{\pi}{2}$-flip (compare with equation (4.32)).
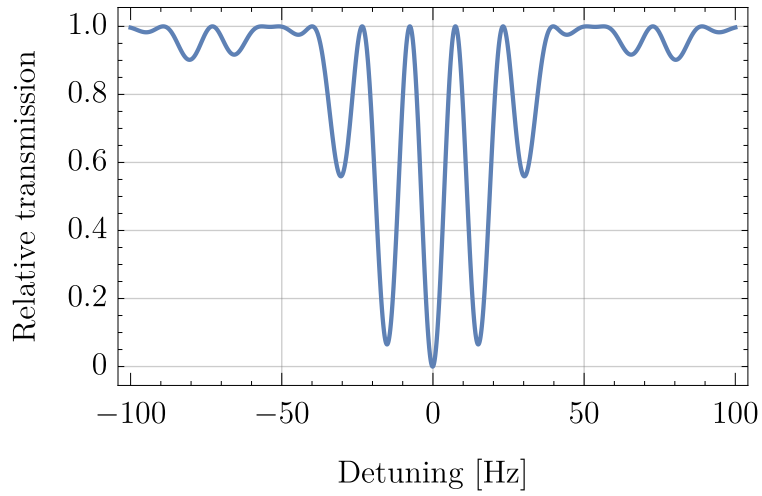
Figure 5.1.: Ramsey fringes for neutron velocities $v_n = 8\,\mathrm{m/s}$, and lengths $l = 152\,\mathrm{mm}$ and $L = 340\,\mathrm{mm}$ for the perturbation regions II and IV, and the middle region III, respectively. The detuning is the difference between resonance frequency (in this case $392.566\,\mathrm{Hz}$ for $|2\rangle \rightarrow |4\rangle$) and frequency of the perturbation regions. The oscillation amplitude of the perturbation regions is $1.3\,\mathrm{mm/s}$.
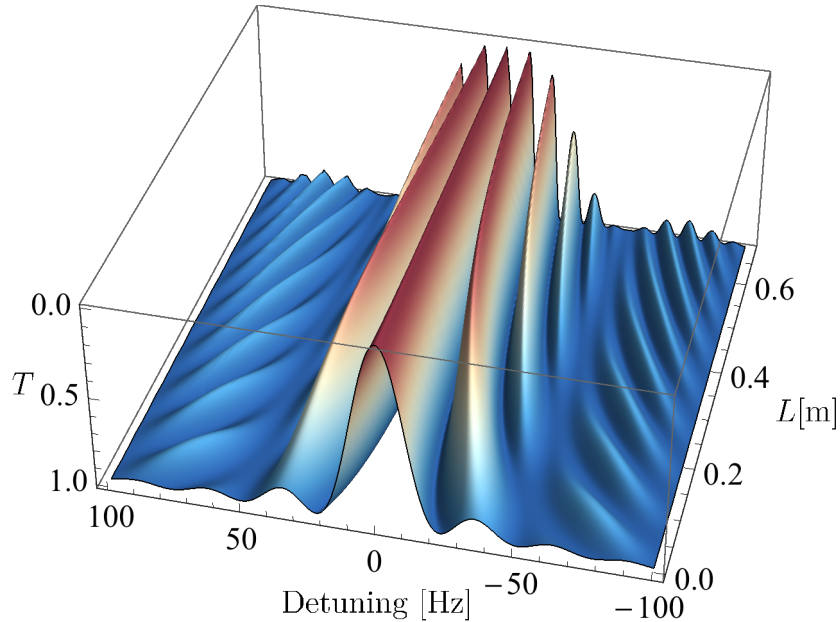
Figure 5.2.: Transition probability for a Ramsey setup with varying length of free propagation L. For better visibility, the relative transmission T is shown inverted. For $L = 0$, a Rabi curve results. Other parameters are as stated in figure 5.1.

5.2. Measured State Population and Convolution with Velocity Spectrum

A particular strength of a Ramsey-type setup is that a broad velocity spectrum of the incoming neutrons can be used. Although side fringes of the Ramsey pattern will smear out, the middle peak (or dip, in terms of count rates), is very robust. For *q*BOUNCE this poses a major advantage, as a broader velocity spectrum yields higher count rates.

This section includes realistic state populations after region I and V, and takes the measured velocity spectrum of the incoming neutrons into account for simulations. The population of states after the mirror-absorber systems is velocity-dependent. Nevertheless, the effects of convolution with the velocity spectrum as well as the influence of the state occupation will be shown separately at times within this section.

This section also anticipates measurements of the incoming velocity distribution of the neutrons (5–13 m/s) that are presented in section 9.2, and measurements of the occupation of states after regions I and V (section 9.3). The state occupation after regions I and V for states one, two and three, respectively, are 50 %, 40 %, and 10 %. Exact values of the parameters are listed in table 9.2 and will be used with the theoretical equations derived in chapter 4.

The graphs to follow will show that the occupation of eigenstates is currently a limiting factor. The state selection is done with a mirror-absorber system (see section 8.1.2 and measurements in section 9.3), which in 2017 did not perform as well as in earlier measurements.[1] This issue is presently being analysed and is work in progress. Improvements on the state selection (increasing the occupation of the ground state) will strongly increase the achieved contrast.

Because of the third energy state still being present after individually measuring the wave functions behind preparation and analysis region, the transition of choice for a first realisation (and for all investigations within this chapter) is the one from the second to the fourth energy state: $|2\rangle \to |4\rangle$. The transition $|1\rangle \to |4\rangle$ would yield higher contrast, but is difficult to realise at the moment due to mechanical resonances of components at the transition frequency.

Figure 5.3 shows the expected Ramsey pattern for transition $|2\rangle \to |4\rangle$. If only the measured velocity distribution is taken into account and perfect preparation of the ground state is supposed, the contrast is over 80 %. Considering also the measured state occupation from 2017, the contrast drops significantly. Because only states $|2\rangle$ and $|4\rangle$ are taken into account for calculating the transition probability P, the transmission T is normalised with respect to all present states as follows, where b_i and c_i are the occupation numbers measured after region I

---

[1] In **Cronenberg** (2016), the occupation of the first, second, and third energy state, were approximately 60 %, 34 %, and 6 %, respectively.
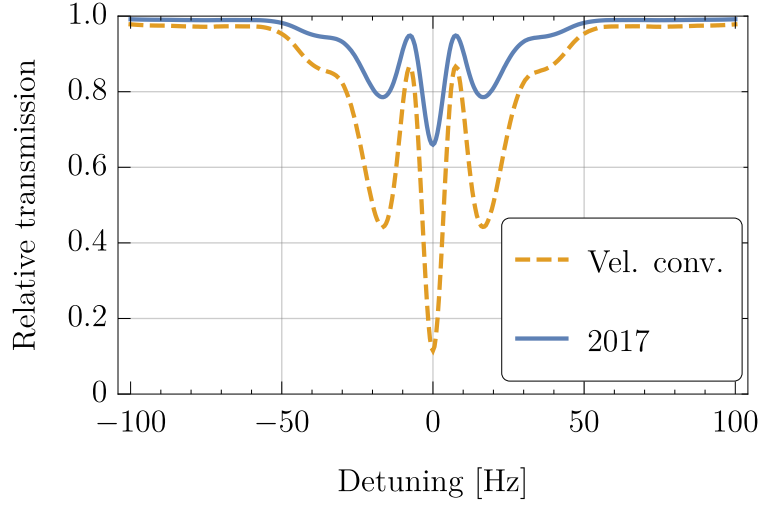
Figure 5.3.: Theoretical Ramsey fringes for transition $|2\rangle \to |4\rangle$, convoluted with the measured velocity spectrum only (yellow, dashed) and with also the measured state occupation numbers taken into account (blue, solid). While the velocity spectrum mainly only smears out side fringes visible in figure 5.1, adding the state occupation results in a noticeable drop in contrast. The oscillation amplitude is set to $1.35\,\text{mm/s}$.

and V for states i, respectively:

$$
\begin{aligned}
T &= \sum_{i \neq 2,4} b_i c_i + P\, b_4 c_2 + (1-P)\, b_2 c_2 + P\, b_2 c_4 + (1-P)\, b_4 c_4 \\
&= \sum_i b_i c_i + P\,(b_4 c_2 - b_2 c_2 + b_2 c_4 - b_4 c_4) \\
&= 1 + P\,(b_4 c_2 - b_2 c_2 + b_2 c_4 - b_4 c_4) \frac{1}{\sum_i b_i c_i} \ .
\end{aligned}
\tag{5.1}
$$

Although improved state selection will yield better results in the future, reasonable contrast can also be achieved with the mirror absorber systems in use at the moment.

5.2.1. Ramsey-Flop and Amplitude Sweeps

Besides directly measuring Ramsey fringes as a function of detuning as depicted in figure 5.3, there are other measurement schemes that can be made use of in the experiment. This section analyses the tuning (viz. varying) of the oscillation amplitude of the oscillating mirrors, whereas the next section covers the variation of another experimentally accessible parameter: the phase between the oscillating regions.

Equations (4.30) and (4.32) give the probability of finding a neutron in the higher state after applying a Rabi pulse to it, and the condition for a $\frac{\pi}{2}$-flip,
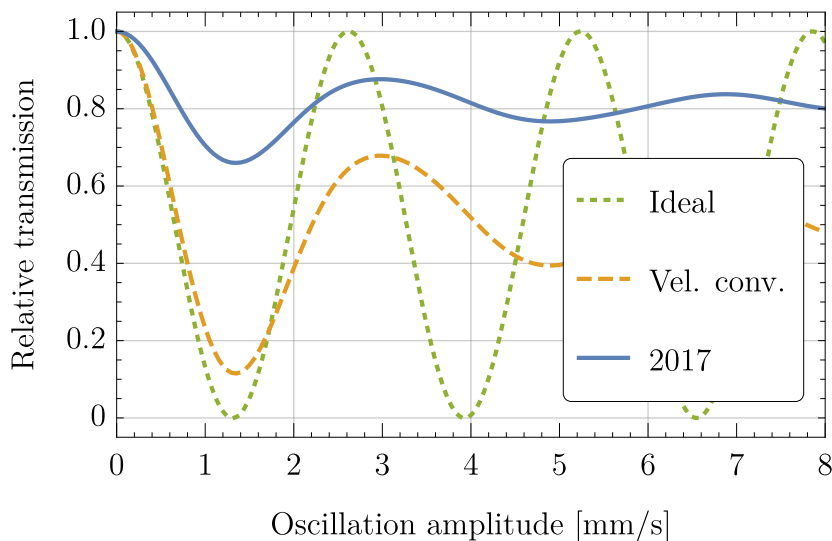
Figure 5.4.: Simulated outcome of the variation of the oscillation amplitude in a Ramsey-setup within *q*BOUNCE. Idealised, for neutrons with velocities of 8 m/s (green, dotted). Taking the velocity distribution of the neutrons into account (yellow, dashed) and then also their state occupation after regions I and V, yields the blue (solid) curve. Still, a clear repopulation of the initial state can be identified at around 3 mm/s.

respectively. These equations show that besides the time span a neutron spends in a perturbation region, the applied amplitude also plays a role. In the plots of the previous sections, this amplitude was optimised for a $\frac{\pi}{2}$-flip for the corresponding velocity or velocity spectrum of the neutrons. However, by increasing the amplitude (just like increasing the length of the region), the occupation probability for the higher state drops again, and the one for the initial state increases. This behaviour is called a Rabi-flop, and can also be applied to a Ramsey-like setup. In the Ramsey case, such behaviour shows that single neutrons that are in a superposition of energy eigenstates after region II stay in a coherent superposition over the length of region III.

Such a Ramsey-flop is depicted in green (dotted) in figure 5.4 (compare with figure 5.1 for the corresponding frequency plot). As the oscillation amplitude increases, the transmission probability for the neutrons oscillates between zero and one in an idealised experiment. This is a very characteristic feature of this quantum mechanical system, and cannot be expected to occur within a classical system (compare section 6.3).

The behaviour changes slightly when a neutron velocity distribution is convoluted with the probability function: The initial transmission rate is not reached anymore, and the oscillatory behaviour is dampened out with increasing oscillation amplitude (yellow, dashed). Taking also the occupation of the states measured in
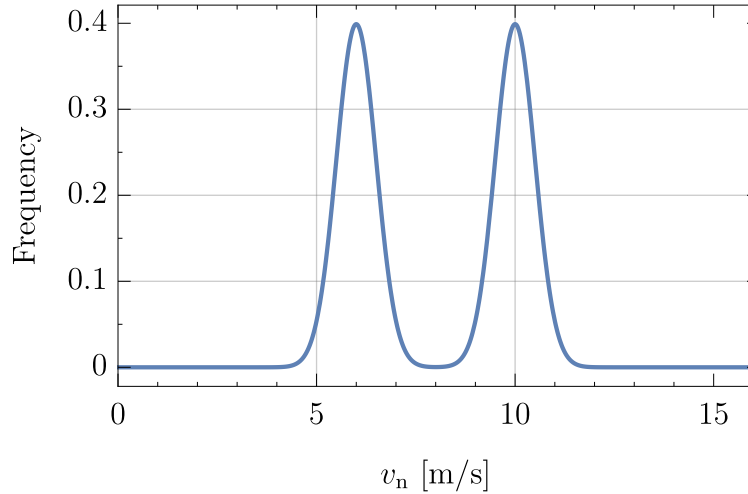
Figure 5.5.: Hypothetical velocity distribution to produce different patterns in an amplitude sweep (figure 5.6). Two normal distributions are joined with mean velocity at 6 and $10\,\mathrm{m/s}$, respectively, with a standard deviation of $0.5\,\mathrm{m/s}$ each.

2017 into account, the contrast drops further (blue (solid) line in figure 5.4). The dampening of the transmission oscillation with increasing oscillation amplitude of the mirrors is an effect due to the phase differences that neutrons of different velocities will experience between the two oscillating regions, as the amplitude can only be optimised for a single velocity. Still, the transmission goes up again after the first minimum at the optimal amplitude to produce a $\frac{\pi}{2}$-flip in each perturbation region.

Measuring a Ramsey-flop in an experiment provides a proof of principle of a Ramsey-setup. This can be readily confirmed by comparing the results just derived with the results from section 6.3, where the classical expectation for a Ramsey-type *q*BOUNCE setup was examined. Experimentally, a Ramsey-flop is convenient because only one single parameter (the oscillation amplitude) needs to be changed.

As the averaging of the transmission rate in a Ramsey-flop is an effect of different neutron velocities involved, it is interesting to investigate the behaviour for hypothetical velocity distributions. Anticipating results from section 9.2, a possible distribution is one with two maxima, as shown in figure 5.5. A distribution similar in shape may be produced experimentally by blocking the path between the velocity selecting blades (compare section 8.1.1) for a certain window of velocities with a sheet or wire made out of a neutron absorbing material. The resulting pattern of an amplitude sweep with a velocity spectrum like this is shown in figure 5.6. After a first minimum slightly above an oscillation frequency of $1\,\mathrm{mm/s}$, a plateau forms, before a second minimum appears at $5\,\mathrm{mm/s}$. It should therefore be noted that more complicated patterns can arise in such amplitude
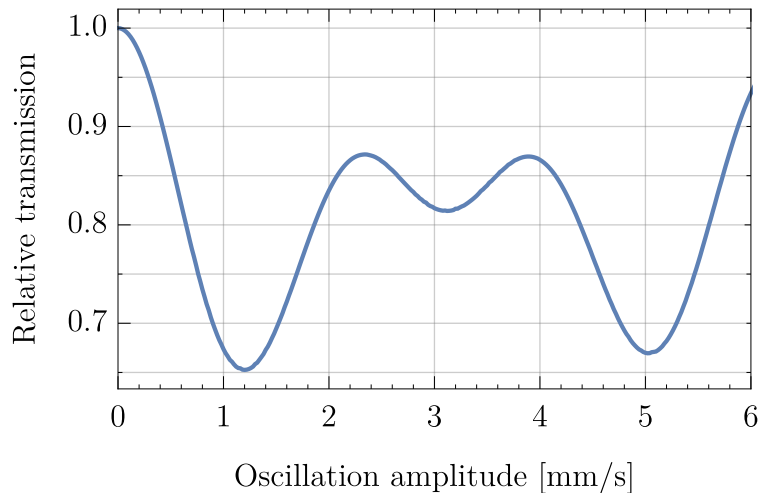
Figure 5.6.: Behaviour of the relative transmission under amplitude sweep for measured state occupations after regions I and V, but with the hypothetical velocity spectrum shown in figure 5.5. A plateau forms between the first, and a second minimum at $5\,\mathrm{mm/s}$.

sweeps, and that a proper measurement of the incoming neutron velocity spectrum is crucial.

5.2.2. Phase Sweep

Experimentally also convenient is to keep the oscillation amplitude of the interaction regions at optimum for a given velocity spectrum, and vary their relative phase. In contrast to the amplitude sweep, a full inversion to the initial zero transmission rate is possible for a two-state system. Starting at optimal resonance with zero phase difference, the count rate will rise up to one again, at a phase difference of 180° (figure 5.7). The graph again takes the measured velocity distribution as well as measured state occupations after preparation and analysing region into account. When the oscillating regions are in phase opposition, no matter how far a transition from initial to final state is driven within the first interaction region, the second interaction region reverts this process exactly. Therefore, this process is not dependent on the velocity distribution.

Again, **measuring such behaviour is evidence for the setup being of Ramsey-type.** The classical expectation from section 6.3 shows very little influence of the phase change applied, while the quantum mechanical Ramsey case lets the transmission rate oscillate (see section 4.2). This is only explicable with a phase relation between the superposed energy states after the first perturbation region.

A phase sweep measurement of the Ramsey GRS setup presented within this thesis is shown in section 9.6.
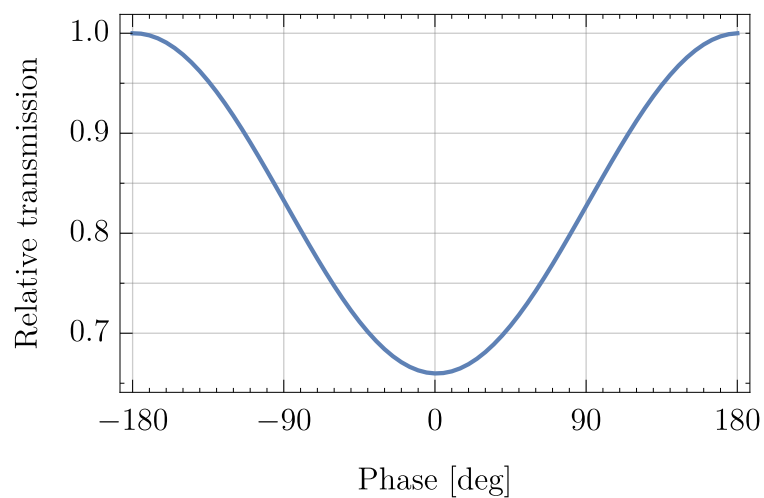
Figure 5.7.: By varying the phase difference between the oscillation regions II and IV at optimal oscillation amplitude, a clear sinusoidal behaviour of the transmission rate can be observed. The zero rate is restored when the oscillating regions have opposite phase. A velocity distribution of 5–13 m/s (see figure 9.3) and a state occupation after regions I and V of around 50 %, 40 %, and 10 % for the first, second and third eigenstate are used (see table 9.2 for exact numbers).

6. Simulations of Classical Particles in a Ramsey-Setup

In order to distinguish the (quantum mechanical) results of the Ramsey-type qBounce experiment from the classically expected behaviour, it is necessary to investigate the behaviour of a classical Bouncing Ball (cBB) above oscillating surfaces.

While the underlying physics of the cBB are (in the approximations applicable) elementary and well understood, the behaviour of a ball bouncing along an arrangement of oscillating and static surfaces is ad hoc non-trivial. Different types of possible trajectories such as periodic behaviours, sticking solutions, or chaotic behaviour are possible and highly dependent on the initial conditions. Therefore, Monte Carlo simulations have been performed for parameter sets as used in the experiment.

After introducing the system under consideration in section 6.1, the simulations are exemplified in section 6.2 and the results are presented in section 6.3.

6.1. Dynamics of a Classical Bouncing Ball

A ball (neutron) is falling down on a flat surface (a neutron mirror) that can either be at rest or oscillating. Accordingly, the subsequent trajectories after impact evolve. In the following, several approximations are used:

- Neutrons are point-like particles,
- the impact upon the surface is instantaneous and elastic,
- the mass of the moving surface is much greater than the mass of the neutron,
- the oscillating surface is flat and levelled,
- gaps between aligned mirrors are neglected.

Adapting the notation used in **Chastaing et al.** (2015), u_n^+ and u_n^- represent the velocity of the neutron before and after impact, respectively, of the nth collision with the mirror at time $t = t_n$ (see figure 6.1). Therefore, the neutron's height above the mirror, $h(t)$, before the first collision with the mirror is is given by

$$h(t) = h_{\text{initial}} + u_{\text{initial}}(t - t_{\text{initial}}) - \frac{g}{2}(t - t_{\text{initial}})^2 \,, \tag{6.1}$$

where h_{initial} and u_{initial} are height and vertical velocity of the neutron at initial time t_{initial}, and g is the Earth's gravitational acceleration. For a mirror at rest at height zero, the time of first impact t_n can be calculated by solving equation (6.1)
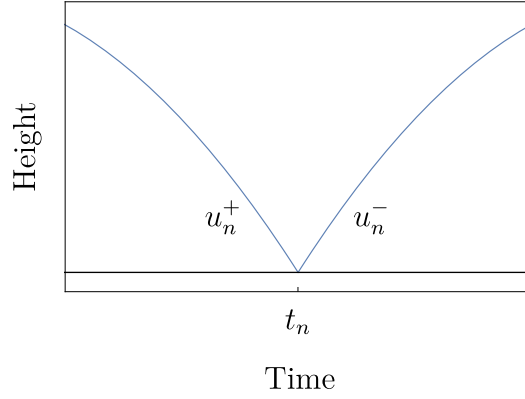
Figure 6.1.: Sketch clarifying the nomenclature of neutron velocities before impact (u_n^+), and after impact (u_n^-), respectively. The neutron is bouncing from left to right.

for t_n with $h(t) = 0$, while for a sinusoidal oscillating surface with amplitude A the implicit equation

$$A(\sin(\omega t_n + \phi_0) + 1) = h(t) \,, \tag{6.2}$$

with $h(t)$ from equation (6.1), contains the desired information. At $t = t_{\text{initial}}$, the phase ϕ_0 is inherently undetermined. The constant term in the bracket on the left-hand side defines the offset A of the surface's oscillation. The implicit equation (6.2) can be solved numerically for the time t_n at which the first impact occurs. Given t_n, u_n^- can be obtained:

$$u_n^- = u_{\text{initial}} - g(t_n - t_{\text{initial}}) \,. \tag{6.3}$$

For the entirely elastic case and for the mirror at rest, $u_n^+ = -u_n^-$ is trivial. For the oscillating mirror, we have

$$u_n^+ = 2A\omega \cos(\omega t_n + \phi_0) - u_n^- \,, \tag{6.4}$$

as well as the height of the neutron at impact,

$$h_n = A(\sin(\omega t_n + \phi_0) + 1) \,. \tag{6.5}$$

With known t_n, h_n and u_n^+, the next flight trajectory of the neutron after impact is determined. The time of the next bounce t_{n+1} can be calculated again by solving an equation like equation (6.2) with the parameters just obtained:

$$A(\sin(\omega t_{n+1} + \phi_0) + 1) = h_n + u_n^+(t_{n+1} - t_n) - \frac{g}{2}(t_{n+1} - t_n)^2 \,. \tag{6.6}$$

Like this, arbitrary numbers of bounces can be calculated iteratively.

While this solution only accounts for the vertical movement of the neutron, the horizontal velocity of the neutron bouncing over a setup of different mirrors can

Table 6.1.: Parameters used for the simulation of the classical trajectory in figure 6.2.

A	ω	ϕ_0	h_{initial}	u_{initial}	$u_{\text{horizontal}}$
0.5 µm	392.566×2π 1/s	0 rad	10 µm	0 m/s	8 m/s
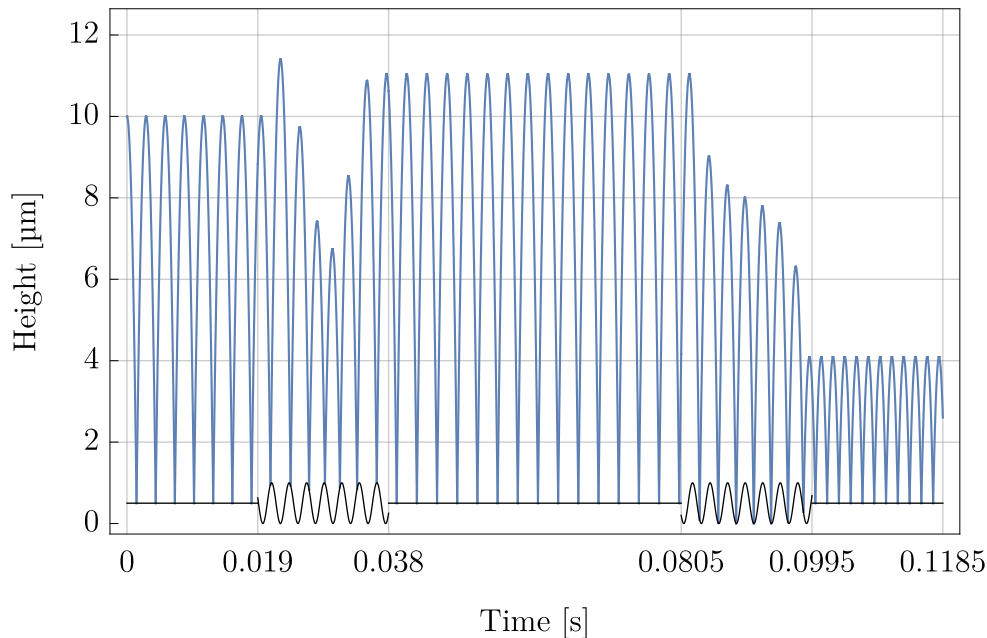
Figure 6.2.: Simulated classical trajectory for a neutron bouncing along a Ramsey-type mirror setup. One set of initial parameters (table 6.1) was chosen to visualise some of the possible effects.

be parameterised through the time the neutron bounces along each individual mirror. For one set of parameters (listed in table 6.1), figure 6.2 shows a neutron entering region I of a *q*BOUNCE Ramsey-setup from the left and exiting on the right-hand side after region V. The lower black line (straight and oscillating) represents the mirror position at each time, whereas the upper blue line shows the neutron's trajectory. Upon entrance in the oscillating region II, first, upwards acceleration of the neutron through collision with the mirror can be observed, followed by subsequent dampening and again acceleration. Although not too surprising, it is noteworthy that a neutron can exit the setup at a lower height than its entrance height.

Further interesting effects like sticking solutions, where the neutron can very tightly follow the oscillating mirror's trajectory, or losses from neutrons hitting a mirror from the side at intersections (accounted for in the simulations), can be studied with the procedure presented.

6.2. Simulations of a Classical Bouncing Ball within *q*Bounce

Less intuitive than the findings just presented is the behaviour of the introduced system when all possible initial conditions and the consequential trajectories are considered and averaged. As argued above, it is of particular interest to simulate outcomes of certain measurement schemes in order to distinguish quantum mechanical results from classical expectations. Therefore, two of those measurements shall be covered and the outcome of their classical simulations presented here: A Ramsey-flop (measuring the transmission while subsequently increasing the oscillation amplitude in region II and IV) and a phase sweep (measuring the transmission while subsequently varying the phase between the oscillating regions II and IV). The simulations are covered in this, and the corresponding results will be displayed in the next section.

The free parameters, which influence the neutron's trajectory shown in the previous section and which change during an experiment, are the neutron's entrance height h_{initial} into region I, its initial vertical velocity u_{initial}, its velocity in flight direction $u_{\mathrm{horizontal}}$, and the global phase of the oscillating mirrors upon entrance of the neutron in region I, ϕ_0.[1]
All of these parameters follow certain distributions. In a Monte Carlo-like approach, for every set of fixed parameters (like oscillation frequency and amplitude, and the slitwidth between the absorbers and mirrors in region I and V for a Ramsey-flop simulation at one oscillation amplitude) the simulations sample the free parameters randomly according to their underlying distributions. For h_{initial}, a uniform distribution from mirror to absorber height is reasonable, as also used in **Chizhova et al.** (2014). Clearly, also ϕ_0 is evenly distributed between 0 and 2π, and a measured velocity distribution like the one shown in section 9.2 is used for $u_{\mathrm{horizontal}}$. For u_{initial}, one has to be slightly more careful. The velocities allowed depend on h_{initial} and the slitwidth S between mirror and absorber in region I. As neutrons that touch the absorber will be scattered out of the system, the neutrons' vertical velocity is limited in the positive as well as the negative direction. This boundary condition leads to

$$u_{\mathrm{max\downarrow}}(h_{\mathrm{initial}}) = -u_{\mathrm{max\uparrow}}(h_{\mathrm{initial}}) = -g\sqrt{\frac{2(A + S - h_{\mathrm{initial}})}{g}}, \qquad (6.7)$$

which is illustrated in figure 6.3a for $S = 22\,\mu\mathrm{m}$.[2] For every incoming neutron at specific height, its initial vertical velocity is sampled from within the grey area shown. Figure 6.3b shows a histogram of the resulting distribution of velocities

---

[1] This phase corresponds to the entrance time of the neutron in region I, relative to the position of the oscillating regions. This is not to be confused with the phase between the oscillating regions II and IV.

[2] This only holds if the neutrons bounce at least once in region I, at a distance smaller or equal to the length of the mirror, which is fulfilled for the horizontal velocities given.
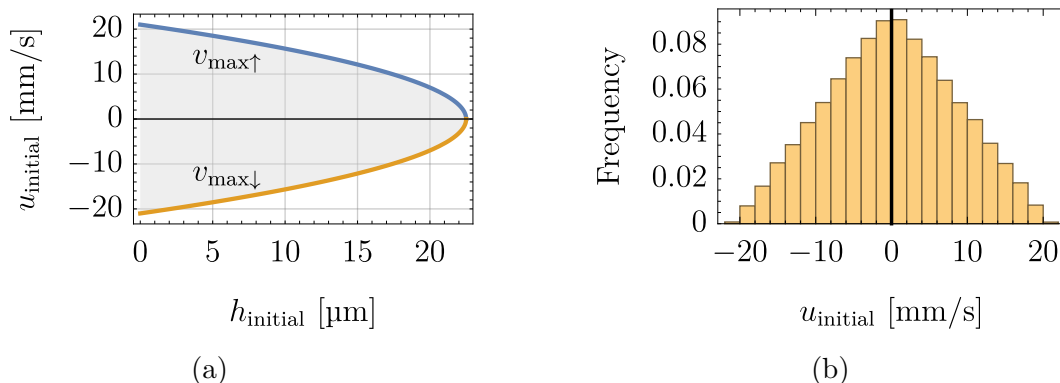
Figure 6.3.: Allowed vertical initial velocities (grey) for given initial height (a) and the resulting histogram used for sampling simulations (b).

used in the simulations.[3]

  With the distributions of the free parameters given and for a set of fixed parameters chosen, randomly generated initial parameters are used to calculate a number of trajectories N. Every trajectory follows a neutron from region I to the end of region IV, at which the simulation outputs the neutron's height h_{out}, and its velocity u_{out}. This means that for every simulation of N neutrons, a histogram of the neutrons' height after region IV can be calculated, which illustrates the global behaviour of the system. In a last step, the question is how many of the arriving neutrons at the analyser (mirror-absorber system with slitwidth S) make it through to the detector. Besides rejecting neutrons, which do not fulfil $A < h_{\text{out}} < S + A$, again equation (6.7) is used to reject neutrons, which do not fulfil $|u_{\text{out}}| \leq |u_{\text{max}}|$, which results in a number for the surviving neutrons N_{alive}. Neutrons hitting a mirror from the side at intersections are accounted for and do not add to this number. Thus, for an experiment measuring transmission rates, every simulation with N sets of initial parameters (N neutrons), drawn from given initial distributions, yields a transmission T via

$$T = \frac{N_{\text{alive}}}{N} \, . \tag{6.8}$$

For all simulations, the approximate velocity distribution measured in 2016 and presented in section 9.2, and $g = 9.805 \, \text{m/s}$ is used.

  The **error bars** shown the next section's results are to be understood statistically, being $1/\sqrt{N}$. That this is valid and that the transmission rates are normally distributed is exemplified in figure 6.4.

---

[3]Technically, this changed for every single amplitude of the oscillating mirrors, as initial heights range from A to $S + A$, because of the mirrors oscillating symmetrically around A.
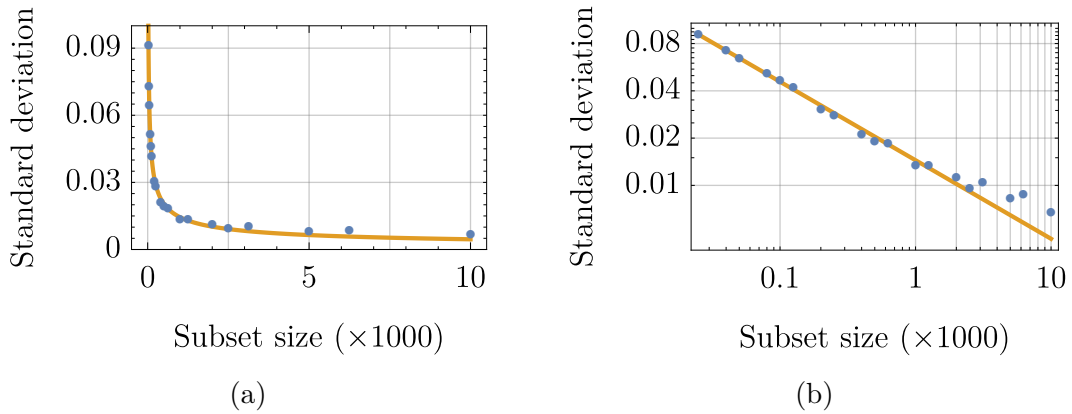
Figure 6.4.: Shown are standard deviations from a transmission rate from a simulation (blue dots). Out of a set of 50.000 iterations, smaller subsets were taken with varying size, yielding different standard deviations. As the subset size increases, the data follows a $\propto 1/\sqrt{N_{\text{subset}}}$ behaviour, as shown by the yellow solid line. The graphs are plotted linearly (a) and in log-log scale (b), and show the same dataset.

6.3. Results of the Simulations

Simulations have been performed for the measurement scheme of an amplitude sweep of the oscillating regions II and IV, as well as for a phase sweep between those regions. The oscillation frequency is chosen to be $392.566\,\text{Hz}$ (which corresponds to the frequency for the quantum mechanical transition $|2\rangle \rightarrow |4\rangle$). For each fixed oscillation amplitude, between 10,000 and 50,000 trajectories have been simulated, and the transmission rate was calculated according to equation (6.8). For the **amplitude sweep**, the phase difference between the oscillating regions is kept at zero, and the corresponding graph is displayed in figure 6.5. The transmission is normalised to the total number of simulated trajectories for each data point. In the quantum mechanical case, an initial drop in transmission rate stops at around $0.6\,\mu\text{m}$ in this case, and is restored to a certain amount at higher amplitudes (compare with figure 5.4). No such behaviour is found in the classical simulation and the transmission keeps declining (suggested by both, linear and quadratic fits).

A simulation of particles bouncing classically through a qBOUNCE setup with **varying phase between the oscillating regions** is shown in figure 6.6. The oscillation displacement amplitude is $A_x = 0.5\,\mu\text{m}$, which corresponds to an amplitude of around $A_v = 1.23\,\text{mm/s}$ in terms of oscillation velocity. Although some variation in the transmission due to the phase difference can be identified, the scale on the vertical axis shows that the effects are very small. No significant indication of a change in transmission rate can be found, even for the extreme cases of total phase inversion of the two oscillating regions at $\pm 180°$. As in the simulation of the amplitude sweep, the classical simulation for the phase sweep
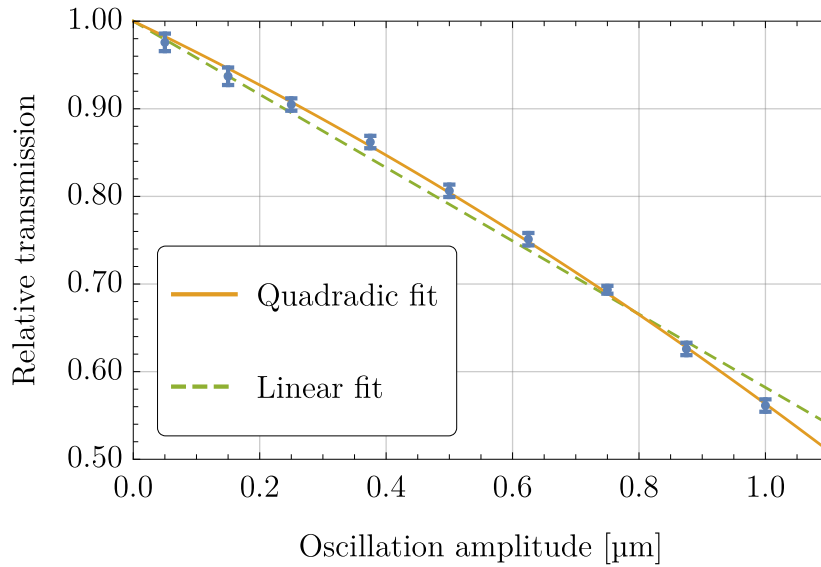
Figure 6.5.: Simulation of an amplitude sweep for a classical particle in a *q*BOUNCE Ramsey setup. The oscillation frequency of the interaction regions is 392.566 Hz, their relative phase zero degrees. The error bars represent statistical errors only.
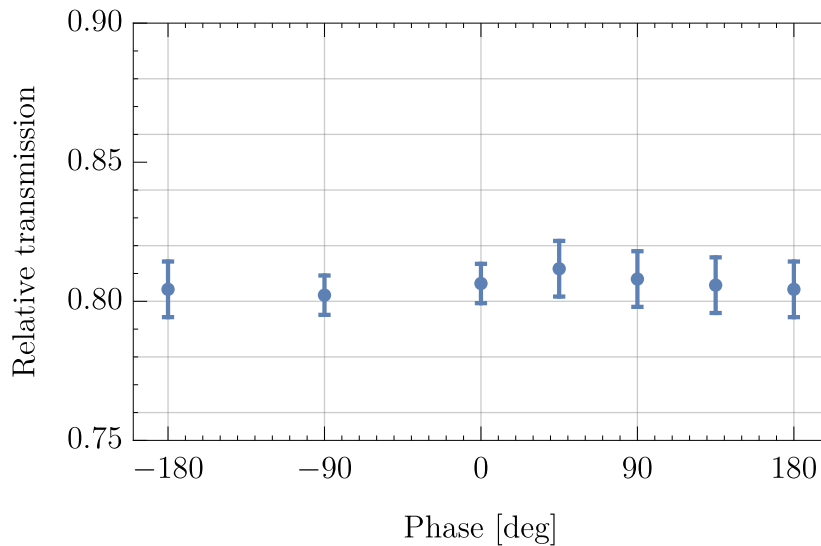
Figure 6.6.: Simulation of a phase sweep for a classical particle in a *q*BOUNCE Ramsey setup. The oscillation frequency is kept at 392.566 Hz, and the relative phase between the oscillating regions varied. Statistical error bars are shown. In contrast to the quantum mechanical prediction, no significant inversion of the transmission rate at ±180° can be identified.

clearly distinguishes from the quantum mechanical behaviour (compare with figure 5.7).

Part III

Experimental Implementation of Ramsey-Type Gravity Resonance Spectroscopy

7. Instrument Setup and preparative Measurements

7.1. Environmental Conditions at PF2, ILL

A Ramsey-type experimental setup within qBOUNCE as introduced in figure 3.5 and section 3.3.2 consists of a wide range of different components. Some of the changes undertaken on site will be beneficial for other future experiments at PF2. While on site changes will be discussed in this section, the subsequent sections describe the instrument (section 7.2) as well as the experimental setup itself (chapter 8). Figure 7.1 gives an overview of the PF2 and its experimental zones and shows a drawing of the UCN platform on which the experiment takes place. With the turbine of PF2 (figure 7.1a, I) and its experimental areas (figure 7.1a II (UCN), III (MAM) and behind I (EDM) for UCN experiments, as well as IV for VCN experiments) being located directly next to the reactor pool, particular precautions are taken with respect to safety issues. Due to the Fukushima nuclear accident, new safety regulations came into effect during the planning phase of the experiment. Therefore, because of the increased size and weight of the new version of qBOUNCE, earthquake safety regulations had to be considered throughout the design of the instrument. The same regulations also required reinforcements of the support structure of the UCN platform where qBOUNCE is placed on. The structural dynamics of the entire platform with the instrument on top were numerically simulated by an external contractor of the ILL and the installation was found to safely withstand accelerations of 4 g.

Figure 7.2 shows a model[1] of the qBOUNCE instrument on the UCN platform of PF2. The functions of the various components will be described in detail in section 7.2.
The instrument mainly consists of a vacuum chamber of two meter length with a cross section of one by one meter, levelled on three spindle drives, of which two are visible in the sketch. These spindle drives and their supports are the only connection of the vacuum chamber to the platform. Around the vacuum chamber, a specially dimensioned crane is placed for opening and closing the chamber. The crane as well as the vacuum chamber (through the spindle drives) are mounted on a continuous, 30 mm thick aluminium plate (in contrast to previous individual combinations of plates). The placement of the instrument on the platform was

---

[1] All 3D drawings and rendered images within this thesis were created with Autodesk Inventor Professional 2016, Student Version.
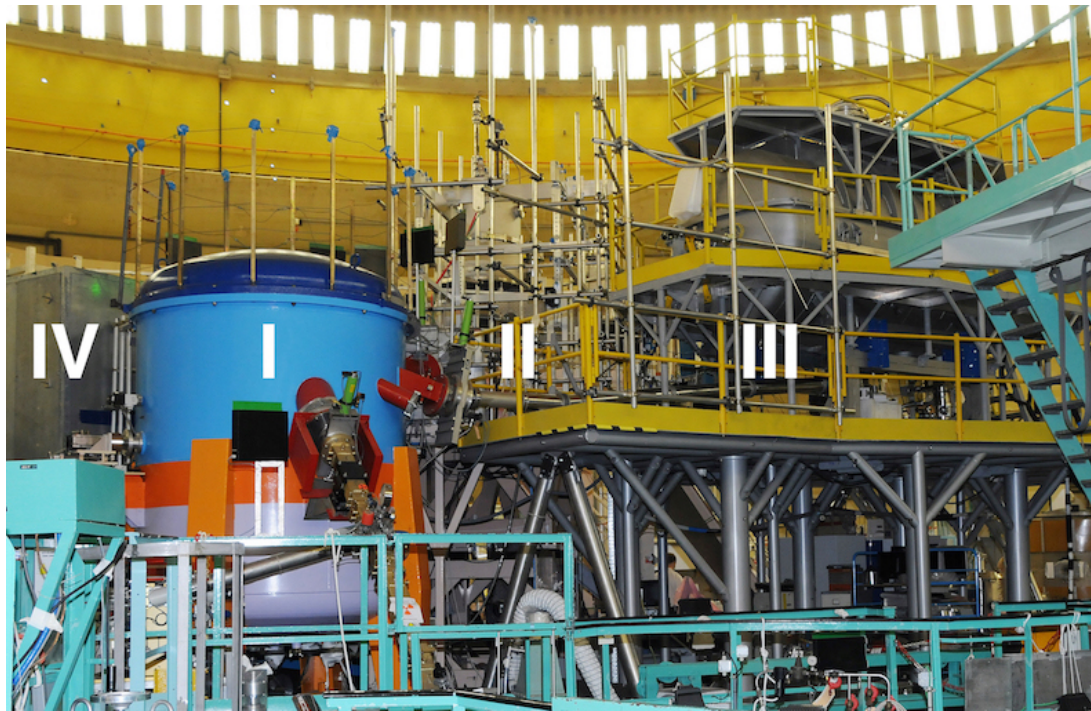
(a)
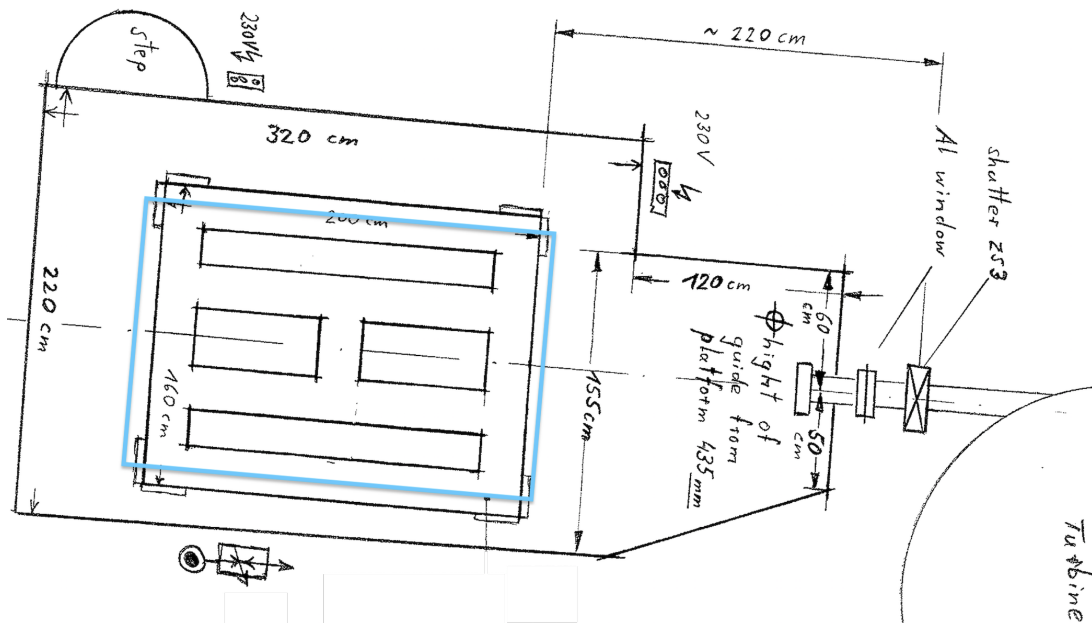
(b)

Figure 7.1.: (a) Photograph (copyright ILL) of the PF2 instrument with several experimental areas visible. Neutrons enter the turbine (I) and either bypass it (VCN, IV), or are guided to the other experiments (UCN — II, VCN — behind II, MAM — III). (b) Drawing of the UCN platform where qBOUNCE is set up (approximate position of the vacuum chamber as as blue rectangle) in top view.
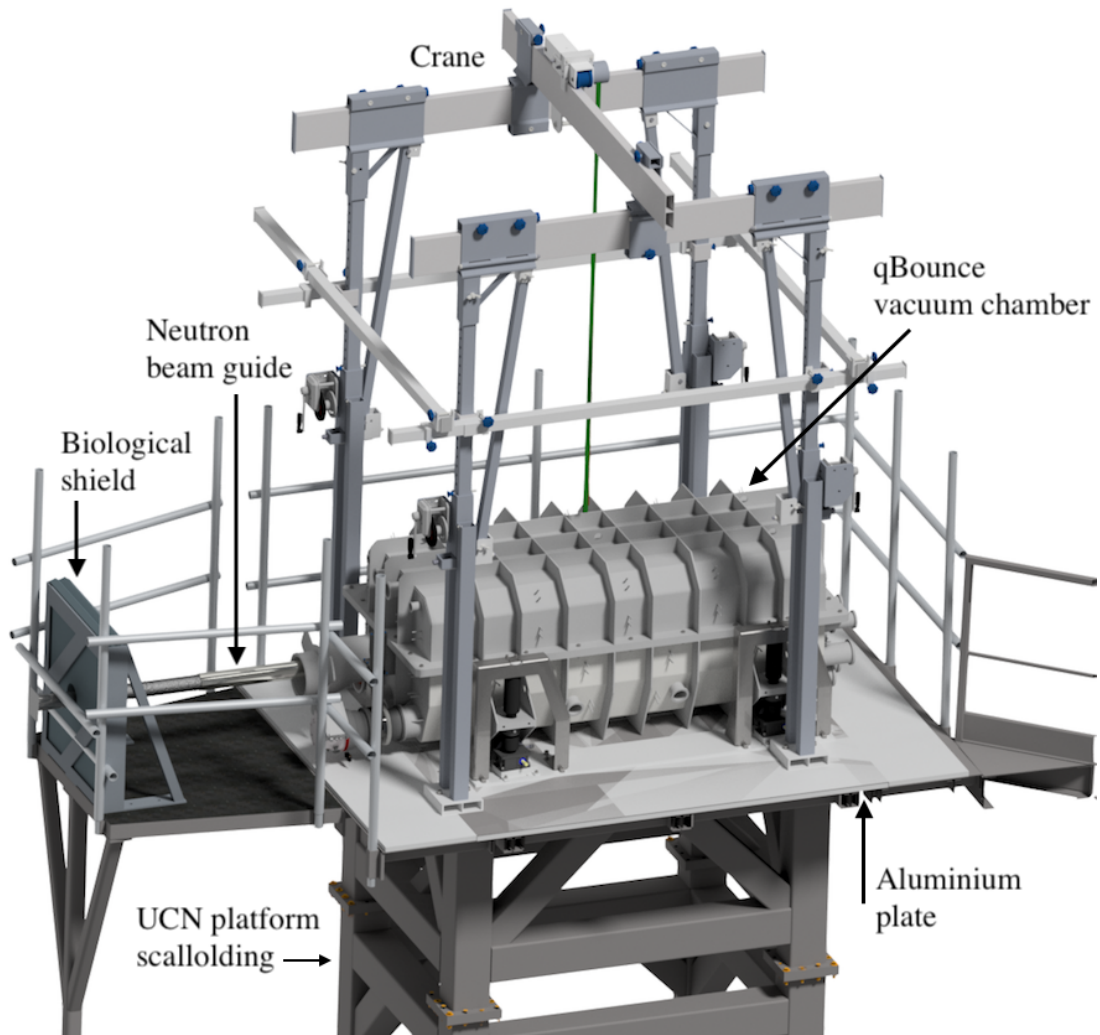
Figure 7.2.: The qBOUNCE instrument on the UCN platform of PF2 as realised.

Figure 7.3.: Additional L-shaped fixing of the vacuum chamber to the UCN platform.

influenced by three major criteria:

- The centre of gravity should lie as centred above the welded scaffolding of the platform as possible,
- the placement has to be compatible with the available lengths of glass neutron guides,
- and the remaining space available around the vacuum chamber has to be sufficient for placement of gear and feedthroughs, as well as to carry out works and adjustments within the vacuum chamber.

The aluminium plate is mounted to the UCN platform with a clamping mechanism that fulfils the requirements of earthquake safety. The qBOUNCE vacuum chamber is, after adjusting the levelling with the spindle drives, mounted to the aluminium plate with a massive fixing, shown in figure 7.3.

The biological shield (see figure 7.4 and compare with the sketch in figure 7.2), which was installed on the UCN platform of PF2, replaces the temporary shields that were installed with the previous qBOUNCE experiments in recent years. It consists of two layers of dovetail pieces of lead, stacked within a support frame of aluminium, which is bolted down onto the platform. Through a hole in the middle, the neutron guide leads UCNs to the corresponding experiment. The size of the shield had to be minimised due to tight weight constraints imposed by earthquake safety rules.

7.2. Instrument setup within *q*Bounce

The new instrument setup of qBOUNCE was planned and constructed with two major goals: upward compatibility and high level of automation. In terms of
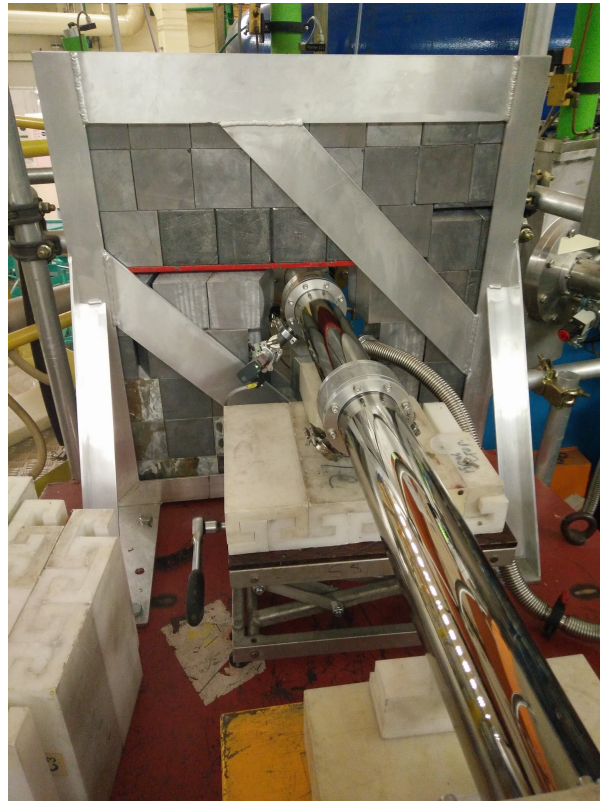
Figure 7.4.: The new biological shield during characterisation measurements of the PF2 UCN beam. The double layer of dovetail lead pieces has a clearance for the neutron beam guide in the middle.
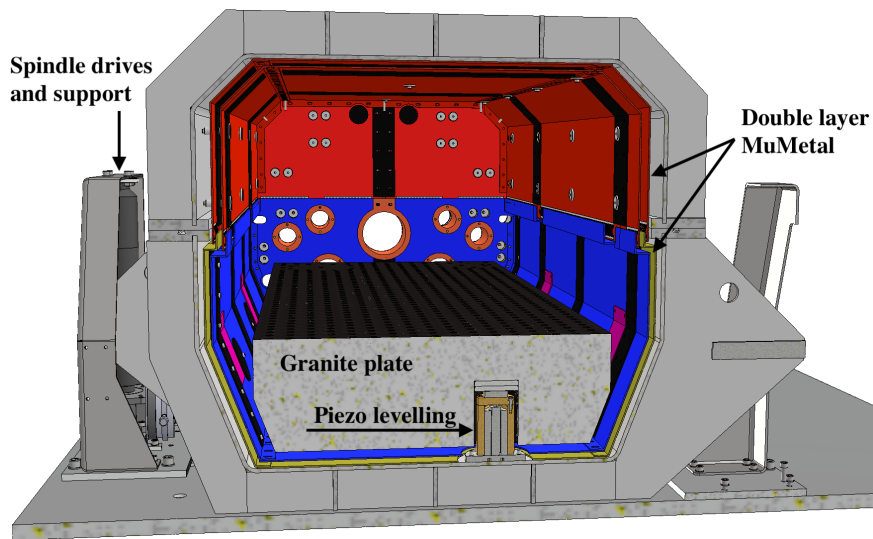
Figure 7.5.: A cut through the *q*BOUNCE instrument with various components visible. The magnetically shielding layers of MuMetal and its mounting and covering components are shown in false colours within the vacuum chamber. One of three piezo actuators levelling the granite plate within the vacuum chamber is visible.

being compatible with future experiments, this essentially means the vacuum chamber as well as the versatility of the instrument should be as large as possible. As can be seen in figures 7.2 and 7.5, the instrument consists mainly of the following components:

- A vacuum chamber with an automised vacuum system, coarse levelled on three spindle drives,
- an integrated magnetic shield,
- a large surface plate made from granite and fine levelled on three piezo-actuators,
- and a crane to open up the vacuum chamber.

The main components and their characterisations, respectively, will be described in the following sections.

7.2.1. Vacuum Chamber

As the neutron's absorption cross section is inversely proportional to its velocity, the mean free path of ultracold neutrons in air is short ($\lambda \approx 20$–60 cm). Therefore, *q*BOUNCE experiments take place within a vacuum chamber. The planning of the vacuum chamber started before the beginning of this thesis, while final designs — especially the layout of threaded bolts placed on the inside and outside of the vacuum chamber — were discussed with the manufacturer[2] as part of this thesis.

---

[2]Trinos / Pfeiffer Vacuum Austria GmbH, Diefenbachgasse 35, A-1150 Wien

Table 7.1.: Feedthrough flange types and corresponding quantities of the vacuum chamber.

Flange	ISO-K 160	ISO-K 100	ISO-K 63	ISO-KF 40	ISO-K 200
Qty	4	10	14	2	1

While the ones on the outside mainly serve as mounting positions for equipment, the ones on the inside are crucial for other instrument components.

The vacuum vessel has an elongated octagonal shape with inner dimensions of about $2100 \times 900 \times 780$ mm. The reason for this geometry is mainly due to spatial limitations on the UCN platform of the PF2. The two parts, top and base, are connected via a single flange with a rubber gasket. The chamber is made of 8 mm thick V2A stainless steel and has support fins all around the outside in order to maintain minimal weight (995 kg without attached parts like feedthrough pipes) with sufficient stability. Feedthroughs in different sizes (see table 7.1) allow for electrical or device connections as well as installation of a pumping system. One feedthrough is special as it serves as inlet for neutron beam guides: a flexible bellow is mounted on an ISO-K 200 flange on the front end (towards the neutron turbine of PF2) of the bottom half of the vacuum chamber. This allows for adjustment in the range of several centimetres as of where the neutron guide enters the chamber (see figure 7.6) and is necessary as the exact alignment of the whole instrument to the axis of the neutron guides is hard to achieve[3]. The bellow can be adjusted and then locked into position via three threaded rods, mounted on the front face of the vacuum chamber. Before a neutron beam guide was fed through the flexible bellow, a deformation test was done while evacuating the vacuum chamber to check for a possible shortening of the system described. This could lead to problems with the neutron guides. The shortening measured on a blank flange mounted on the bellow was 0.47 mm and therefore below the specification of the manufacturer of 0.5 mm.

All around the inner surface bolts are placed for the mounting of the magnetic shielding (see section 7.2.4). Also, on the base of the chamber, three circles of eight M8 bolts are arranged in a triangular shape where piezo elements are mounted (one of them is visible in figure 7.5). On these, the granite surface plate is levelled (see section 7.2.3). As the full weight of the granite plus the experimental setup is loaded on the piezo elements, the resulting stress on the vacuum chamber was analysed carefully by the manufacturer and the dimensioning of the support fins adapted appropriately.

---

[3]In the positioning of the vacuum chamber with respect to the beam tube axis coming from the turbine, there are many factors involved that are subject to uncertainties, e. g.: The positioning of the spindle drives and their support structures that are mounted on the aluminium plate on the platform, the positioning of the aluminium plate itself, or guidance of neutron beam tubes from the neutron turbine to the experiment. Overall precision in the millimetre range is therefore difficult to achieve, and the bellow ensures flexibility in case of slight changes in any component.
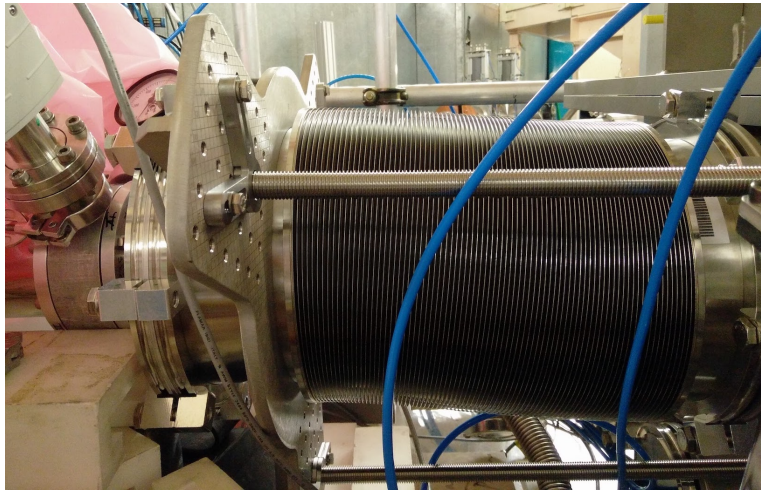
Figure 7.6.: The bellow mounted to the flange for the beam guide inlet allows for adjustments of height (and left/right if necessary) as to where the beam guide enters the vacuum chamber.

Automation of the Vacuum System

For a successful experiment, automation of a high percentage of recurrent processes is vital. Evacuating the experiment volume is a prime example of this class of processes and automation an important issue. Not only saving time between different measurements where the vacuum chamber has to be vented and evacuated again, but maybe even more importantly eliminating possible damages to the system caused by human error, make an automated vacuum system essential.

The vacuum automation box features single buttons for the automatic achievement of the modes "Prevacuum", "High Vacuum", or "Vent" (figure 7.7). The corresponding valves are automatically switched by a programmable logic controller[4]. A schematic view of the vacuum system[5] is displayed in figure 7.8. Prevacuum in the vacuum chamber can alternatively be achieved via a second bypass that allows for adjustable slow pumping. This is useful in case of mechanically sensitive components within the vacuum chamber. See **Gruber** (2016) for further details.

A cut from a typical pressure curve with the setup described above for evacuating the vacuum chamber during an experimental cycle at the ILL is shown in figure figure 7.9. A pressure of 10^{-3} mbar is reached after 13.5 min of pumping. This is a pressure at which UCN measurements can easily be performed in terms of mean free path.[6]

---

[4]A Siemens LOGO! 24RCE with two expansion modules DM 24R.

[5]Pumps in use are an Edwards multi stage roots roughing pump iXL120 and a turbomolecular pump HiPace 700 M by Pfeiffer Vacuum.

[6]Nevertheless, it is desirable to achieve higher vacuum not only to further reduce possible neutron mirror contamination, but because the vacuum pressure affects certain limits on hypothetical particles.
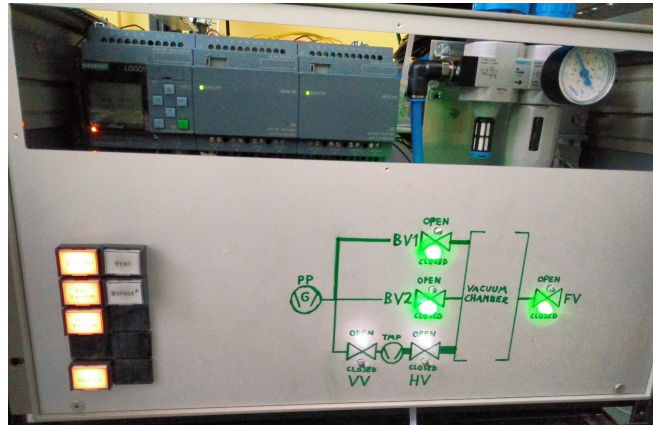
Figure 7.7.: Vacuum box to operate the instruments vacuum system via single buttons. The logic controller and the air pressure supply are visible in the inside. By pressing the buttons on the left, the system automatically and safely operates all pneumatic valves according to the mode desired. The valve positions are indicated by LEDs in a circuit diagram.
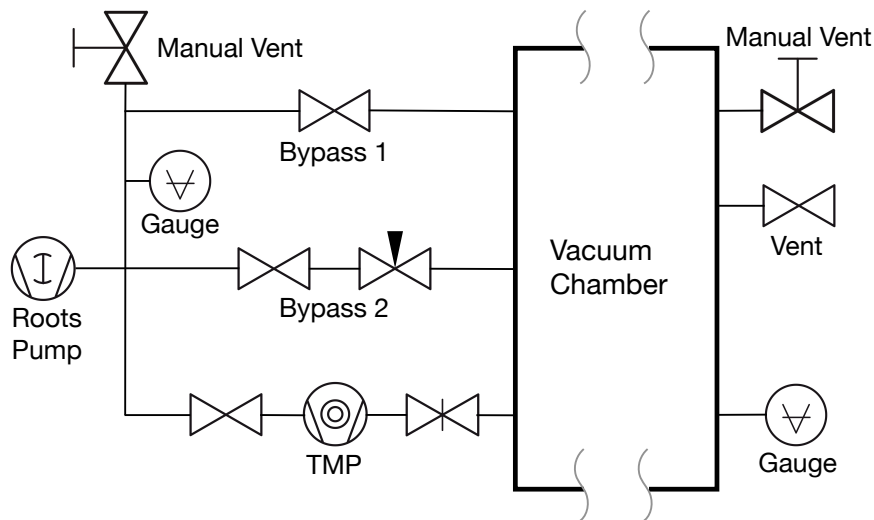

Figure 7.8.: Schematic view of the automated vacuum system. The vacuum chamber can be evacuated through *bypass 1* (regular), or *bypass 2* (slow pumping through adjustable needle valve). In "High Vacuum"-mode, the system pumps through the turbopump (TMP) as soon as possible, depending on the pressure measured by the gauges in the system and at the chamber.
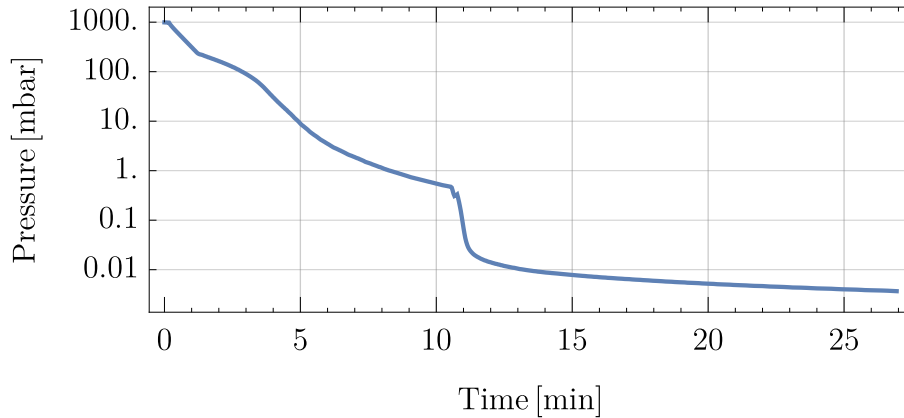
Figure 7.9.: Detail from a typical pressure curve from 24th of February 2017. The vacuum chamber was pumped automated via the "High Vacuum"-button on the vacuum automation box. The small fluctuations at around 10.5 min indicate the valves switching from pumping through the bypass to pumping with the turbopump.

While it took several days to reach a pressure within the vacuum chamber in the order of 10^{-5} mbar during the experimental time *3–14–358*, initial characterisations with an empty chamber exhibited 2.9×10^{-6} mbar within the first 18 hours of pumping, not having reached the final pressure yet (**Stangl** (2016)). This difference is due to the fact that not all components in use within the vacuum chamber could be ensured to be vacuum compatible at that time, and therefore outgassing. Knowing this, the components were replaced in subsequent experimental times.

7.2.2. Levelling of the Instrument

As the bound states of ultracold neutrons above a mirror are dependent on the Earth's gravitational acceleration g, the experiment surface should be aligned normal to the direction of gravity. The error (on g as well as the neutron eigenenergies) made by misalignment of an angle α scales with a factor $\cos \alpha$.

Within the qBOUNCE instrument, two steps ensure a levelled, stable measuring surface plate, upon which experiments can be set up:

- rough levelling of the vacuum chamber via spindle drives
- fine levelling of the surface plate of granite within the vacuum chamber via piezo-actuators.

The **spindle drives**[7] can be seen in figure 7.5. The gear ratio is 24:1, which results in an upstroke of 0.25 mm per full turn of the drive shaft. The vacuum

---

[7]Tr Z–25–R with a trapezoidal thread, ZIMM Maschinenelemente GmbH + Co KG, Millennium Pk. 3, A-6890 Lustenau.
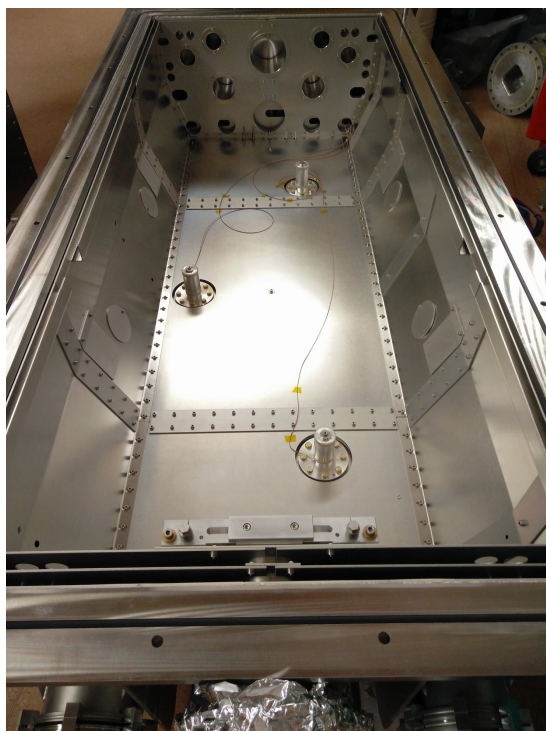
Figure 7.10.: Placed piezo-actuators for the levelling of the surface plate. The granite was inserted with dedicated spacer equipment mounted to the vacuum chamber, to ensure exact placement onto the actuators.

chamber sits on self-aligning nuts, which can compensate misalignment up to $\pm 3°$ of angle in any direction.

Within the vacuum chamber, the surface plate of granite is levelled on three **piezo-actuators**. Figure 7.10 shows the bottom half of the vacuum chamber without granite plate, with the actuators in place. Piezomechanik[8] elements of type PSt 150/20/80 VS25 offer a maximum stroke of 95 µm when operated from -30 through 150 V. The levelling of the granite plate is controlled via a control loop feedback mechanism consisting of the piezo-actuators and a tilt sensor[9] mounted on the granite. This PID-control was characterised and tested in **Mayr** (2016). Within the vacuum chamber, all three piezo elements are covered with a protection cover — a system that is free to move only in vertical direction, as piezo elements may not be stressed horizontally (see figure 7.5). This is merely a safety feature for processes like lowering the granite plate down onto the piezos. Data of an overnight measurement during the experimental time at the ILL in 2017 can be seen in figure 7.11. The root mean square of two independent normal distributions (here x and y axes of the tilt sensor) results in a Rayleigh distribution. The good match of the data and the estimated distribution shows

---

[8]Piezomechanik GmbH, Berg am Laim Str. 64, D-81673 Munich

[9]Model 755 by Applied Geomechanics, purchased through Tech-Sys Instruments: Tech-sys s.p.r.l, 64 Avenue de la Floride, B-1180 Bruxelles.
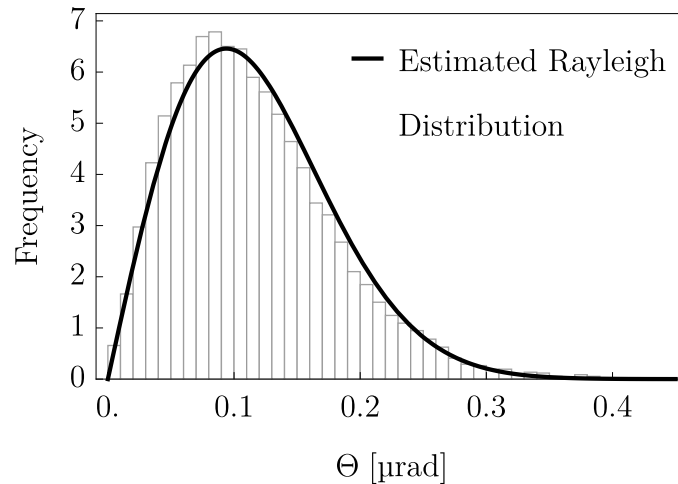
Figure 7.11.: Histogram of typical data output of the tilt sensor and an estimated Rayleigh distribution for the data. The root mean square Θ of the granite surface plate's tilt in x and y direction ($\Theta = \sqrt{1/2\left(\Delta x^2 + \Delta y^2\right)}$) peaks around $0.1\,\mu\mathrm{rad}$.

that systematics are minor and therefore no further investigations were made. Misalignment of the granite of $0.1\,\mu\mathrm{rad}$ shifts the energy ground state about $7 \times 10^{-27}\,\mathrm{eV}$ and is therefore negligible.

7.2.3. Granite Surface Plate

The granite surface plate within the vacuum chamber effectively is the heart of the qBounce instrument, as this is the basis and reference plane of all experiments taking place. Therefore, following criteria have been considered in the design:

- Large usable surface,
- versatile mounting possibilities for equipment,
- good stability and levelling,
- and sufficient flatness.

To fit properly into the vacuum chamber, the basic rectangular block shape of the granite is chamfered along the lower lengthwise edges. Its dimensions are $1900 \times 700 \times 220\,\mathrm{mm}$ with a weight of approximately $840\,\mathrm{kg}$, and the surface's flatness is below $2\,\mu\mathrm{m}$. Although the manufacturer[10] guarantees this flatness for given supporting points (in our case the position of the three piezo-actuators), FEM simulations have been carried out to minimise bending of and stress within the granite (see figure 7.12a for a simulation with the final design) by choosing the supporting points accordingly.
To save space, blind holes in the granite let the piezo elements enter the granite

---

[10]Johann Fischer Aschaffenburg Präzisionswerk GmbH & Co. KG, Ruhlandstrasse 72–78, D-63741 Aschaffenburg

(a)　　　　　　　　　　　　　　　　　　(b)
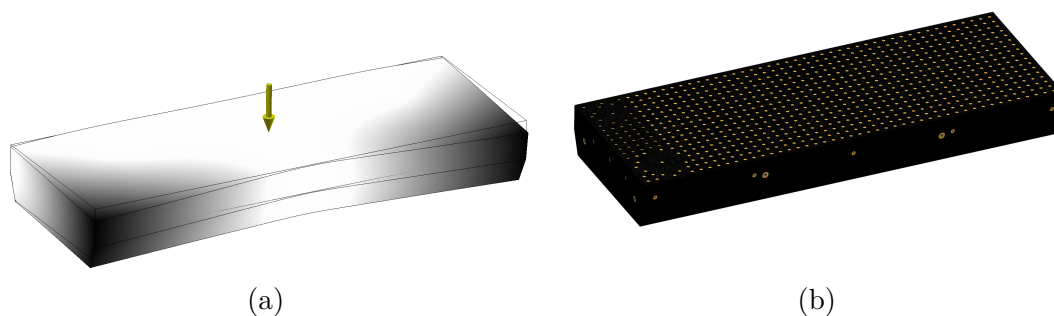
Figure 7.12.: (a) A simplified FEM simulation of the granite surface plate without threaded inserts with the final shape design, supported on three piezo elements underneath. Even without further lap procedures, an initially perfectly flat surface bends only 1.8 µm under gravity at two of the corners. (b) A model of the final surface plate with all threaded inserts on and around the granite.

thus far so the granite can be positioned as low as possible within the vacuum chamber (see figure 7.5). Within the blind holes, brass plates with three threaded holes are placed. Another brass plate is then fixed to the first one, serving as replaceable contact plate to the piezo system. In case the rounded contact part of the piezo system leaves pressure marks in the contact brass plate over time (possibly at unwanted positions), the plate can be replaced.

All over the granite's surface, 773 threaded M6 inserts are placed, mostly for mounting purposes of experiment components (figure 7.12b). At the rear end, two round geometries for placing tilt sensors are provided where vacuum pipes connected to inverse feedthroughs can be mounted, for tilt sensors that have to be operated at atmospheric pressure. All around the surface plate, additional threaded inserts of various diameter are placed for attaching hoisting gear or serving other purposes in the future.

Two identical granite surface plates are used, where the second one not only serving as a spare part, but is used in parallel to the one within the vacuum chamber for testing and preparing all kinds of setups relevant for the experiment.

7.2.4. Magnetic Shield

Due to the non-zero magnetic moment of the neutron, external magnetic fields have to be shielded in order to avoid systematic errors in the measured transition frequencies of the UCNs. Different to previous *q*BOUNCE setups, the magnetic shielding is now fully integrated into the instrument. A two layer MuMetal shield of three millimetre each and 10 millimetre space in between is imbedded between the inside of the vacuum chamber and the granite surface plate, mounted on the vacuum chamber's threaded bolts (see figure 7.5). Two major advantages arise from this setup. Firstly, magnetic shielding is required in *q*BOUNCE experiments

in any case, and placing the shield within the vacuum chamber allows for manufacturing the chamber out of slightly magnetic but cheaper V2A stainless steel, instead of the less magnetic V4A version. Secondly, the shield does not have to be assembled and dissembled every time the vacuum chamber is closed and opened, as per design the two MuMetal layers from top and bottom halves of the vacuum chamber join and overlap in the process of closing the chamber (see figure 7.5).

The design, based on our initial suggestions and subject to many boundary conditions, was developed under active communication between us and the manufacturing company Magnetic Shields[11]. At the position of the feedthroughs in the vacuum chamber, as well as at the opening for the neutron beam guide, the magnetic shield was equipped either with branch tubes (tubes of MuMetal connected with the main layers that are going into the actual feedthrough) or movable cover plates, to cover the holes in the main layers of the shield. By restricting the holes for the feedthroughs to the minimum sizes of for instance connectors of cables, some of the holes did not have to be covered at all, as the penetration of magnetic fields are then very short ranged. For the feedthrough of the neutron beam guide entering through the bellow, a height adjustable branch tube was designed.

In figure 7.10, the lower half of the shield can be seen.

Shielding Factor

Taking the magnetic moment of the neutron from table 2.1 and inserting the nuclear magneton μ_{N},[12] yields the energy shift of a neutron in a magnetic field:

$$\Delta \vec{E} = -\vec{\mu}_n \, \Delta \vec{B} \ , \tag{7.1}$$

$$\left| \Delta \vec{E} \right| \approx 60.3 \, \frac{\mathrm{neV}}{\mathrm{T}} \ . \tag{7.2}$$

For an exemplary vertical component of the Earth's magnetic field of $45\,\mathrm{\mu T}$, this translates to a shift of around $2.7\,\mathrm{peV}$ in comparison to a non existing field. Remembering the bound states of UCNs above a mirror (figure 3.1), it becomes clear that residual field gradients (only energy differences matter in GRS) within an experiment should be dampened below the pico-electronvolt range — the energy of the first eigenstates. A shielding factor of around 100 brings natural magnetic fields (and therefore maximum possible field gradients) down to the percent level in terms of UCN energies above a mirror, and gradients along the critical experimental area can then be expected to be even lower. Therefore, a shielding factor of 90–110 was aimed for in the planning of the shield.

Figure 7.13 shows measurements in the course of the final inspection of the magnetic shielding, fitted into the qBounce vacuum chamber. Due to technical restrictions at the time, the measurements could not be performed atop the UCN

---

[11]Magnetic Shields Ltd, Headcorn Road, Staplehurst, Tonbridge, Kent, TN12 0DS, UK

[12]$\mu_{\mathrm{N}} = e\hbar/\left(2m_{\mathrm{p}}\right) = 5.050783699(31) \times 10^{-27}$ J/T, 2014 CODATA recommended values
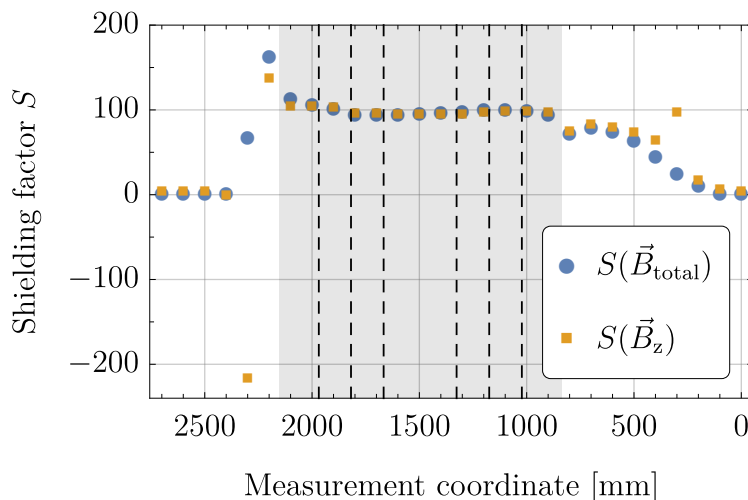
Figure 7.13.: The magnetic shielding factor of the *q*BOUNCE vacuum chamber shield is shown, deduced from measurements. The shaded area represents the area initially defined as critical experimental area, whereas the regions between dashed horizontal lines correspond to the positions of the five Ramsey regions in the experimental time *3–14–358*. The UCN flight direction goes from left to right. Statistical error bars are not visible due to the plot markers.

platform at PF2 of the ILL, where the experiment ultimately takes place. The measurements were done several meters away from the platform, but still in the reactor hall on level D.

The shielding factor S is plotted for the total magnetic field in z-direction $\vec{B}_z$ as well as for the total field $\vec{B}_{total} = (\vec{B}_x^2 + \vec{B}_y^2 + \vec{B}_z^2)^{1/2}$, as perfect alignment of the axes of the magnetometer[13] is difficult. Nevertheless, it can be seen that the vertical field component contributes predominantly to the total shielding factor. The magnetic field was first measured without the vacuum chamber and then measured again with the vacuum chamber and it's imbedded magnetic shield present. Care was taken to achieve high reproducibility of the measurement positions (increments of $10\,cm$ and roughly at height of the neutron mirrors' surface) by setting up a test frame along which the magnetometer was moved.

It is obvious that the shielding factor changes drastically outside the shaded area, where boundary effects due to the geometry of the shield or the branch tubes manifest. With a simple interpolation between the data points (under the assumption of sufficiently smooth behaviour of the shield between the data points measured), the averaged shielding factor within the shaded area yields $S(\vec{B}_{total}) \approx 98.6$, whereas the shielding factor along the setup of neutron mirrors results in $S(\vec{B}_{total}) \approx 96.9$.

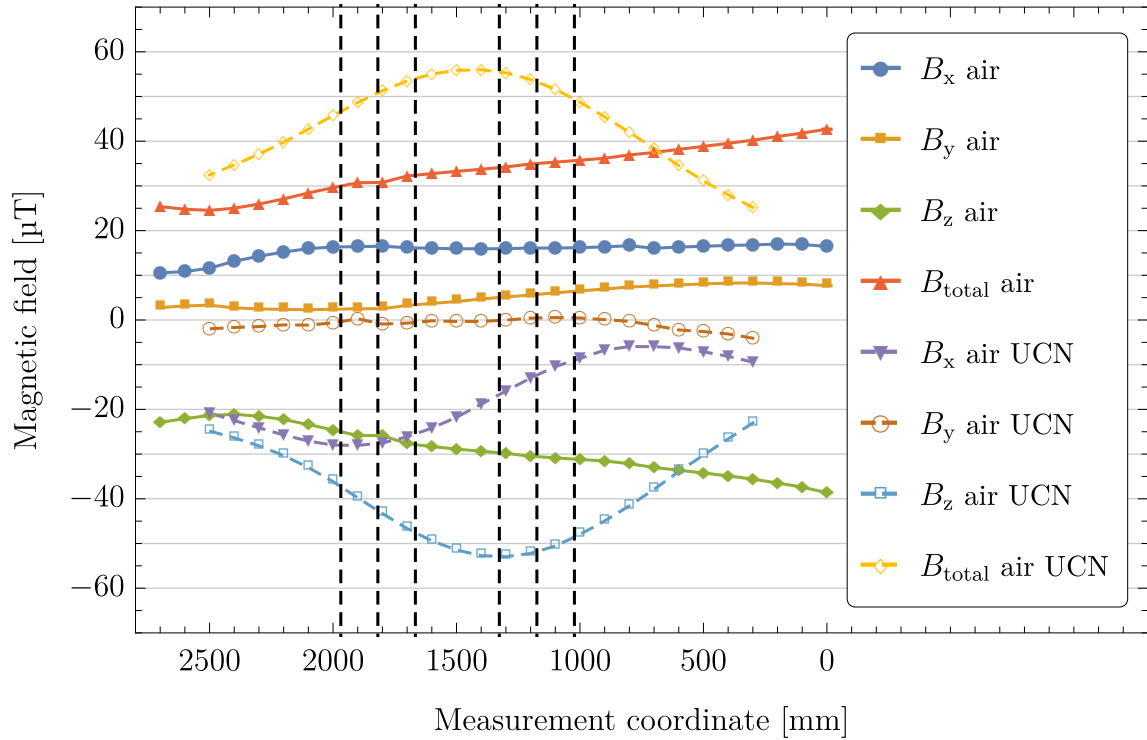[13]Bartington Mag-03MSL100, used for all measurements within this section

75

Figure 7.14.: Air readings (without vacuum chamber and magnetic shield present) of the magnetic field measured next to the UCN platform at level D (solid lines, "air"), and at the vacuum chambers final position on the UCN platform (dashed lines, "air UCN"). Every measurement point is an average over $5\,\text{s}$ with millisecond intervals, and statistical error bars are not visible.

Residual Field Homogeneity

Figure 7.14 shows air readings of the magnetic field at the PF2. No vacuum chamber and thus no magnetic shield was present during these measurements, but the measurement positions were adjusted to be roughly along the neutron flight path in the experiment. Comparison of the measurements next to (solid lines) and on the UCN platform (dashed lines), shows more oscillations in the field on the platform. This presumably comes from the steel scaffold construction of the platform (see figure 7.1b). Movements of cranes (on the same floor as well as one storey below) or vehicles would produce temporary magnetic effects. Their influence cannot be ruled out, but are unlikely to produce the magnetic fields measured. No neighbouring experiments with high magnetic fields were present at the time and can be ruled out. Overall though, the field strengths of both measurements are in the same range, with larger gradients on the platform.

For the position next to the platform, measurements with vacuum chamber and magnetic shield present, yielded maximum field gradients of around 47, 36,
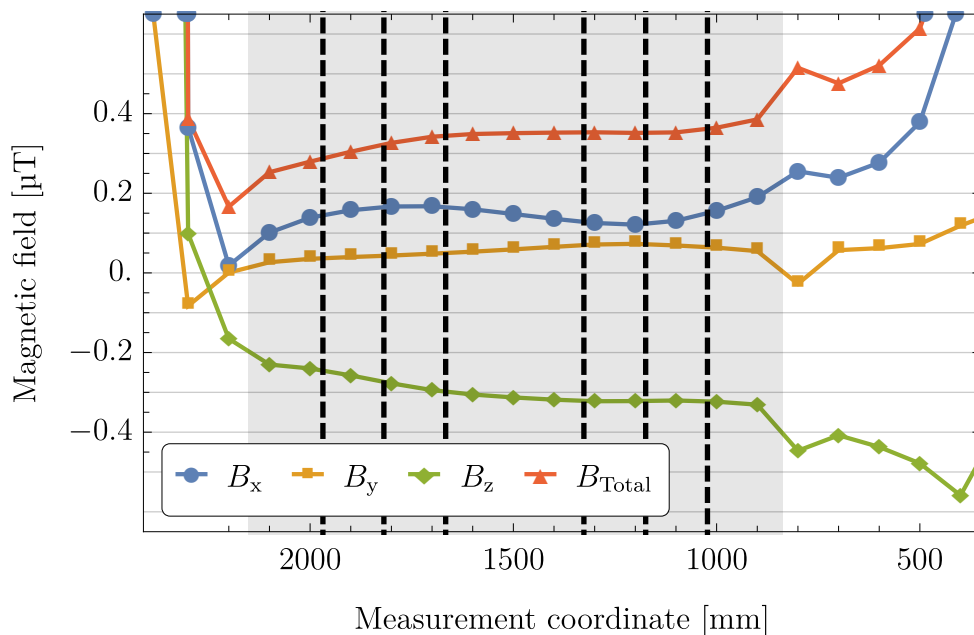
Figure 7.15.: Measured residual magnetic fields within the vacuum chamber, placed next to the UCN platform at PF2. The shaded area again represents the area initially defined as experimental area. Inside this area, boundary effects of the front ends and therefore residual fields are small. The regions between dashed horizontal lines correspond to the positions of the five Ramsey regions in the experimental time *3–14–358*. The UCN flight direction goes from left to right. Statistical error bars are not visible due to the plot markers.

78 and $74\,\mathrm{nT}/0.946\,\mathrm{m}$, respectively, for x, y, z, and total residual field gradients between the positions of the beginning of region I and end of region V (very left and very right dashed vertical lines in figure 7.14). The residual fields are shown in figure 7.15. For the UCN platform, without other sources of magnetic fields, the gradients will be slightly higher, according to the higher initial field gradients in the air readings.

In summary, the implemented double layer magnetic shield is embedded into the new vacuum chamber and fulfils the aimed specifications with a stable shielding factor of around 100 all over the critical experimental area.

7.2.5. Glass Neutron Guides

For the first time, *q*BOUNCE uses neutron beam guides made from glass, produced by Movatec[14]. The guides are coated with a $500\,\mathrm{nm}$ thick non-magnetic nickel and molybdenum (85/15) composition on the inside to ensure high reflectivity

---

[14]Movatec GmbH, Erfurter Straße 23, D-85386 Eching

for ultracold neutrons. The usage of glass has the advantage of resulting in very smooth surfaces, highly suitable for being coated. The drawback, however, is that glass is naturally more fragile than the stainless steel guides usually used so far. The 5 mm wall thickness of the guides with 90 mm outer diameter make them quite sturdy nevertheless.

Figure 7.16 shows the beamline set up at the UCN platform of the PF2. UCNs emerge from the turbine and are guided through the biological shielding. There, also a thin aluminium foil is installed, so that the beam guides coming from the turbine and the beamline set up by qBOUNCE can be evacuated individually. A pneumatic rotating UCN shutter (2) follows. Up to this point, conventional electropolished steel guides (with an outer diameter of 81 mm) have been in use. An adapter flange with outlets for pumping the beam guides (3) connects the steel pipe after the shutter to the first glass guide of 450 mm length. Another flange (4) connects the second glass guide of length 750 mm and has connectors for pumping or measuring air pressure as well as a connector pointing downwards. This allows for a neutron detector to be placed underneath to serve as a beam monitor. The second glass neutron guide is then immediately fed through a flange mounted on the vacuum chamber's flexible bellow (5). This flange as well as all beam guide connections before, seal around the outside of the neutron guides.

Within the vacuum chamber, the neutron guide's end is closed with a thin (100 µm) aluminium foil, which has a low neutron absorption. As can be seen in table 2.2, however, the Fermi pseudopotential of aluminium leads to a cutoff of the transmitted neutrons below ≈ 3.2 m/s. In order to avoid damages to this thin foil, the air pressure on the side of the vacuum chamber should always be higher or equal to the pressure in the neutron guide. Like this, the neutron guide can stay evacuated even if the vacuum chamber is vented.

The foil is part of a newly designed aluminium end cap and is placed upon an O-ring seal, pressed down with a thin counter piece of aluminium. This allows for very close positioning of any experimental equipment to the outlet foil. By keeping the end cap thin in general (< 40 mm), it is in principle possible to position the last neutron beam guide in such a way, that the end cap ends 10 mm before the granite surface plate begins. However, for reasons of precaution, a height adjustable holder for the glass neutron guide was placed within the vacuum chamber, so that the own weight of the glass tube together with the additional weight of the end cap will not lead to unwanted stress within the glass. Moreover, the new end cap is also coated with NiMo on the inside to reduce unwanted background of neutrons penetrating through the aluminium. A picture of the end cap as well as the holder can be seen in figure 7.17.
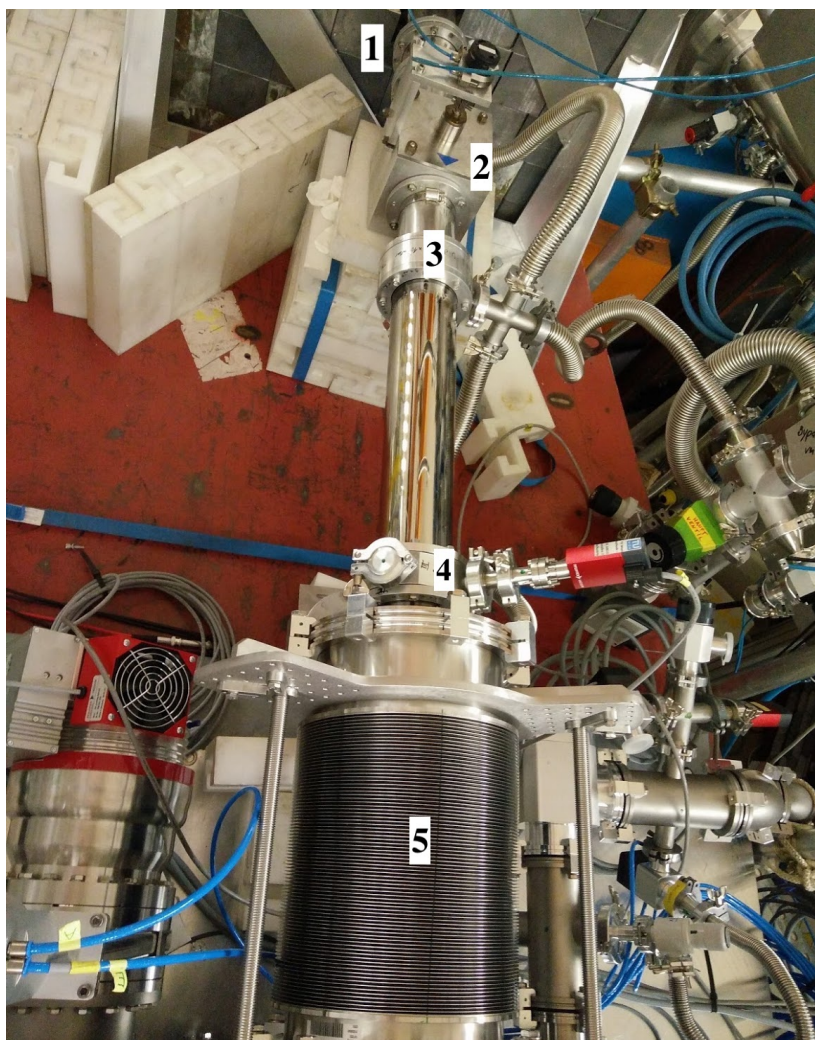
Figure 7.16.: Beamline setup guiding neutrons from the PF2 turbine (top, behind the visible biological lead shielding, 1) to the *q*BOUNCE vacuum chamber (bellow flange visible at the bottom of the image, 5). Neutrons go through a rotating shutter (2), and glass neutron guides connected via flanges (3 and 4) until they enter the vacuum chamber. Parts of the vacuum system like turbomolecular pump on the bottom left and bypass/pumping pipes on the right, are visible.
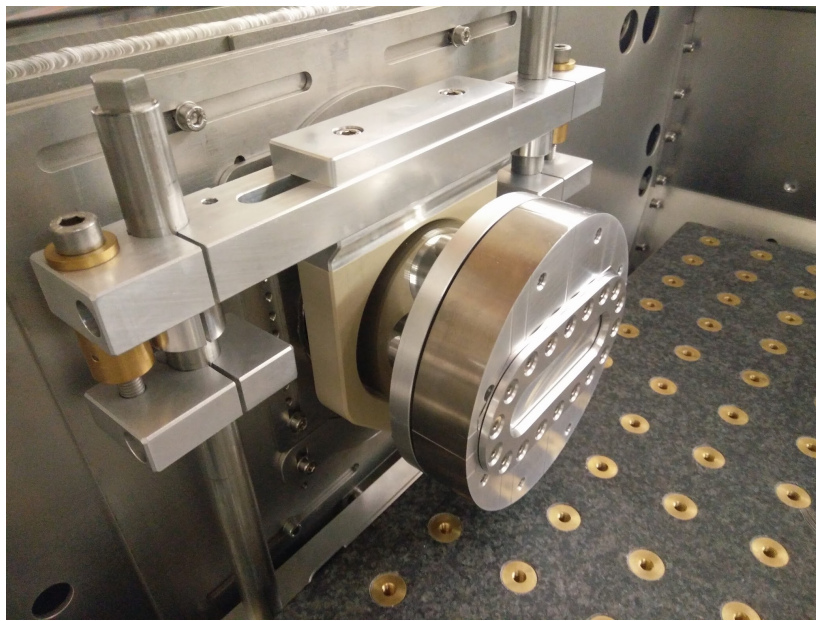
Figure 7.17.: Beam guide end cap and height adjustable beam guide holder within the vacuum chamber. The height adjustment of the MuMetal branch tube for the beam guide is visible in the back.

8. Experimental Ramsey-setup within *q*Bounce

This section focuses on the experimental components of the Ramsey-type *q*BOUNCE setup. Section 8.1 describes all components along the neutron flight path essential for Ramsey-type GRS. Section 8.2 covers auxiliary components, that are used to monitor the Ramsey-setup.

The control of most experimental components is carried out via LabVIEW[1]. For the new setup, several changes have been implemented. The control is now based on a LabVIEW project structure and data acquisition is implemented using the syslog protocol (**Herzinger** (2014)). Also, an automation via scripts allows for carrying out and monitoring experiments and a global visualisation displays important parameters of all devices in use. All control hardware was mounted into two 19-inch racks, together with two identical servers responsible for the software control of the experiment. This way, besides the wanted redundancy in case of failure, the servers can be used in parallel for controlling the experiment and for tests or software development.

8.1. Ramsey GRS Core Components

Figure 8.1 shows a rendered image of the *q*BOUNCE Ramsey-setup. Ultracold neutrons enter the setup from the left through a velocity selector system, bounce along a five-part neutron mirror setup, and are detected right after. In the following, the components of the setup shall be described in detail.

8.1.1. Velocity Selector System

A system of velocity selecting blades is used to restrict incoming ultracold neutron velocities in the experiment in flight direction (see figure 8.1). Thus, it directly defines the flight times of the neutrons through the regions of a GRS-setup. Figure 8.2 illustrates the concept. Vertical blades form a slit aperture and restrict the allowed flight parabolas for neutrons to enter the mirror-absorber system.

Neglecting the slit height l between mirror and absorber and presuming a purely classical flight path, one finds an expression for the allowed v_x:

$$X\sqrt{\frac{g}{2h_{\mathrm{l}}}} \leq v_x \leq X\sqrt{\frac{g}{2h_{\mathrm{u}}}} \,. \tag{8.1}$$

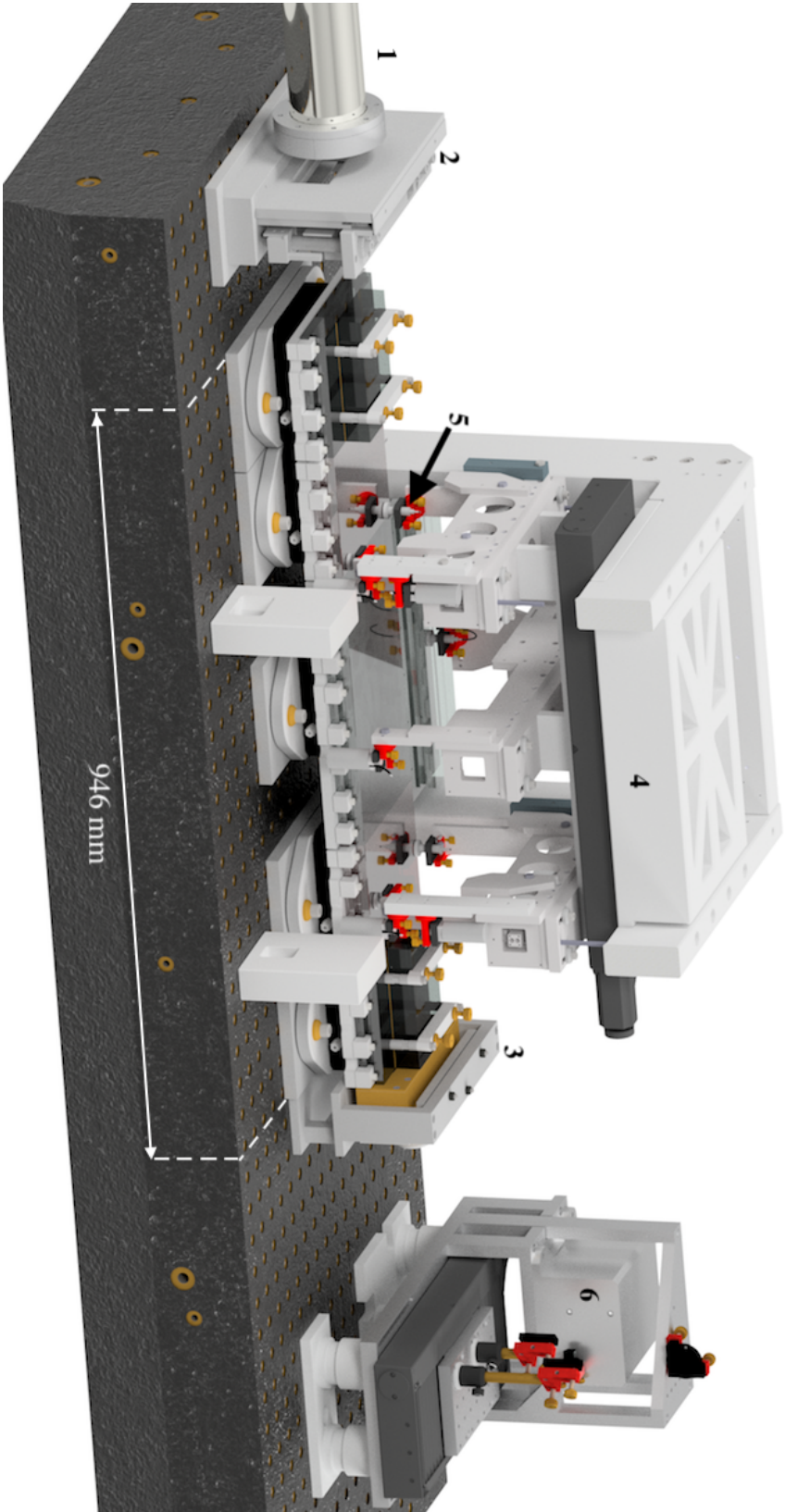[1] National Instruments Ges.m.b.H., Heinrichsgasse 4, A-1010 Wien

Figure 8.1.: A rendered model of the experimental setup is shown. A neutron beam tube (1) guides UCNs to the slit aperture (2) from the left. A five region neutron mirror setup with a detector at the end follows. The mirrors are displayed slightly darker than they are for better visibility. Around the neutron mirrors (with a cut through the sensor gantry, 4, for better visibility) and behind the detector (3, brass colour), setups for monitoring experimental parameters through capacitive sensors (5) and a laser interferometer (6) are placed. The granite plate has a length of 190 cm and a width of 70cm.
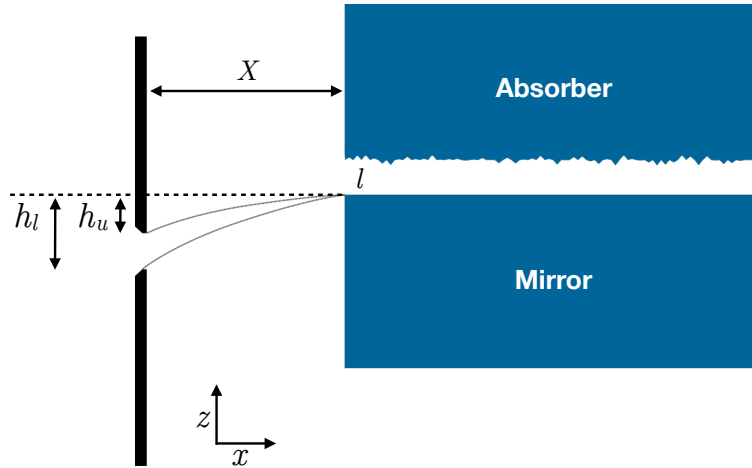
Figure 8.2.: Schematic illustration (not to scale) of the velocity selecting blades system. The blades are shown in black on the left-hand side, at distance X from the mirror-absorber system. Neglecting the slitheight l between mirror and absorber, the neutrons' trajectories for maximal and minimal velocity v_x are shown. The heights of lower (h_l) and upper (h_u) blades refer to the mirror surface.

Thus, the positions of the blades h_l and h_u, control the lowest and highest allowed neutron velocity, respectively.

Until the experimental realisation of the Quantum Bouncing Ball in 2014 (see section 3.2), the velocity selector system was embedded into a part of the former vacuum chamber, but not mounted directly on the measurement plate due to shortage of space. This leads to problems, the main ones being that the system is poorly accessible and that the height reference to the measurement granite is difficult. Therefore, the existing system for velocity selection was adapted for the new Ramsey setup, improvements were made and the new system was characterised (**Rath** (2016)).

A rendered image of the collimating blades system is shown in figure 8.3. The main section of the system are two horizontal blades in the middle, made from boron steel, which operate as a slit aperture. Boron has a high neutron absorption cross section and steel can be lapped to achieve high flatness and well defined upper and lower edges, respectively[2]. The blades are connected to fine threaded rods through aluminium blocks. Due to this direct connection to the blades, these blocks serve as measurement blocks. The height of the blades is adjusted with the fine threaded rods. In a readily adjusted setup on the measurement granite, usually there is no space to measure the positions of the blades directly. Therefore, the blades' position can be measured with a depth gauge from top, directly to measurement blocks (and a brass extension from the block for the

---

[2]In this case the slit-facing surfaces have a mean roughness index of 0.1 µm, and a flatness of 0.01 mm. This means that the surface must lie between two hypothetical parallel planes with a distance of 0.01 mm.
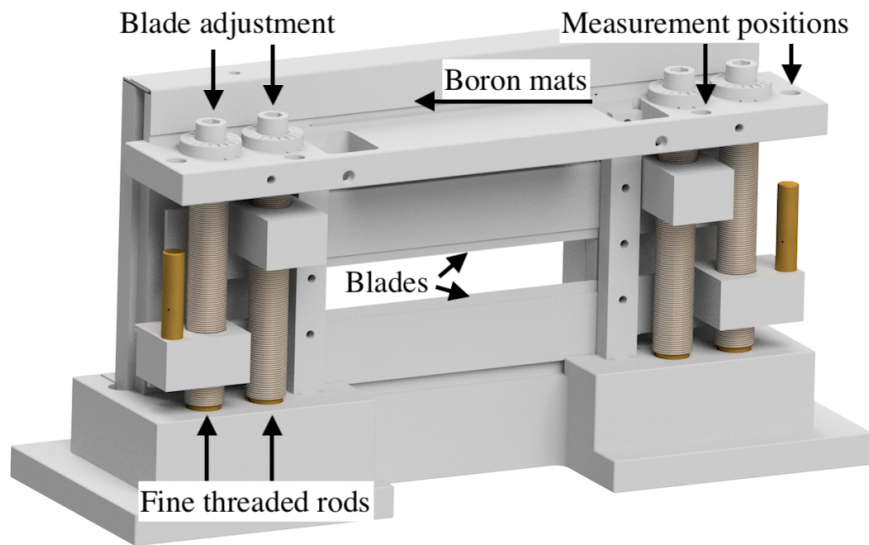
Figure 8.3.: Rendered image of the rebuilt velocity selecting blades system. Fine threaded rods are connected to the blades of the slit aperture via measurement blocks, and tune their height. The measurement blocks can be accessed from above with a depth gauge. On the backside, boron mats or other neutron absorbing materials can be mounted via an aluminium sheet. This is to prevent UCNs to penetrate the system, which is mainly built of aluminium, outside the aperture.

lower blade, respectively). The fine threaded rods are also operated from above, tune the height of the blades, and therefore also the incoming neutron velocity spectrum. The neutrons exiting the beam guide towards the experiment are not restricted in the y-direction (perpendicular to the flight direction of the neutrons).

Measurements of the incoming neutron velocity distribution within *q*BOUNCE follow in section 9.2.

8.1.2. Neutron Mirror Setup

The neutron mirror setups for *q*BOUNCE are shown in figure 8.4. Two different setups are used: A propagation region, where ultracold neutrons freely bounce along a flat mirror surface, and a mirror-absorber region, with which the lowest energy states of neutrons can be selected. Based on previous designs (**Jenke et al.** (2011); **Cronenberg** (2016); **Thalhammer** (2019)), some minor novelties were incorporated in the design of the new Ramsey regions. The two setups are identical besides the absorber placement and shall be described in the following, from bottom to top.

Coarse Levelling Basis

The coarse levelling ultimately allows the neutron mirrors to be aligned without steps via the employment of nanopositioning tables, which have a restricted range.
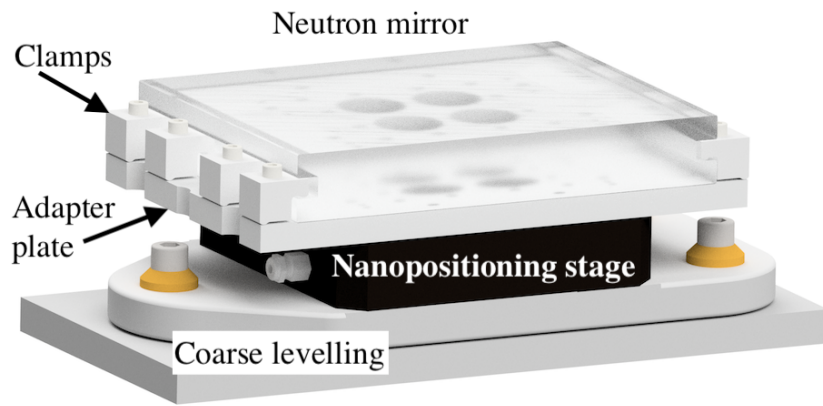
(a)
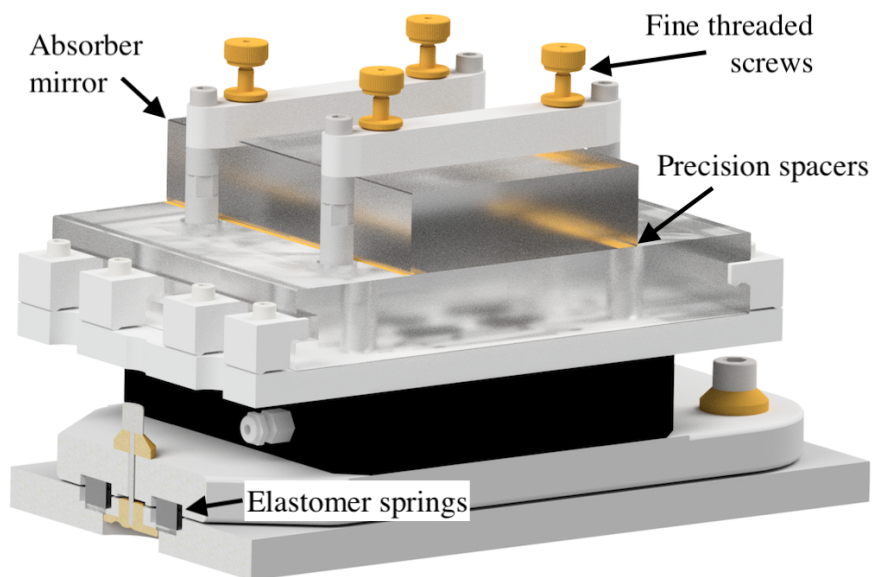
(b)

Figure 8.4.: Rendered images of neutron mirror setups used within *q*BOUNCE. Usually, the top of the mirror is coated with aluminium, and therefore not transparent. (a) Propagation region, (b) mirror-absorber setup with a cut through the coarse levelling plates on the left.

The two aluminium plates are separated through elastomer springs[3], which are compressed via three fine threaded screws. Thereby, height adjustments in the millimetre range down to a precision of less than 10 micrometres, as well as tip and tilt regulation better than $100\,\mu$rad (depending on the dimensions of the mirror placed on the region) are feasible.

Nanopositioning Stage and Mirror Mounting

Atop the coarse levelling basis, a nanopositioning stage is mounted. The Physik Instrumente[4] stages have height ranges from 50–200 μm and $\pm 500\,\mu$rad for tip and tilt. The stages are not only used for aligning all neutron mirrors with barely any steps in between, but their controller units have analogue inputs where signals from a frequency generator can be fed in. These input signals can be employed for generating oscillations of the neutron mirror. Control algorithms from previous realisations have been rewritten and automations programmed that can deal with static or oscillating nanopositioning stages (**Neuhuber** (2017)).

In between the actual neutron mirrors and the nanopositioning tables, adapter plates with clamps to hold the mirrors in place are implemented. While the clamp mechanism was upgraded slightly to reduce the chance of damages to the mirror, the adapter plates were now also kept shorter in flight direction of the neutrons than the length of the mirrors. Hence, contact between two subsequent regions can be ruled out as long as the mirrors themselves are not touching. This makes the alignment of the five regions easier.

Neutron Mirrors

The neutron mirrors are manufactured by POG[5], consist of optical crown glass and have an optically reflecting aluminium coating[6] on top. The coating allows for supervision of the mirrors via lasers and capacitive sensors.

The manufacturer specifies the contour accuracy of the mirror surface as $3/0.5(0.2)$ in every $\varnothing 60\,$mm, the surface quality as $5/3 \times 0.16$ in every $\varnothing 60\,$mm and the parallelism as $5''$ ($\approx 0.0014°$).

According to DIN 3140 (now DIN ISO 10110) for optical components, the specification number 3 describes surface form tolerances and translates in this case to the following:

$$A(B/C) = 0.5(0.2) = \frac{\lambda}{4}\left(\frac{\lambda}{10}\right) , \qquad (8.2)$$

---

[3]Elastomer compression spring 70 Shore A by Meusburger Georg GmbH & Co KG, Kesselstr. 42, A-6960 Wolfurt.

[4]Models P-518, P-528 and P-558.TCD, Physik Instrumente (PI) GmbH & Co. KG, Auf der Roemerstrasse 1, D-76228 Karlsruhe.

[5]POG Präzisionsoptik Gera GmbH, Gewerbepark Keplerstraße 35, D-07549 Gera

[6]Al wire used: 99.98%, thickness not verified by the manufacturer, protective coating of $(180 \pm 15)\,$nm SiO_2 from 99.99% granulate.

Table 8.1.: Maximum contour errors A/B to be expected for different neutron mirror lengths/widths due to the manufacturing process.

Mirror length [mm]	152	200	340
Error (A/B) [nm]	401/160	528/211	897/359

with reference wavelength λ, the maximum spherical sag error from the test plate A (in number of Newton fringes), the maximum irregularity B (deviation from a spherical shape, in number of fringes), and rotational symmetry irregularities C. With $\lambda = 633\,\text{nm}$ as used by the manufacturer, this yields $A = 158.25\,\text{nm}$ and $B = 63.3\,\text{nm}$ for every $60\,\text{mm}$. For the neutron mirrors used within qBOUNCE, table 8.1 summarises the resulting errors to be expected for the contour accuracy. The surface quality specification 5, given as $3{\times}0.16$ in every $\varnothing 60\,\text{mm}$ indicates a maximum of three surface imperfections of size $0.16\,\text{mm}$ within any diameter of $60\,\text{mm}$.

While previous experiments within qBOUNCE have been considerably smaller in size and deviations of the neutron mirrors' surfaces from ideal planes were therefore smaller, these specifications posed a problem to the alignment routine of the neutron mirrors in the initial operation of the Ramsey experiment (see section 8.2.2).

Absorber System, Region I & V

The absorbers above the neutron mirrors in regions I and V are held in place via four fine threaded screws that press the absorber down onto precision spacers made of brass. The gauges are (depending on the amount of pressure executed via the fine threaded screws) defining the slit width between mirror and absorber. The absorber mirrors for preparation and analysis in resonance experiments are produced with the same specifications as all other mirrors, but are not coated. In addition, one of their surfaces is roughened. This is done by the glassblowing workshop of the University of Heidelberg[7] by the use of corundum abrasive. Details and an analysis of previously manufactured absorbers can be found in **Wautischer** (2015) and the absorbers produced in the course of this thesis are analysed in **Schmidt** (2017). The absorbers were roughened with corundum abrasive F600 (mean grain size of $(9.3 \pm 1.0)\,\text{µm}$ as per FEPA standards), featuring similar roughness parameters than the absorber used in **Cronenberg** (2016).

Systematic neutron measurements of the mirror-absorber systems with regions I and V are presented in section 9.3.

---

[7]Universität Heidelberg, Grabengasse 1, D-69117 Heidelberg

8.1.3. Neutron Detection

Two different neutron detectors play a roll in *q*BOUNCE experiments. The main detector for Gravity Resonance Spectroscopy is a **neutron counter tube** as shown in brass colour behind the last mirror of the Ramsey setup in figure 8.1. The proportional neutron counter has an anode wire within a cylindrical volume filled with $ArCO_2$ (90:10), where CO_2 acts as quenching gas. The decay products from neutron capture reactions[8] enter the detector volume through the ^{10}B coated entrance foil of $AlMg_3$. In comparison to the decay products, the kinetic energy of the UCNs is negligible, and the decay products will emerge in opposite directions. Therefore, at all times, at most only one decay product (helium nucleus or lithium ion with opposite momentum) can reach the detector per incoming neutron. There, ionisation of the Ar gas[9] and the avalanche phenomenon produce a charge measurable with the high voltage electrode. The measured charge is still proportional to the initial ionisation and so the detection is sensitive to the energy of the ionising particle. The detector in use, developed by Martin Thalhammer, is an advanced version of the one developed in **Thalhammer** (2013) and presented in **Jenke et al.** (2013), and its background rate measured at the Atominstitut in Vienna is (0.41 ± 0.04) mHz (**Heistracher** (2015)). Of course, this background value is to change when the detector is put into operation at the ILL, already because neutron and radiation background will be higher. A characterisation of the detector in its final position in the experiment follows in section 9.5.
The detector system was integrated into the LabVIEW visualisation in **Huber** (2017).

In order to determine the population of the eigenstates of UCNs above the mirror after region I and region V, **CR-39 neutron detectors** with a spatial resolution are used. The detectors are made of CR-39 plastic[10] and just as the counter tube use ^{10}B as neutron converter. With a thin layer of copper in between, a layer of around $0.2\,\mu m$ of boron is coated onto the plastic. CR-39 is a well known track detector for particles of a wide range of energy.
The decay particles from the neutron capture reaction in the boron layer are well suited for damaging the structure of the polymer, and after an etching process the particles' tracks can be visualised with an optical microscope with a resolution of 1–$2\,\mu m$. The spatial resolution detectors are for example summarised in **Jenke et al.** (2013) or **Filter** (2018).

To determine the incoming neutron flux into the experiment (and monitor possible changes due to reactor power or UCN production), a ^3He **monitor detector** provided by the ILL is used. The detector is mounted at connection flanges of neutron beam guides, where some clearance allows neutrons to exit the

---

[8] $(n + {}^{10}B) \rightarrow \{(\alpha + {}^{7}Li^{*} \rightarrow \alpha + {}^{7}Li^{3+} + \gamma)_{94\%}, (\alpha + {}^{7}Li^{3+})_{6\%}\}$

[9] CO_2 is used as quenching gas, to absorb high energy photons produced in the collisions and therefore suppress further/unwanted ionisation elsewhere in the detector volume.

[10] Plastic strips are very light, therefore two tiny dots of glue on either side are sufficient to mount the detector on a holder and can be dissolved with acetone after the measurement.

neutron guide and fall into the detector (compare with section 7.2.5).

8.2. Auxiliary Components

This section treats the most important systematic issues for the experiment presented, as the auxiliary components have to major tasks:

- monitoring of the neutron mirror oscillations, and
- monitoring of tilt and steps along the neutron mirrors.

As a novelty for *q*BOUNCE experiments, the simultaneous mechanical oscillation of two neutron mirrors is investigated. The monitoring of the movement of the oscillating neutron mirrors is crucial for the precision with which the transition frequencies can be determined. Steps in either direction between two neutron mirrors lead to losses through reflection or to unintentionally induced transitions.

Two different systems are used: Neutron mirror oscillations are monitored with laser interferometers, which allow precise measurements of the oscillation frequency and amplitude, as well as the phase between the two oscillating regions. Tilts of, or steps between subsequent neutron mirrors, are measured via capacitive sensors. The optical elements guiding the laser beams onto the mirror surfaces, as well as the capacitive sensors, are mounted on a linear stage above the neutron mirror setup. Therefore they can be moved along the neutron mirrors. The linear stage is attached to the sensor gantry shown in figure 8.1 (4). Both monitoring processes, for mirror oscillations and for relative positioning of the mirrors, shall be described in the following two sections.

8.2.1. Monitoring of Neutron Mirror Oscillations

For a Ramsey setup within *q*BOUNCE, the parameters frequency, amplitude, and phase of the oscillations of the neutron mirrors have to be known. Following steps and measurements have been performed to ensure the control over these parameters up to the precision needed at the moment.

The main interferometer used to monitor oscillations of the neutron mirrors is placed at the very right on the granite in figure 8.1 (6). The construction it is built into is called SIOS stage[11] and features another linear table shown in black — perpendicular to the other linear table attached to the sensor gantry. Through optical elements mounted on the linear stages[12], two laser beams of the interferometer can scan the neutron mirrors along the x and y axes. The third laser beam is deflected down onto the neutron mirrors as well, but the optics (not shown in figure 8.1) are not movable and therefore only a single position on

---

[11]The name is due to the SIOS laser interferometer mounted on it. SIOS Meßtechnik GmbH, Am Vogelherd 46, D-98693 Ilmenau.

[12]HPS-170 with 300 and 150 mm range, respectively. Now PI miCos GmbH, Freiburger Straße 30, D-79427 Eschbach.

the mirror setup can be measured. This beam serves as a reference beam for the moving ones.

Simultaneous Oscillations of Two Neutron Mirrors

The mechanical oscillation of two neutron mirrors potentially exhibits two systematic effects of a Ramsey-type setup within *q*BOUNCE, namely the stability of their phase and of their amplitude, respectively. The effects can arise in different forms. While an error due to a possible detuning (in phase, amplitude, or both) between two separate regions is evident, also the oscillations within a single neutron mirror have to be analysed properly.

Oscillations of a single neutron mirror have been realised before (**Jenke et al.** (2011); **Cronenberg** (2016)). In first tests with two simultaneously oscillating neutron mirrors fixed on one granite plate (**Heiß** (2017)), significant problems in their observation were encountered. Phase and amplitude measurements yielded inconclusive results. Although the granite plate weighs around 840 kg, parasitic oscillations were disturbing either the neutron mirror setups themselves, and/or the SIOS stage construction and the optical elements involved to guide the laser beams from the interferometer to the neutron mirrors. With a temporarily implemented external (extensively mechanically decoupled) second laser interferometer, the oscillations could be adjusted to be in phase, with the same oscillation frequency and amplitude. With an external laser interferometer present, phase and amplitude of the oscillations can be calibrated, and the interferometer mounted on the granite can be used for realtive measurements in x and y directions across the neutron mirrors.

For the reasons just described, such a quasi external interferometer was implemented within the vacuum chamber. An aluminium frame only mounted on threaded bolts of the front ends of the vacuum chamber was designed, where a laser interferometer and corresponding optical elements can be mounted. Figure 8.5 shows a rendered image of the setup within the lower half of the vacuum chamber, with the frame for the external laser interferometer visible. Oscillations are dampened out extensively before they could arrive at the external interferometer from the granite plate: The frame is only mounted on two points each on both front ends of the vacuum chamber. While the pentaprism guiding one of the laser beams towards region II is not shown in the image, the one for region IV is visible right next to the large sensor gantry (3).

For a successful first realisation of Ramsey spectroscopy within *q*BOUNCE, frequency, phase and amplitude of the neutron mirrors have to be under control. In the final setup, located at the final experimental position at the PF2 of the ILL, the measurements presented in the following sections have been carried out. After introducing the components used as well as their respective positions in the setup, the frequency stability and the oscillation amplitudes in the system as well as the relative phase between the oscillating mirrors is analysed.
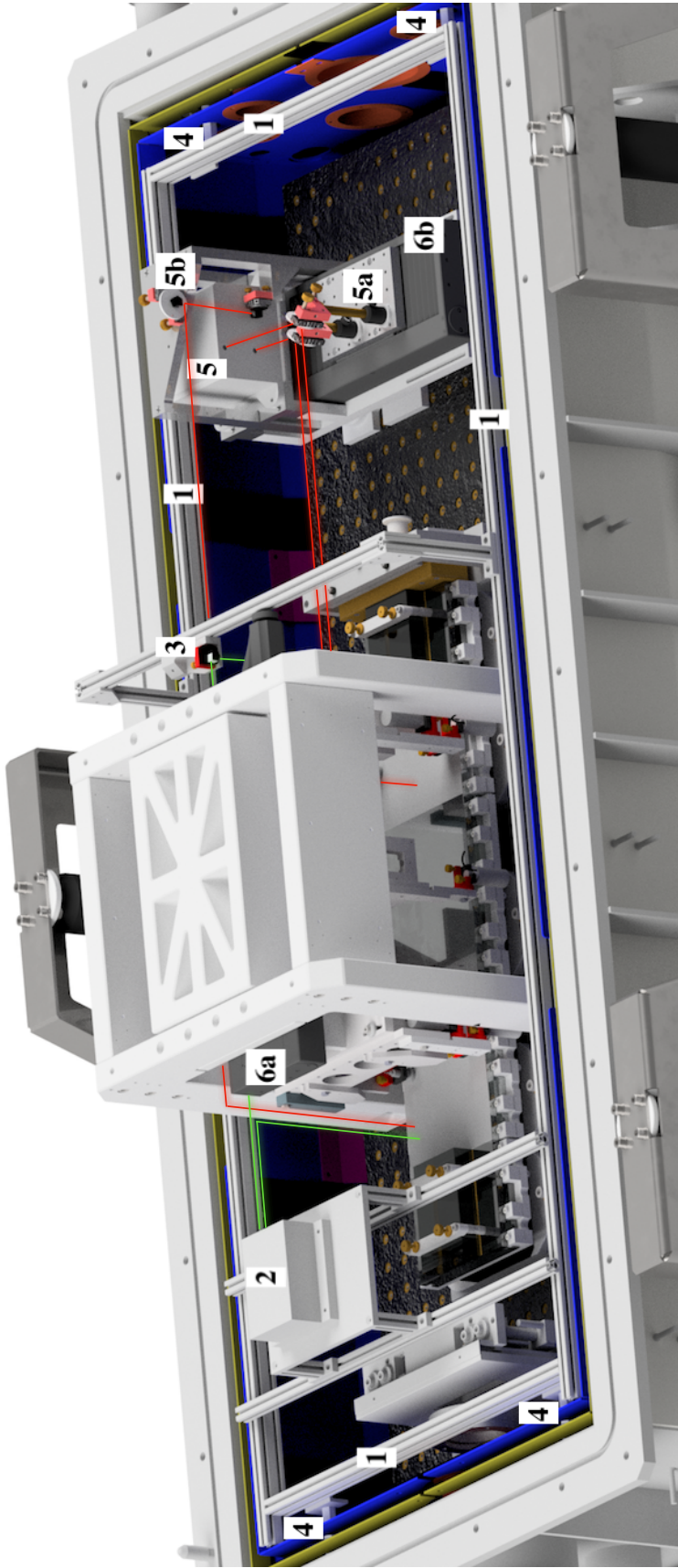
Figure 8.5.: An additional aluminium frame (1) for installing a laser interferometer (2, with green laser beam paths) and corresponding optical element (3, to the right side of the sensor gantry) without directly touching the granite plate or any other components than the front ends of the vacuum chamber (4). Furthermore, the internal laser interferometer (5, with red laser beam paths) with two adjustable laser beams (5a, through linear stages 6a and 6b) and one fixed (5b) laser path is shown.
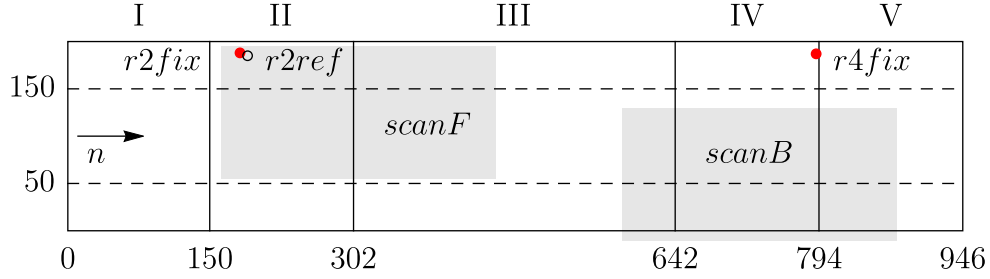
Figure 8.6.: Schematic representation of the areas reachable by the two laser beams *scanF* and *scanB* of the internal laser interferometer (5a in figure 8.5) within the Ramsey-setup (shaded areas). The black circle is the third laser beam (*r2ref*) of the internal interferometer (5b in figure 8.5), which has a fixed position. The two red disks (*r2fix* and *r4fix*) represent the fixed positions of the laser beams coming from the external interferometer (2 in figure 8.5). The length and width of the setup is shown millimetre.

Scannable Regions of the Laser Beams

Figure 8.6 shows the five neutron mirrors of the Ramsey-setup. Neutrons enter from the left, as indicated. The two shaded areas depict the regions scannable by two beams of the internal laser interferometer (henceforth *scanF* for the left (towards the front) and *scanB* for the right one (towards the back side)), which is placed on the SIOS stage on the granite to the right-hand side in figure 8.5. The travelling path of the lasers that is defined by the two linear stages involved, is restricted due to technical reasons and obstacles in the optical path. The black circle in figure 8.6 indicates the fixed reference positions of the third beam of the internal interferometer (*r2ref*). The two red disks represent the two fixed positions of the laser beams from the external laser interferometer (*r2fix* and *r4fix*). Finally, the dashed lines represent the area from which neutrons are detected in the end (width between the spacers in the mirror-absorber setups).

Frequency Measurements

The frequency applied to the nanopositioning tables in following measurements via an arbitrary frequency generator (AFG)[13] was 462.925 Hz, which is the resonance frequency for a gravitationally bound ultracold neutron to induce a transition from $|1\rangle$ to $|3\rangle$.

Measurements of regions II and IV, by *scanF* and *scanB*, respectively, yield a frequency of $\nu = 462.912(10)$ Hz throughout the accessible area. The lasers *r2fix*, *r2ref*, and *r4ref* give the same result. The error arises from the fourier transform of the rawdata with 20 000 datapoints and a sampling rate of 2517 Hz, yielding an error of ± 0.126 Hz. This precision can readily be increased by changing the
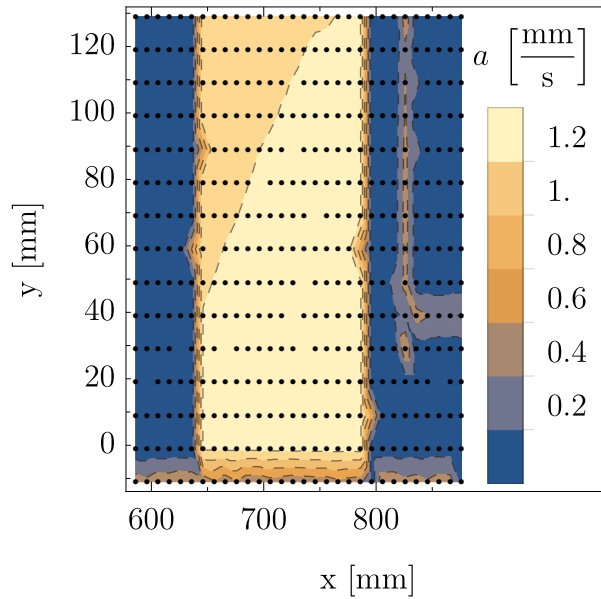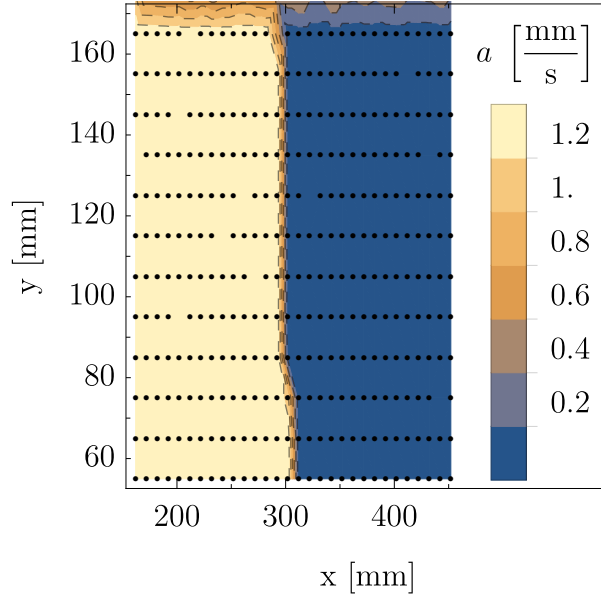
---

[13]Tektronix AFG 3102

Figure 8.7.: Amplitudes measured by laser beam *scanB* of regions III to V. The image corresponds to the right shaded area in figure 8.6. Black dots represent positions of data taking. Below $y = 0\,\text{mm}$, artefacts are visible where the laser beam approaches the end of the mirror.

settings for data taking. Thus, the frequency stability of the oscillations is sufficiently under control for a first realisation of the experiment.

As shown in figure 8.6, the lasers can also scan regions III and V. Measurements on these non-oscillating regions also yield results of the applied frequency. Therefore, it is important to check for the corresponding oscillation amplitudes of the neutron mirrors, to make sure that oscillations are sufficiently small in all but the perturbation regions of the Ramsey setup.

Amplitude Measurements

For the same measurements just discussed with respect to the frequency stability, figures 8.7 and 8.8 show the corresponding measured amplitudes from *scanH* and *scanB*, respectively. Firstly, the measurements show that any oscillations on regions other than II and IV are below $0.1\,\text{mm/s}$ and therefore negligible (compare figure 5.4). The structures on the right-hand side in figure 8.7 seem to come from the absorber mounting of the mirror, but since the absorber mirror itself is not oscillating this was not further investigated. The absolute amplitude of the oscillating regions is crosschecked with the external laser interferometer to avoid influences of parasitic oscillations, and the scanning laser beams are used to examine the mirrors' global behaviour. Along the mirror of region IV, the laser beam *scanB* shows a gradient in the oscillation amplitude of $0.1\,\text{mm/s}$ (figure 8.7), which is not the case for *scanF* (gradient around $0.03\,\text{mm/s}$, figure 8.8).

Figure 8.8.: Amplitudes measured by laser beam *scanF* of regions II to III. The image corresponds to the left shaded area in figure 8.6. Black dots represent positions of data taking. Above $y = 165$ mm, again artefacts are visible where the laser beam scans beyond the mirror surface.

An absolute amplitude of 0.1 mm/s for non-oscillating regions is negligible (compare section 5.2.1). A gradient in the oscillation amplitude of 0.1 mm/s is also negligible in most cases. In an amplitude sweep measurement (compare section 5.2.1), the effect becomes largest when measuring in the steepest slope of the transmission. Then, with current experimental parameters, an effect smaller than 5 % results. The reason for the gradient can either be due to inaccurate adjustment of the neutron mirror setup, or a false effect due to the laser beam guidance. The latter possibility is supported by the fact that even for the laser beam *r2ref*, which itself is not moving, measured amplitudes vary within the range of 0.1 mm/s during the measurements. Part of its optics are mounted on the SIOS stage (5b in figure 8.5) together with one of the linear tables (6b in figure 8.5). Another optical element of *r2ref* is mounted on the sensor gantry (where the other linear table (6a) operates). The linear tables therefore seem to influence the results of the laser measurements.

This is to be further investigated but even in the worst case the error due to this effect is similar to or smaller than statistical limitations at the moment. Thus, also the oscillation amplitudes of the neutron mirrors are in control up to the precision needed at the moment.
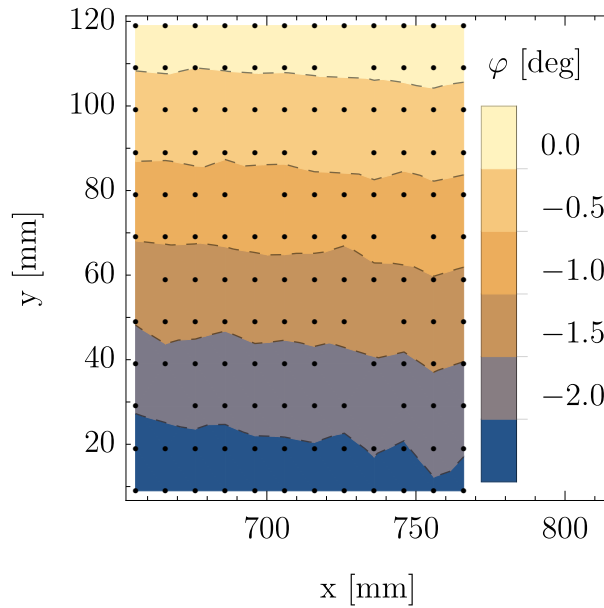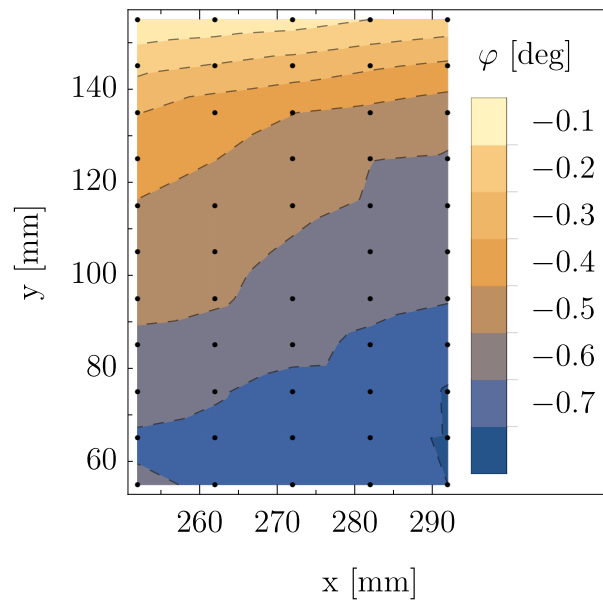
Figure 8.9.: Phase difference $\Delta\varphi$ measured on region IV between the moving laser beam *scanB* and the fixed beam *r4fix*. Compare with figure 8.6 for their respective positions. Again, black dots represent positions of data taking.

Relative Phase Measurements Regions II and IV

After the investigation of the frequency and amplitude stability of the system, another essential parameter is the phase between the two oscillating regions (compare figure 5.7) as well as the phase difference on a single mirror.

For these measurements, the external laser interferometer is a verified reference. The optical elements of the laser interferometer mounted on structures on the measurement granite, can add phase shifts that are not originating from the neutron mirrors themselves, but are due to parasitic oscillations. The external interferometer however is stable. Figure 8.9 shows the phase difference between *scanB* and *r4fix* while *scanB* was scanning region IV. Due to the mechanical restrictions mentioned already, not the full range of the mirror could be scanned, but an overall maximum phase difference of a few degrees can be estimated due to previous measurements and is negligible for now. Again, region II was performing better in this measurement (see figure 8.10), which also might be due to false effects of parasitic oscillations. This is supported by the phase difference measured between the beams of the external interferometer *r2fix* and *r4fix*, showing a phase difference below 0.2° between two points on region II and IV. Comparing with figure 5.7, this is a negligible value.

Figure 8.10.: Phase difference $\Delta\varphi$ measured on region II between the moving laser beam *scanF* and the fixed beam *r2fix*. Compare with figure 8.6 for their respective positions. As the holder of the prism reflecting beam *scanF* onto region II is blocking the path of *r2fix* below $x = 250\,\mathrm{mm}$, only a smaller area can be used to determine the phase difference between those two beams.
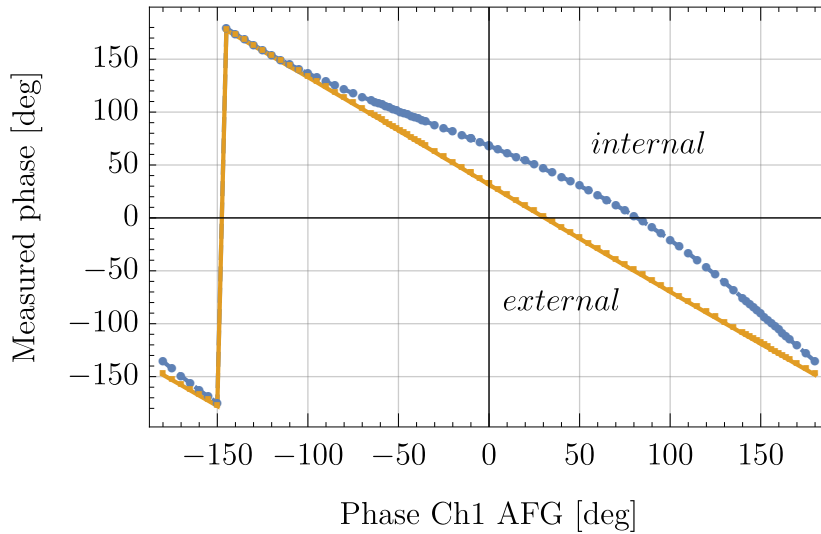
Figure 8.11.: Measured phase of internal and external laser interferometers depending on the applied phase via the AFG. The frequency applied was $392.566\,\text{Hz}$, which corresponds to the transition frequency $|2\rangle \rightarrow |4\rangle$.

Generation of In Phase Oscillations of Regions II and IV

Within the measurements presented above, the optical elements guiding the laser beams from the internal interferometer placed on the granite, were adjusted accordingly to yield results close to the external interferometer. In order to have the two neutron mirrors in regions II and IV oscillate in phase, the initial signals from the frequency generator (AFG) have to be phase shifted. This is to make up for interference effects of parasitic oscillations within the setup. The external interferometer in the vacuum chamber that is used as a reference for this and all measurements, was verified with yet another laser interferometer that was not even touching the vacuum chamber.[14]

The phase difference at the AFG that is needed for in phase oscillation of the neutron mirrors changes with the oscillation frequency. The behaviour is reproducible and the external laser interferometer installed in the vacuum chamber proofs to be reliable and important.

To illustrate this, measurements have been performed where the phase between the output channels of the AFG for the two nanopositioning tables was swept through from $-180°$ to $180°$ with 92 data points. Figure 8.11 shows the results for two laser beams of the internal as well as the external interferometer used, each of them measuring a phase difference between region II and IV. The externally measured phases show a linear dependency between applied and measured phase, as expected. The offset at AFG phase zero shows the interference behaviour

---

[14]A guard railing that is placed all around the UCN platform of the PF2 was used to mount a connecting bar across the platform, slightly above the vacuum chamber. Above the mirror setup, the laser interferometer and corresponding optical elements were fixed to that bar.

mentioned above, meaning that a phase offset has to be fed to the nanopositioning tables to achieve in phase oscillating neutron mirrors[15]. For the largest phase difference of $\pm 180°$ (plus offset), the measured phase differences are minimal. Thus, measurements like this can in principle serve as lookup tables for the phases of the internal interferometer, although the use of an external one is more convenient.

In summary, the previous sections showed that systematic effects can occur when measuring the spatial behaviour of two neutron mirrors that oscillate simultaneously. This can either be addressed by mechanical adjustments (which are impractical as the vacuum chamber would have to be opened between switching frequencies) or via look up tables. However, as long as an independent external laser interferometer can be used for calibration, this is not mandatory as relative measurements between two laser interferometers yield satisfying results.

8.2.2. Height Alignment of Neutron Mirrors

Besides the laser interferometers that are used to monitor the neutron mirror oscillations, another method to control the positions of the neutron mirrors is via the use of capacitive sensors. Within qBOUNCE, relative measurements with capacitive sensors that are moved along the neutron mirrors, are performed to control the height alignment of the mirrors. This principle has been implemented by Hanno Filter in **Cronenberg** (2016) and was also used in **Thalhammer** (2019). The concept has been extended and adapted for the larger setup of five neutron mirrors.
In this section, first an estimation of the needed precision of the steps between neutron mirrors shall be given. Second, problems that have been encountered in the measurements of the steps are discussed. Therefore, the linearity of the capacitive sensors has been measured and will be presented here. Third, measurements of steps of a five part Ramsey-setup will be described.

Estimation of Needed Precision

Ideally, no upward or downward steps are present between subsequent neutron mirrors. If steps occur, however, there mainly are two issues. First, in the case of a step upwards, the neutron wave function will be reflected with a certain probability. This means that there is a loss in transmission. The neutrons that are still transmitted, will partly change their energy states — tending to lower states. Second, in the case of a step downwards, reflection will be low (but not zero, in a quantum mechanical description, see **Reiter et al.** (2009)). The transmitted neutrons can again undergo transitions to other states, but in this case transitions to higher states are more likely.

---

[15]This has been checked of course for different frequencies, where this offset changes. Therefore, it is ruled out to a great extent that the offset arises from other sources like electronic processing in the piezo controller or the like.
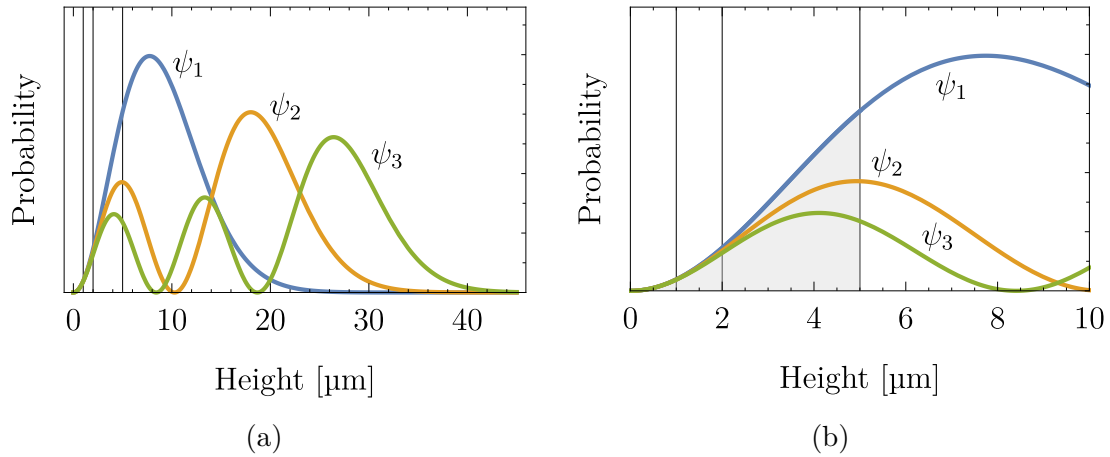
Figure 8.12.: Square of the wave functions of eigenstates ψ_n of a neutron above a mirror (a), and their respective overlap (grey) with upward steps of one, two, and five micrometer, respectively, in detail (b).

Table 8.2.: Overlaps of wave functions ψ_n with upwards steps of different heights s in percent.

	$s = 1\,\mu m$	$s = 2\,\mu m$	$s = 5\,\mu m$
ψ_1	0.16	1.25	15.42
ψ_2	0.16	1.20	11.91
ψ_3	0.16	1.16	9.65

It is noteworthy, that these processes also occur in the case of neutrons entering an oscillating region. Due to their periodical displacement around their rest position (with ideally steps of zero to the other neutron mirrors), steps in either direction occur. This case is more complex, however, and needs a more careful treatment than the one presented here.

Suppose a neutron above a mirror. The wave functions for the first three eigenstates are shown in figure 8.12a. For steps upwards, the overlap between the wave functions and steps of one, two, and five micrometers, respectively, is depicted in figure 8.12b, which is a zoom into figure 8.12a. The vertical axis represents the probability to find a neutron at a certain height. Thus, the overlap between step and wave function of the neutron can be calculated, and is an estimate of the reflected percentage. The same approach has been used in **Wautischer** (2015); **Schmidt** (2017). Of course, this needs a quantum mechanical calculation for precise results, which shall not be covered here.

In this approximation, the overlaps of the wave functions and steps of different heights are summarised in table 8.2. Upward steps of less than $2\,\mu m$ yield reasonably small overlaps in the percent range.

(a)	1	2	3	4	5
5	0.1	0.2	0.5	2.8	92.6
4	0.1	0.4	2.3	93.7	1.5
3	0.3	1.7	94.8	1.3	0.4
2	1.1	96.2	1.1	0.3	0.2
1	97.8	0.8	0.3	0.1	0.1

(b)	1	2	3	4	5
5	0.3	0.7	2.0	12.8	73.3
4	0.5	1.6	10.4	76.9	4.0
3	1.2	7.9	80.9	3.6	1.2
2	5.0	85.7	3.2	1.1	0.6
1	91.9	2.4	0.9	0.5	0.3

(c)	1	2	3	4	5
5	0.3	0.8	2.8	74.1	9.5
4	0.9	3.2	64.3	15.2	2.7
3	3.2	51.3	23.8	3.9	1.6
2	33.7	37.5	5.2	2.2	1.2
1	61.5	6.6	2.7	1.6	1.1

Figure 8.13.: Transition probabilities in percent for neutrons from state i (horizontal axis) to state j (vertical axis), at downward steps of one (a), two (b), and five (c) micrometer, respectively.

For the transition of the neutron in state i to another state j at a step, the probability is given by the overlap of the two wave functions:

$$P_{ij} = \langle \psi_i | \psi_j \rangle = \int \psi_i^*(z)\, \psi_j(z + s)\mathrm{d}z \ . \qquad (8.3)$$

Here, s denotes the corresponding step, which is a downward step for positive values. For the same step heights as above, one, two, and five micrometer, the transition probabilities for the first five eigenstates of the neutron are shown in figure 8.13. For $s = 0$, only the diagonal elements would be green and would read 100 %, with no transitions taking place. This is only true for a step between two mirrors without an absorber mirror atop. The case of an upper mirror above the first neutron mirror is covered in **Cronenberg** (2016). For estimation purposes, the case presented suffices for both scenarios. For downward steps in figure 8.13, a 5 μm step between the mirrors yields high transition probabilities. For example, there is a 33.7 % probability for a neutron in the ground state to be excited to the second state, falling down a step of 5 μm (figure 8.13c). The probabilities decrease for a step of 2 μm (figure 8.13b), and give acceptable results for 1 μm steps (figure 8.13a).
Transition probabilities for upward steps (not shown here), yield similar results, at least for small steps. There, the off diagonal entries of the tables in figure 8.13 have similar values but are mirrored along the diagonal — transitions to lower energy states are favoured.

In summary, steps of one micrometer or less can be tolerated within the first Ramsey-type experiments within qBounce. Losses and unwanted transitions are at acceptable values for such small steps.
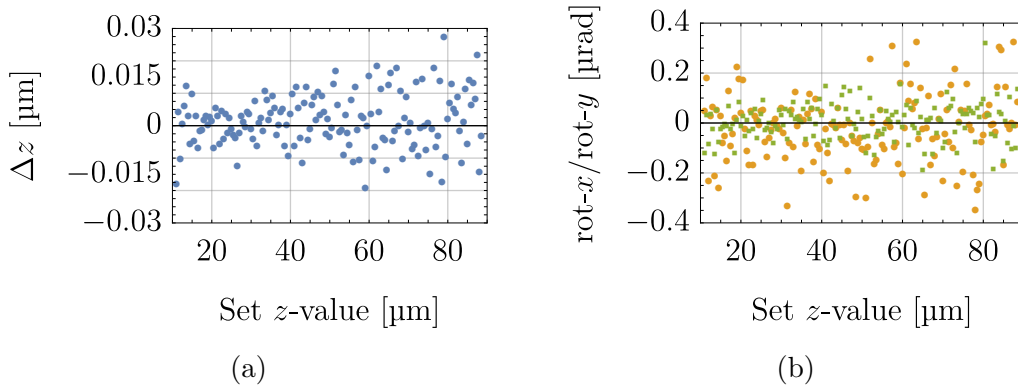
Figure 8.14.: Internal sensor outputs of a nanopositioning stage driven from 11–88.5 µm. The difference from the set z-value to its internal sensor output (a) as well as the output of the rotational (x — dots, orange & y — squares, green) axes (b) are shown.

Capacitive Sensor Linearity

The capacitive sensors are used to align the neutron mirrors relative to each other. The sensors measure the capacitance (and therefore the a distance) by generating a homogeneous electric field between sensor and probe, in this case neutron mirrors. Although absolute measurements of the distance would be feasible, within the setup presented only relative measurements are performed. In order to use capacitive sensors reliably for the reconstruction of steps between neutron mirrors, their linearity is crucial. Although the sensors ship with calibration protocols, which show non-linearity below critical values for the experiment ($< 0.03\,\%$), a check within the setup in qBOUNCE is necessary: The neutron mirrors exhibit a non-conductive protective layer of SiO_2 above the conductive Al layer that the sensor is referencing to, and this influences the sensors' behaviour. This issue, the sensors' linearity in a typical neutron mirror setup within qBOUNCE (see section 8.1.2), is addressed in the following test.

A nanopositioning stage[16] that is operating well within the stages' specifications, is used to move a neutron mirror in vertical direction. It exhibits a maximal non-linearity of $0.0345\,\%$ according to its calibration protocol, and therefore yields a reference for testing the capacitive sensors' values. The capacitive sensors are placed above the neutron mirror at a fixed height, and measure relative height changes to the mirror. Driving the nanopositioning table that has a range of 0–100 µm from 11–88.5 µm, its internal sensors output the values shown in figure 8.14 for height z and rotational axes rot-x and rot-y.

Although the variation of Δz rises for increasing set values (figure 8.14a), the stage is very stable and deviations negligible. The rotational axes that are fixed to zero, are stable as well (figure 8.14b) even though the rot-x axis (dots, orange) exhibits higher fluctuations than the rot-y axis (squares, green). This is due to

---

[16]PI "518a", Ser. No. 112063142.
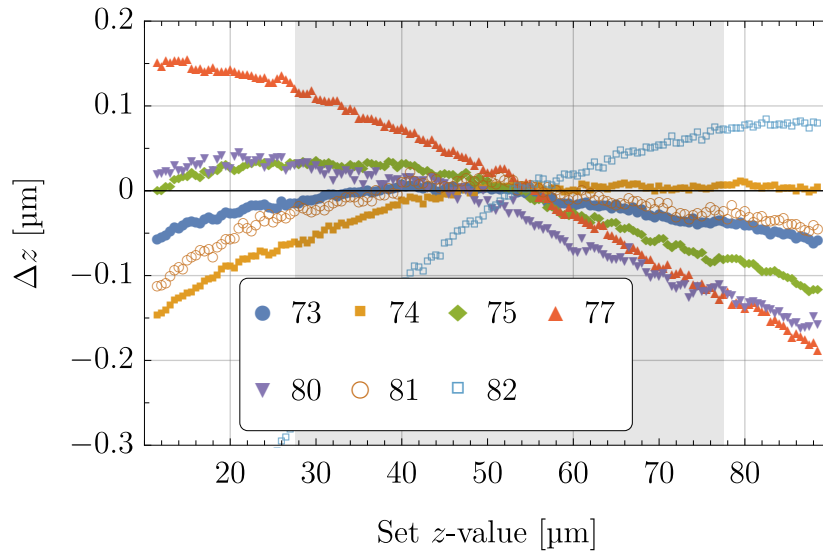
Figure 8.15.: Deviation between the feedback-controlled set values of the calibrated nanopositioning stages and the output of the capacitive sensors on top. Sensor values are here zeroed to the middle of their measurement range. The shaded area illustrates the range that is sufficient for scanning a full Ramsey-setup. Sensor #77 and most of all #82 show behaviour out of specifications.

the neutron mirror having dimensions of $152 \times 200\,\mathrm{mm}$, where the longer axis corresponds to the nanopositioning stage's rot-x axis.

Figure 8.15 shows the deviations from a set of capacitive sensors to the target value of the nanopositioning stage. The offset from the set z value of the nanopositioning stage to its real value was subtracted according to the table's calibration protocol provided by the manufacturer. Analogue measurements have been performed with the remaining sensors. Because of their individual mounting height positions, the zero-crossing is slightly different for each capacitive sensor.

The shaded area represents the range that is typically sufficient to scan over a complete five part Ramsey-setup of around $950\,\mathrm{mm}$ length (including height variations due to movement of the linear stage to which the sensors are mounted). Non-linearity in this area of $50\,\mathrm{\mu m}$ is less than $0.15\,\mathrm{\mu m}$. The errors become even smaller locally (e. g. at a position of steps between two mirrors) and are therefore negligible. The two sensors performing the worst in this measurement are sensors #77 and #82, where #82 also showed scratches on the sensitive area due to transportation or handling. The sensors will be replaced.

Measurements of Steps between Neutron Mirrors

With a set of seven capacitive sensors, all five neutron mirror regions can in theory be aligned to each other (relative to a sixth reference mirror), with satisfactory precision for the experiment presented. Figure 8.16 shows a sketch of the mirror
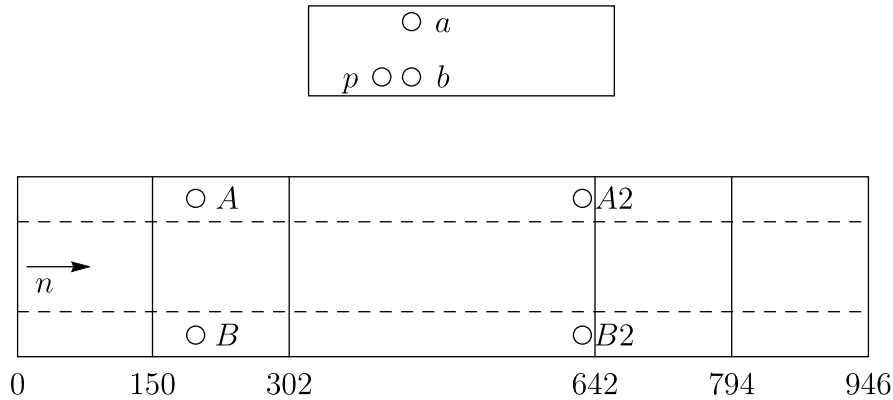
Figure 8.16.: Schematic setup of seven capacitive sensors above five consecutive neutron mirrors (where neutrons enter form the left) and one reference mirror. The reference sensors small a, b, and pitch p, map the vertical movement of the linear stage above, which can be corrected for in the data of the four main sensors A, B, $A2$, and $B2$.

setup with labelled capacitive sensors, and the sensors mounted in the setup can be seen in figure 8.1. All sensors can move along the mirrors at a height of a few hundred micrometers, while their relative positions as well as their positions vertical to the neutron flight direction never change, as they are fixed to a linear stage above. The sensors measure their relative distance to the neutron mirrors and therefore steps between the mirrors can be calculated. The three sensors on the reference mirror, a, b, and p, are used for determining unwanted vertical variations of the operating linear stage, as the sensors always stay on a single, large mirror and span a surface. These unwanted movements in height as well as roll (in neutron flight direction) and pitch (normal to neutron flight direction) angle, can be corrected for in the data of the sensors above the main setup (A, B, $A2$, and $B2$). The dashed lines in figure 8.16 represent the region where UCNs bounce along. The sensors operate outside of that region.

Under the assumption that the mounting of the capacitive sensors is rigid and does not deform during operation of the linear stage, as well as small-angle approximation for the roll and pitch movements of the linear stage's slide, a trivial relative height correction to the output of the four main sensors can be made as the sensors move along the mirrors. Here, the mirrors are assumed to be flat. In the experiment, the sensor system moves in steps from left to right, taking data at each sensor position at each step.

Let Zx_i denote a distance to mirror output of a sensor x at position i, and $\overline{xy}$ be the distance (always along the linear stages axis or perpendicular to it) between two sensors x and y. After subtracting Za_1 from all sensors at all positions i from a complete map of measurements, all further results will be relative to the value Za_1. Then, with $Zx_i = Zx$ the corrections for the measurements taken at

the points defined in figure 8.16 read

$$A_{\text{corr}} = ZA - \frac{\overline{AA2}}{2\overline{bp}}\,(Zp - Zb) + \frac{\overline{aA}}{\overline{ab}}\,(Za - Zb)\ ,$$
$$B_{\text{corr}} = ZB - \frac{\overline{AA2}}{2\overline{bp}}\,(Zp - Zb) + \frac{\overline{aB}}{\overline{ab}}\,(Za - Zb)\ ,$$
(8.4)

and

$$A2_{\text{corr}} = ZA2 + \frac{\overline{AA2}}{2\overline{bp}}\,(Zp - Zb) + \frac{\overline{aA}}{\overline{ab}}\,(Za - Zb)\ ,$$
$$B2_{\text{corr}} = ZB2 + \frac{\overline{AA2}}{2\overline{bp}}\,(Zp - Zb) + \frac{\overline{aB}}{\overline{ab}}\,(Za - Zb)\ .$$
(8.5)

The first part after the sensor height itself in every sum of the corrections corresponds to the roll correction, while the second one corresponds to the pitch correction. In a previous realisation in **Thalhammer** (2019), only the pitch correction was relevant, as the sensor system only consisted of four sensors in a row — two reference sensors and two main sensors. For a short mirror setup as the one of the realisation of the Quantum Bouncing Ball, this correction was sufficient and delivered satisfactory results.

Upon initial operation of the new sensor gantry with long neutron mirrors, patterns arose in data that should actually show flat mirrors. Tests have been performed to understand the behaviour observed, with the most important ones being:

- Change of the correction algorithm to account for errors in the distances measured between the sensors, which enter equations (8.4) and (8.5).
- Changes of the grounding of the neutron mirrors and linearity measurements depending on the distance of the capacitive sensor to the position of the grounding.
- Controlled displacement of the neutron mirrors between successive measurements.
- Measurements with additional weights on the holders of the capacitive sensors, to increase possible effects of clearance in the linear stages bearings.
- Measurements with the capacitive sensors cables moved or placed differently, as they are highly sensitive.

A number of the carried out tests has been analysed in **Feichtinger** (2018). The tests show that a predominant part of the observed deviation from flat mirror surfaces seems to arise from waviness in the mirrors themselves. With the use of large mirrors in this setup, the effects appear to the full extent for the first time. External inspection of flatness deviations has been initiated and the issue is currently under investigation.

For the mirror alignment during the experimental time in 2017 and also during the experimental times in 2018[17], a pragmatic approach was chosen: By using
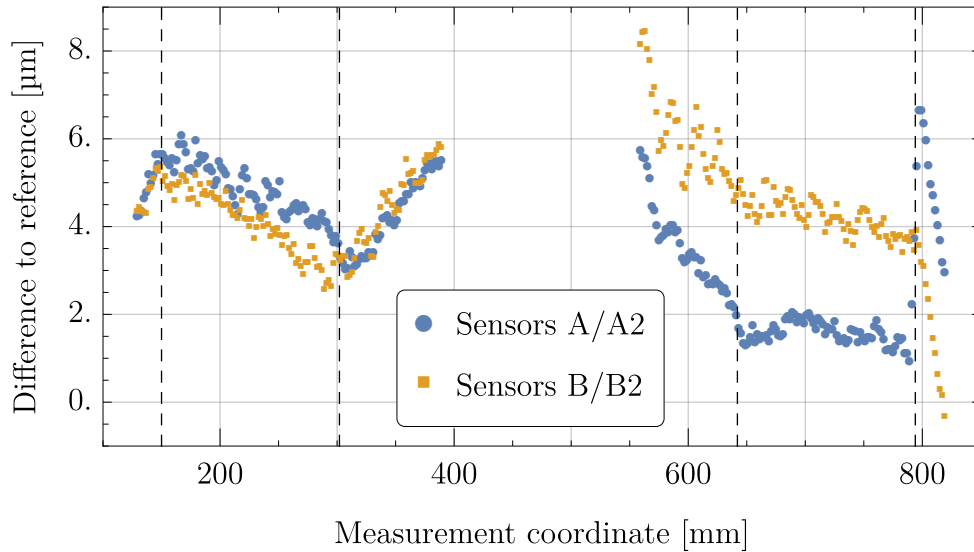
---

[17]See chapter 9 for an overview of experimental times.
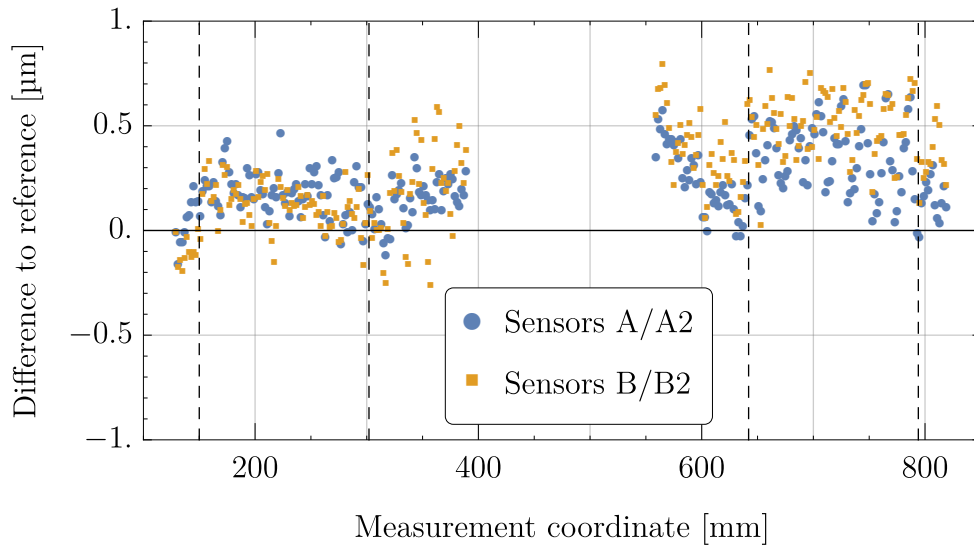
Figure 8.17.: Raw data of capacitive height measurements of ID 6.021 obtained by sensors A(A2) and B(B2), subtracted by the average of 20 reference maps. The dashed lines now represent the joints between mirrors. The variation of the data points is in the order of the standard deviation of the averaged reference map of $< 0.4\,\mu$m.

linear height gauges[18], one can manually deduce the relative step height between two aligned neutron mirrors. This is possible to an accuracy of better than a micrometer. A setup once aligned with little steps between the mirrors (in this case $\leq 0.5\,\mu$m) can be scanned with the capacitive sensors multiple times, with high reproducibility. Mirrors can from then on be readjusted with respect to an averaged reference map of the capacitive sensors.

Figure 8.17 shows data from a capacitive sensor map of measurement ID 6.021 from the experimental time in 2017, with respect to an averaged reference map. All data was recorded in vacuum. The averaged reference was obtained over around 19 hours with 20 maps (IDs 6.001–6.020). Data taking of ID 6.021 started around one hour after the end of the reference maps and frequency response tests of the nanopositioning tables have been carried out in between. Dashed lines indicate the positions of the joints between two neutron mirrors, and therefore the critical positions in terms of the neutron mirror alignment. The data points shown are raw data from of sensors A/B and $A2/B2$ (compare figure 8.16), with the reference map subtracted. The space in between (large parts of the mirror of region III) is not accessible by capacitive sensors. Regions I and V can only be scanned on the last 21 mm and the first 25 mm, respectively[19]. The difference in height between two subsequent mirrors in regions I to IV is smaller than $0.5\,\mu$m.

---

[18]Mitutoyo Laser Hologage.

[19]This is referring to the middle position of the capacitive sensor, the sensor surface has a diameter of 20 mm.

Figure 8.18.: Raw data of ID 6.021 of capacitive height measurements in vacuum obtained by sensors A(A2) and B(B2), subtracted by the average of 26 reference maps in air. The dashed lines now represent the joints between mirrors..

The result looks different when comparing a capacitive sensor map (ID 7.067) to a reference map (ID 999.2–.28) with a larger time span between the measurements. The reference maps were measured in air after aligning the neutron mirrors with the use of linear gauges, nine days before the data of ID 7.067 in vacuum was recorded. The difference between reference map and ID 7.067 is shown in figure 8.18. A global offset to the reference map of ≈ 2–$2.5\,\mu m$ is due to drifts of the coarse levelling of the mirror setup with elastomer springs (see section 8.1.2). This offset irrelevant, as only the height difference of subsequent neutron mirrors is of importance. Again, steps smaller than $1\,\mu m$ are achieved at all but one step. The graph shows a gap of around $5\,\mu m$ between regions IV and V for sensor *A*2. This has been addressed by adjusting the pitch angle (and consequently also the height) of region V appropriately. The change however lead to a drop in the measured neutron zero rate. This is possible because region V consists of a neutron mirror with an absorber above, and therefore the neutron mirror adjustment in both directions can influence the transmission. The position settings of the neutron mirror setup of region V were hence kept to the settings yielding the null rate measured right after the initial adjustments of the mirrors via linear gauges.

In summary, the mirror alignment is feasible with steps $\leq 1\,\mu m$, which is sufficient as shown in section 8.2.2.

9. Measurements with Neutrons

The experiment has the proposal number *3–14–358* at the ILL. Data presented within this thesis[1] were taken during reactor cycles n°180 and n°181[2], despite from section 9.6, where data was taken during cycles n°182 and n°183[3].

9.1. Velocity Spectrum at PF2 UCN

In the course of preparation of the *q*Bounce instrument setup at the PF2, the velocity spectra (in neutron flight direction along the beam guides) of three of the four available beam ports (UCN, EDM and TEST) were measured (see section 2.3). The MAM beam port was in use and therefore not available. The measurements have been performed together with Stefan Döge (TU Munich), with PF2 equipment: a custom designed Movatec UCN chopper with titanium blades, and a Cascade neutron detector[4] with time resolution. The full analysis of the data, as well as the velocity spectra for all beamlines, can be found in **Döge** (2018). For the UCN beam port where *q*Bounce is located, the corresponding spectrum is illustrated here.

Figure 9.1 shows the setup used for the measurements of the spectra. Chopper (3) and detector (5), are triggered externally, and the flight time of the neutron for the length of the glass neutron guide (4) is measured. An offset is present between the trigger signal and the actual opening of the chopper. For the calculation of this offset, the neutron guides (2) and (4), of lengths 45 and 60 cm, respectively, are interchanged. The corresponding velocity spectrum is depicted in figure 9.2. The data is binned and averaged for multiple runs of 120 s measurement time. The spectrum peaks at 8.0 m/s, which is in agreement with the analysis of the measurements in **Golubich** (2017).

9.2. Velocity Selector Measurements

Measuring the velocity of neutrons in flight direction (henceforth v_x) can be done with standard time-of-flight methods (like the one used in section 9.1), and any suitable chopper-detector system will be sufficient. Within *q*Bounce, such a measurement is impractical due to heavily reduced count rates and technical

---

[1] doi:10.5291/ILL-DATA.3-14-358

[2] 02.11.2016 - 22.12.2016 & 19.01.2017 - 08.03.2017

[3] 28.02.2018 - 25.04.2018 & 22.05.2018 - 12.07.2018

[4] Cascade U, CDT GmbH, Hans-Bunte-Strasse 8-10, D-69123 Heidelberg.
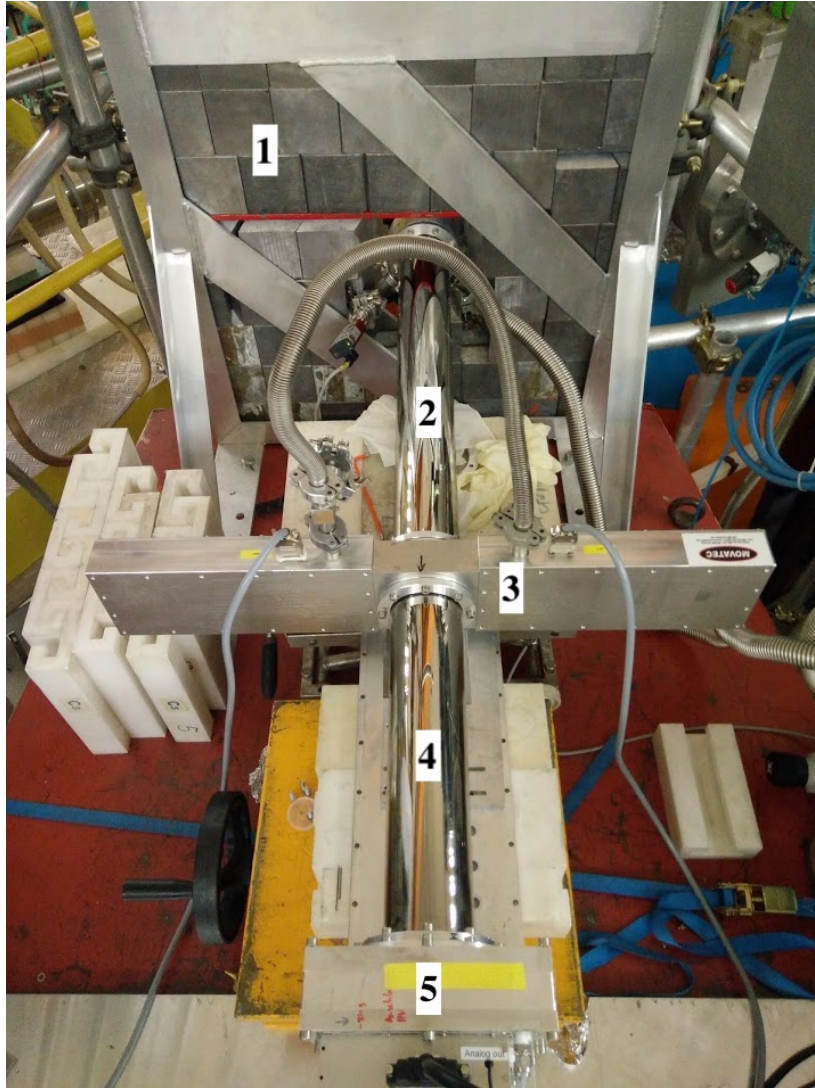
Figure 9.1.: Time-of-flight setup used at the UCN beamport of the PF2. Neutrons are coming from the turbine, located behind the biological shield of lead (1). In between two glass neutron guides (2 and 4, compare section 7.2.5) is the UCN chopper. The detector (5) is mounted on the neutron guide.
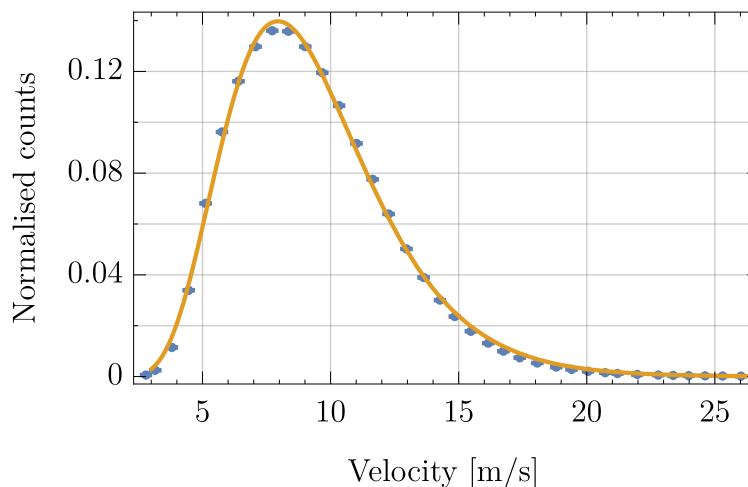
Figure 9.2.: Measured velocity spectrum of the UCN beamport at the PF2. The data was equidistantly binned. The spectrum peaks at $8.0\,\mathrm{m/s}$. A fit function of the form $f(v) = \exp\left(-a(v - v_0)^b\right)(v - v_0)^c$ is shown, and best fit parameters are displayed in table table 9.1.

Table 9.1.: Best fit parameters for the function $f(v) = \exp\left(-a(v - v_0)^b\right)(v - v_0)^c$ of the measured UCN spectrum, shown in figure 9.2.

Parameter	Best fit value	Parameter	Best fit value
v_0	0.772086	a	11.7793
b	0.474257	c	14.2208

difficulties (e. g. space, vacuum). In 2016, the incoming velocity spectrum in the experimental setup was measured with the re-engineered velocity selector system presented in section 8.1.1. An incremental approach was chosen for tuning the heights of the blades. For each measurement, both blades were adjusted, yielding settings for transmission of velocity ranges of $1\,\mathrm{m/s}$ (3–$4\,\mathrm{m/s}$, 4–$5\,\mathrm{m/s}$, and so forth).

Figure 9.3 shows the resulting data, with the grey area illustrating the spectrum for the final blade positions. The slitheight was $l = 100\,\mu\mathrm{m}$, and data is corrected with respect to beam monitor rates. Against expectations, there is a noticeable dip in the velocity spectrum at 8–$9\,\mathrm{m/s}$. This datapoint was remeasured and obvious systematic causes like the height of the blades or misalignments in the setup were ruled out. Furthermore, this structure was seen in the results of analogue measurements in 2018 with $l = 30\,\mu\mathrm{m}$.

While an expected maximum around or below $8\,\mathrm{m/s}$ shows in the data (compare section 9.1 and **Jenke** (2011); **Cronenberg** (2016)), some process generates another maximum at higher velocities. Mixing of different velocity components for the geometrical specifics of the current setup, and suppression of slower
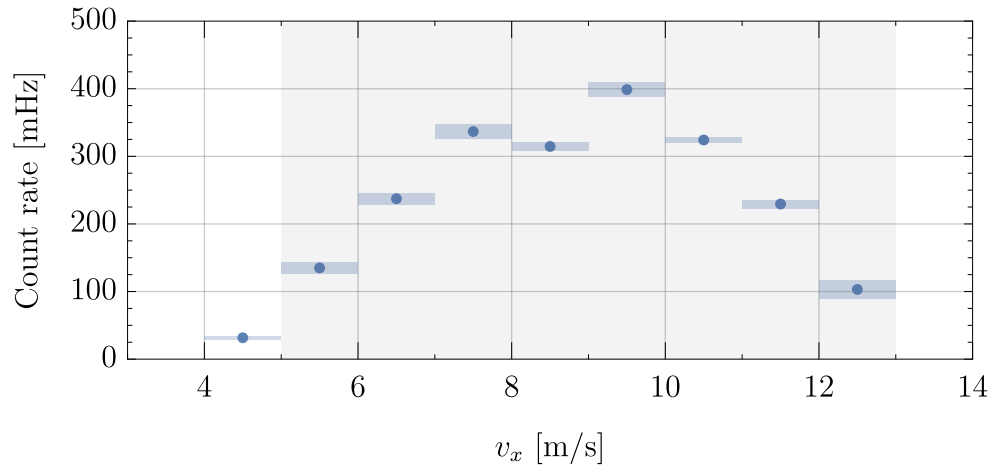
Figure 9.3.: Incrementally measured distribution for the neutrons' velocity in flight direction v_x with a slitheight $l = 100\,\mu\text{m}$. The error box around each measurement shows statistical errors (vertically) and the selected v_x range per measurement (horizontally). The spectrum for the blade positions in their final place for further measurements is shown in grey. Taking measurement errors of the height of the blades into account, this results in $(5.0 \pm 0.2) - (13^{+0.43}_{-0.39})\,\text{m/s}$ for the idealised classical model.

neutrons in the mirror absorber system should be investigated. In addition, a yet missing quantum mechanical description through a path integral is desirable. However, a proper time-of-flight measurement should be aimed for in the future, to better understand the incoming velocity spectrum of the UCNs.

9.3. State Preparation and Analysis

The occupation numbers of the neutrons' energy eigenstates after region I and V, respectively, were determined. This was done by spatially measuring the absolute value of the square of the wave function. The consistency of the method was checked within this thesis, by also measuring the state occupation after region I and V in series, and comparing the results to the individual measurements.

Measurements

For the measurements, ^{10}B-coated CR-39 detectors[5] (see section 8.1.3) were used. Figure 9.4 shows the experimental setup for the measurement of a single mirror-absorber region with a detector placed behind, as well as the aluminium holder with a mounted detector. After measurements, the boron coating was removed promptly from the detector, to ensure low background. The detectors

---

[5]Partially, detectors developed in **Filter** (2018) were used.

(a)   (b)
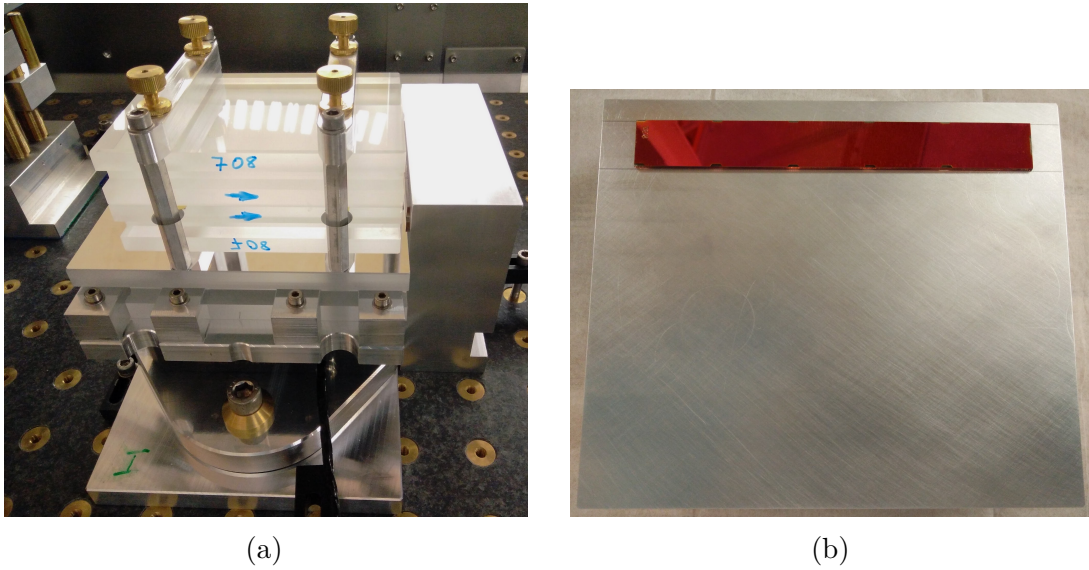
Figure 9.4.: (a) Mirror-absorber region with placed CR-39 right after. Neutrons enter from the left. (b) Aluminium CR-39 holder with adjusted detector.

were then etched and microscoped. Neutron traces on the CR-39 were detected using image and pattern recognition methods, in a half automated, half manual procedure (see e. g. **Jenke et al.** (2013)).

The result can be can be fitted[6] with the square of the absolute of the wave function, which is the incoherent sum of the individually populated states $\varphi_n(z, t_1)$ at measurement time t_1:

$$|\psi\left(z, t_1\right)|^2 = N \sum_n |C_n(t_1)| \left(|\varphi_n(z - z_0)|^2 * f(z, \sigma)\right) + N_0 \ . \qquad (9.1)$$

Here, N is an arbitrary parameter for the norm, $C_n(t_1)$ are the occupation parameters of interest, z_0 is the unknown height offset of the neutron trace on the CR-39, $f(z, \sigma)$ is a gaussian function of the spatial resolution σ, and N_0 is the background (see **Jenke** (2011)).

For the velocity spectrum of 5–13 m/s, as used in the experiment, three measurements were carried out:

- after region I,
- after region V,
- and after region I and region V in series.

For the preparation **region I**, with a measured mirror-absorber distance of $l = 25\,\mu\text{m}$, 2265 neutrons have been detected on CR-39 ID T37. A fit of the occupied energy eigenstates to the measured data points is shown in figure 9.5a.

---

[6]Mathematica packages from Tobias Jenke were used.

Table 9.2.: Best fit results and one sigma errors for the occupation numbers of the energy states one, two, and three, for the mirror-absorber systems of region I, V, and I plus V in series. The square of the absolute value of the wave functions was each measured with CR-39 detectors. The positive error for $|C4|^2$ was taken symmetrically for both directions, due to unphysical results for negative occupation numbers.

	Neutrons	$|C1|^2$ [%]	$|C2|^2$ [%]	$|C3|^2$ [%]	$|C4|^2$ [%]
Region I, *ID T37*	2265	$52.1^{+2.2}_{-2.2}$	$36.6^{+3.4}_{-3.6}$	$10.7^{+2.3}_{-3.3}$	$0.7^{+4.7}_{-4.7}$
Region V, *ID L06*	12232	$45.9^{+0.9}_{-1.0}$	$43.1^{+1.6}_{-1.7}$	$11.1^{+1.1}_{-0.9}$	$0.0^{+0.5}_{-0.5}$
Regions I+V, *ID 129*	7147	$59.2^{+1.2}_{-1.0}$	$37.9^{+1.8}_{-2.3}$	$3.0^{+1.4}_{-1.2}$	—
Calculated I+V		58.5	38.6	2.9	

Above the height of $26\,\mu\text{m}$, the bins are not equidistant anymore. This is to keep statistical methods applicable with a sufficient number of neutrons per bin, and is accounted for in the fit.

The corresponding measurements for **region V** (12232 neutrons, $l = 26\,\mu\text{m}$, CR-39 ID L06) and **regions I plus V** (7147 neutrons, CR-39 ID 129) are shown in figure 9.5b and figure 9.5c, respectively. The reduced χ^2 of the fits are $\chi^2_{\text{red,I}} = 1.15$, $\chi^2_{\text{red,V}} = 1.61$, and $\chi^2_{\text{red,I+V}} = 0.99$.

Comparison of the Measurements

For regions I and V, the first four eigenstates were included in the fit to determine their corresponding occupation numbers, whereas for the measurement of regions I+V in series, the fourth state can be neglected as it is sufficiently suppressed. The results are displayed in table 9.2. From the occupation numbers for region I and region V, the expected state occupations transmitted in the measurement of both regions in series can be calculated:

$$\frac{|Ci|^2_I \times |Ci|^2_V}{C_{\text{norm}}} = |Ci|^2_{I+V} \ , \tag{9.2}$$

with $i = \{1, 2, 3\}$, and $C_{\text{norm}} = |C1|^2_I \times |C1|^2_V + |C2|^2_I \times |C2|^2_V + |C3|^2_I \times |C3|^2_V$. These calculated estimations are shown in the last line of table 9.2, and compare to the measured occupation numbers one row above. The results are in good agreement, and the measurements show remarkable consistency of the method used.

9.4. Zero Rate Stability

A recurring problem in qBOUNCE since **Cronenberg** (2016) has been the exponential decrease of the zero rate. As was confirmed later, the reason was grease
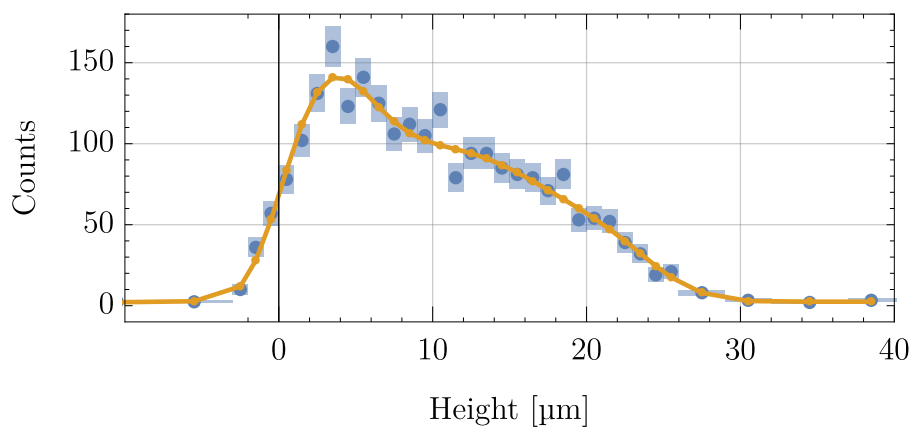
(a)
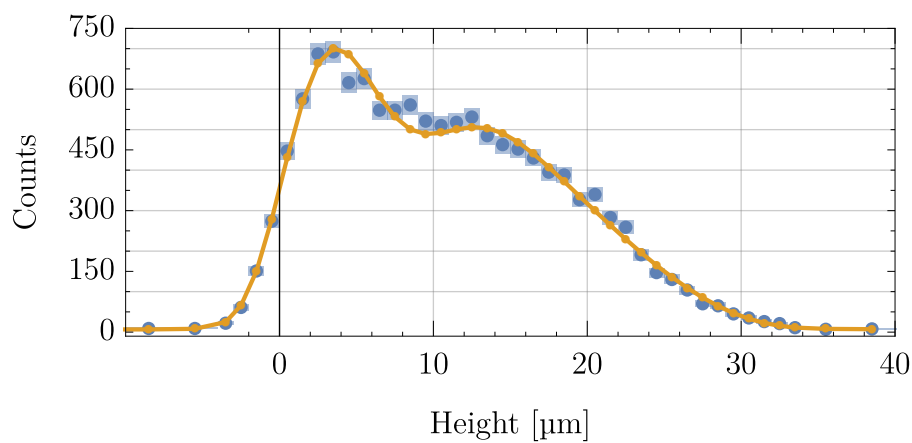
(b)
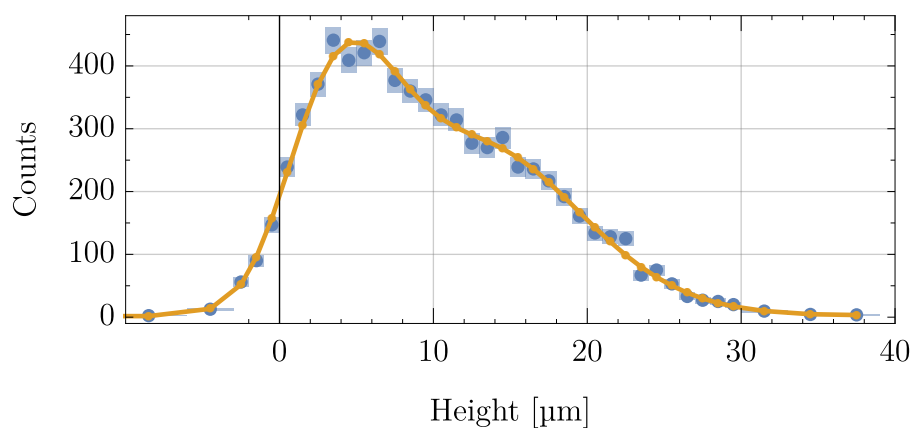
(c)

Figure 9.5.: Binned histograms of a CR-39 measurements of regions I (a), V (b), and I plus V (c). The rectangles' height around the data points represents the statistical error, the width is the bin width. The solid line connects the points of best fit at height of the binned data points.

Table 9.3.: Fit parameters for an exponential decay of the initial zero rate r_0, final rate r and mean lifetime τ. The standard errors correspond to one sigma.

	Estimate	Standard Error	Confidence Interval
r_0 [mHz]	30.68	1.33	[29.28, 32.08]
r [mHz]	14.65	1.04	[13.56, 15.75]
τ [d]	2.75	0.70	[2.02, 3.48]

Table 9.4.: Counter tube characterisation parameters on site at PF2, ILL, within a region of interest of channels [145, 950].

Background	Error	Livetime	# neutrons	# measurements
0.45 mHz	0.03 mHz	492 393 s	222	38

in the linear tables of the sensor gantry and the SIOS stage. In the process of finding these errors, the following changes and tests were made *without* success:

- Thorough cleaning of the inside of the vacuum chamber and every component installed within (e. g. MuMetal, granite, frames), to avoid oil contamination from machining residues,
- usage of oil-free vacuum pumps,
- protection against oil backflow from the roughing pump's exhaust air connection to the PF2 system by installing a zeolite trap.

Also, measurements with a residual gas analyser (RGA) have been performed. They showed signs of oil contamination, with signatures of machine oil. The linear stages that were suspected to pose a problem could only be replaced later on, and an exponential count rate drop was measured again.

The resulting zero rate stability can be seen in figure 9.6. Table 9.3 shows the corresponding fit parameters for the fit function $(r - r_0)e^{-t/\tau} + r_0$, with initial rate r_0, final count rate r and mean lifetime τ. Although the drop in count rate features similar parameters than the one observed in **Cronenberg** (2016), the mean lifetime seems much shorter in the measurement presented. This could be explained by the larger mirror surface that is subject to depositions.

9.5. Characterisation of the Counter Tube and Background Reduction

The **counter tube** (see section 8.1.3) was characterised during the measurement times at the ILL in 2016 and 2017 within 38 measurements. Table 9.4 summarises the data. Figure 9.7 shows the global detector spectrum for all main measure-
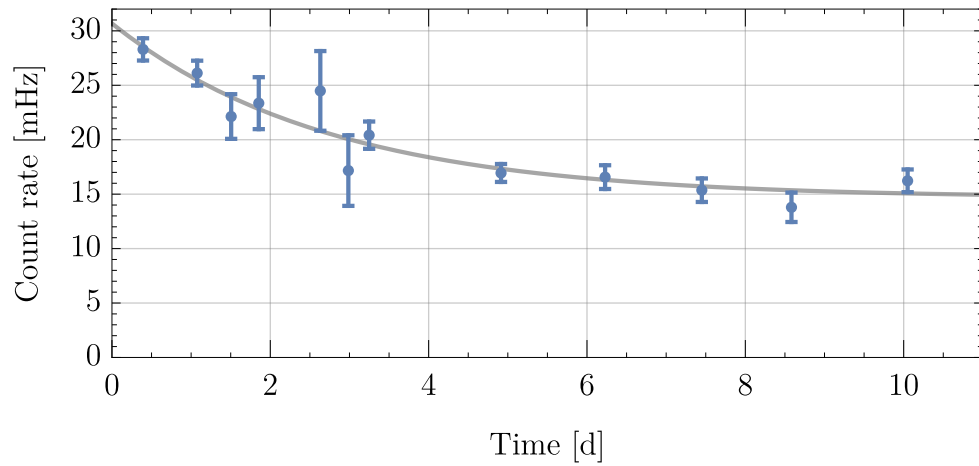
Figure 9.6.: Decay of the initial zero rate following an exponential drop (fit shown as solid line) due to depositions on the neutron mirrors. The data points are plotted at the position of the middle of their recording time and are corrected for beam monitor and background. The problem was solved in 2018.
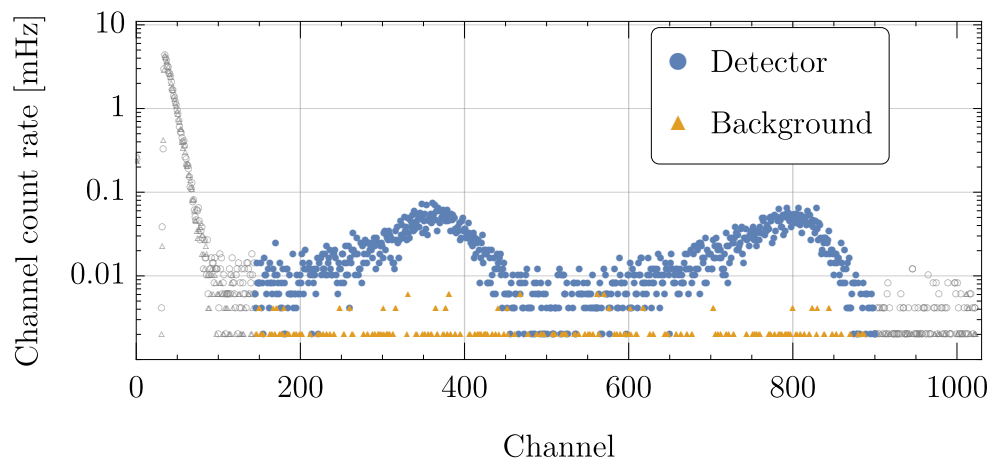

Figure 9.7.: Global detector spectrum of 38 measurements. Count rates outside of the region of interest are shown in corresponding grey hollow marks.
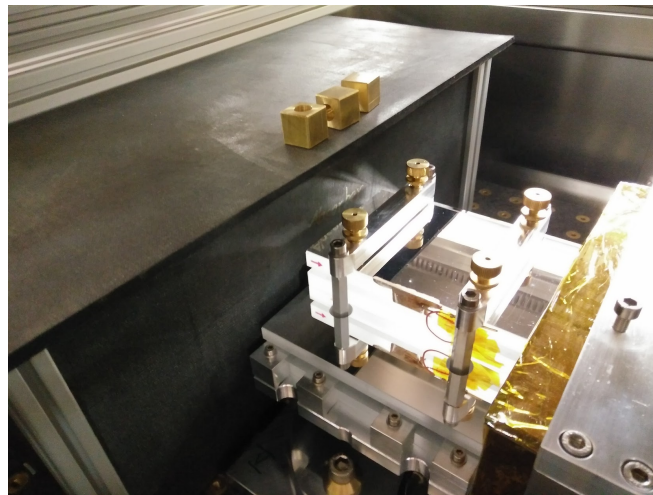
Figure 9.8.: Two layers of boron carbide mats house the collimating blades system. Only a range around the entrance slit at region I (shown in the image), is cut open so that neutrons can enter the absorber gap.

ments taken in 2017. The background of $(0.45 \pm 0.03)\,\text{mHz}$ is considered to be very low and the counter tube can readily be used for this and future experimental runs within qBOUNCE.

To reduce potential **background** of neutrons within the vacuum chamber, a shield around the end cap of the neutron beam guide (section 7.2.5) and the velocity selector system (section 8.1.1) was implemented. The boron carbide (B4C) shield is blocking any neutrons that do not enter the mirror setup as intended (see figure 9.8). Unfortunately, no direct before-after comparison measurements were performed, but measurements with open and blocked slit of the shield, respectively, have been carried out. With the slit closed[7], the count rate reduced to $(0.34 \pm 0.01)\,\text{Hz}$ from initially $(218.40 \pm 0.21)\,\text{Hz}$ with open slit in the shield. The measurements differ by a factor of over 642 and the percentage of neutrons hitting the detector without going through the slit in the shielding is very low $(< 0.2\,\%)$ and therefore negligible.

Due to their vacuum properties, the boron mats should be replaced with vacuum compatible, neutron absorbing material (e. g. boron aluminium alloys) in the future.

9.6. Ramsey Proof of Principle Measurement

This measurement, performed by the qBOUNCE team around Joachim Bosina, is to be seen separate from the other measurements presented so far, as new velocity selector measurements, CR-39 measurements for regions I and V, as well as characterisations of the counter tube have been performed prior to the

---

[7]The slit was blocked with a sheet of aluminium and a double layer of Tesa tape wrapped around.

measurement (see beginning of this chapter). Nevertheless, the same principles and procedures were applied.

An unambiguous test for Gravity Resonance Spectroscopy in Ramsey configuration built within the present thesis is a measurement of the transmission while sweeping the phase between the two oscillating regions. As explained in sections 4.2 and 5.2.2, the quantum mechanical prediction for two-state system in such a measurement is that the zero rate is to be recovered for phase differences of $\pm 180°$, and the corresponding phase sweep graph is showing sinusoidal behaviour. In 2018, such a measurement has been performed with the setup presented in this thesis. For the transition $|2\rangle \to |4\rangle$ (resonance frequency 392.566 Hz), the input phase was varied at optimal oscillation amplitude for the transition of 1.47 mm/s. The velocity spectrum was set to 5–13 m/s with the velocity selector system. Although data analysis is still ongoing, preliminary results are shown in figure 9.10.

The data[8] is corrected for detector background of (0.59 ± 0.05) mHz within the region of interest of [100,1023]. The measured count rates are normalised to two different averaged zero rates. The zero rate changed when the team was forced to do a new startup of the experiment control, including the mirror alignment. For both zero rates, raw data and the corresponding weighted means are shown in figure 9.9. The phase difference shown in the graph is the phase difference between the oscillating mirrors in regions II and IV. For a value of zero, a phase difference of $-30.8°$ was set at the frequency generator (compare figure 8.11). The monitor detector exhibited anomalies, which requires further analysis. The beam monitor was therefore not taken into account, which usually is a correction in the order of 2 %. Together with the measured data points and their statistical error bars, two least squares fits are shown: a sinusoidal and a linear fit. The linear fit gives $\chi^2_{\rm red} = 1.04$ and a probability value of $p = 0.41$, whereas the sine fit yields $\chi^2_{\rm red} = 2.86$ and $p = 1.6 \times 10^{-4}$. The sinusoidal behaviour clearly fits better than the classical expectation of a straight line. The fit functions and best fit values are listed in table 9.5.

The results can neither be explained classically (compare with section 6.3), nor by two Rabi experiments in series. The classical expectation does not exhibit significant sinusoidal behaviour, but a rather constant transmission rate independent of the phase. Two Rabi transitions in series would also not be influenced by relative phase differences of the oscillating regions. If they are, this means that the wave function exiting region II is still a coherent superposition of energy states when arriving at region IV, which is exactly the Ramsey experiment described.

The phase sweep measurement presented is proof of the worldwide first realisa-

---

[8]The IDs used for the zero rates are [3.058, 3.062, 3.08, 3.1, 3.159, 4.026, 4.069, 4.126, 4.193] and [4.361, 4.364, 4.401, 5.001, 5.034, 5.069], respectively.

Data used for the phase measurements have IDs [4.018, 4.118, 4.17, 4.178, 4.186, 4.199, 4.205, 4.211, 4.366, 4.372, 4.377, 4.396, 4.407, 4.413, 4.419, 4.426, 5.006].
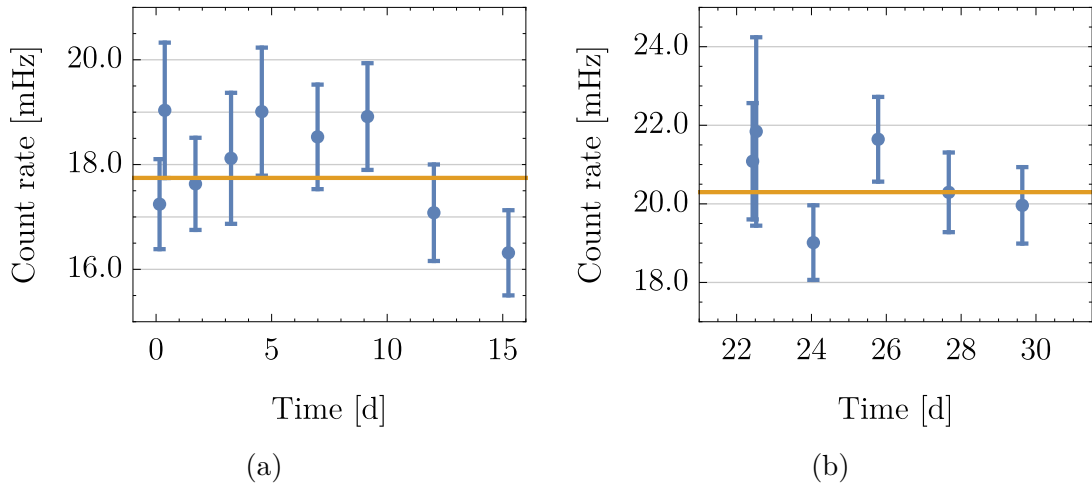
Figure 9.9.: Measured raw data of zero rates and their weighted means. The two different resulting zero rates, shown in (a) and (b), have been used to normalise the data. The zero rates are $r_a = (17.75 \pm 0.33)\,\mathrm{mHz}$, and $r_b = (20.30 \pm 0.47)\,\mathrm{mHz}$, respectively.
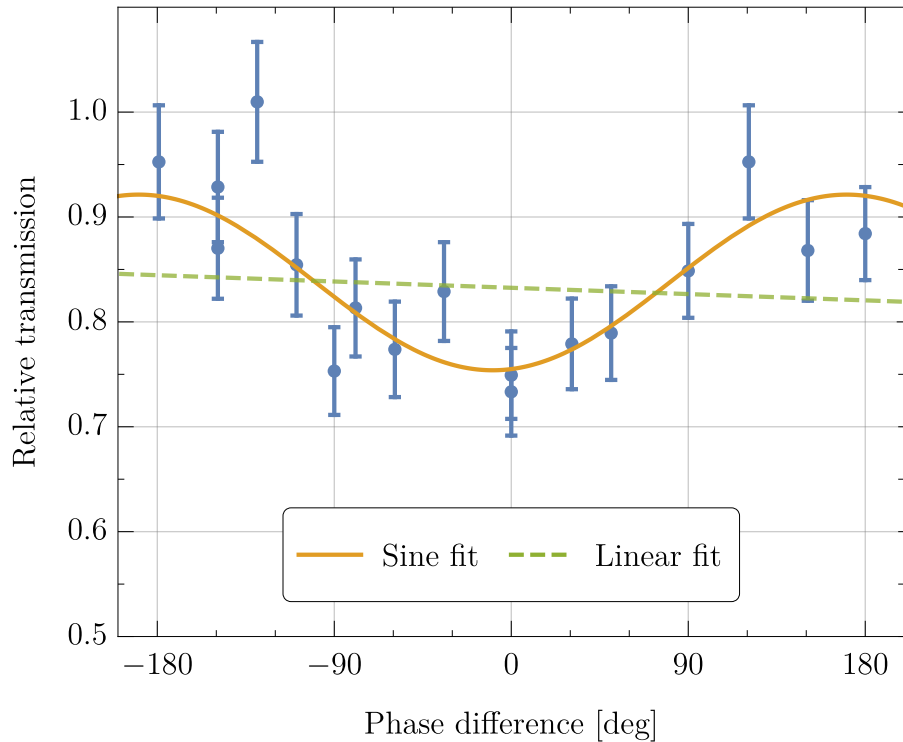

Figure 9.10.: Recorded normalised transition as function of the phase difference between the two oscillating regions. Two least squares fits to a sine function (with $\chi^2_{\mathrm{red}} = 1.04$), and a straight line ($\chi^2_{\mathrm{red}} = 2.86$) have been added.

Table 9.5.: Fit functions, best fit parameters, degrees of freedom, and resulting χ^2_{red} values for the fits shown in figure 9.10.

Function	Best fit parameters	DOF	
Sine fit: $n - a\cos\left(\gamma + \phi\right)\frac{\pi}{180}$	$n = 0.837593$ $a = 0.0837325$ $\gamma = 9.46439$	14	$\chi^2_{\text{red}} = 1.04$
Linear fit: $d + k\phi$	$d = 0.832501$ $k = -6.662 \times 10^{-5}$	15	$\chi^2_{\text{red}} = 2.86$

tion of Gravity Resonance Spectroscopy in Ramsey configuration. In addition, to the author's knowledge no other experiment before has used Ramsey's method without the use of electromagnetic radiation in the perturbation regions.

A first demonstration of quantum states of neutrons in the Earth's gravitational field was presented in **Nesvizhevsky et al.** (2002). Successful measurements of the Quantum Bouncing Ball, damped Rabi GRS, and a full three part Rabi GRS setup followed, and limits on fifth forces, dark matter, and dark energy were set (**Jenke** (2011); **Jenke et al.** (2014); **Cronenberg** (2016); **Cronenberg et al.** (2018); **Thalhammer** (2019)). After being suggested in **Abele et al.** (2010), this proof of principle for Ramsey-type GRS marks the beginning of experiments with increased precision to follow. Besides further tests of the Standard Model and continued search for dark energy and dark matter candidates to come, the first application is already underway in form of measurements of the electric charge of the neutron (**Durstberger-Rennhofer et al.** (2011)). This might lead to new limits on the electrical charge of the neutron in future Ramsey-type experiments within *q*BOUNCE.

Part IV

Summary and Outlook

10. Summary

Gravity Resonance Spectroscopy started as an elegant and versatile technique to demonstrate the quantum mechanical behaviour of neutrons above a mirror. Today, it is used to test gravity-like fifth forces, candidates for dark energy and dark matter, and the limits of Newtonian gravity. A theoretical motivation for the experiment presented in this thesis was given in the beginning.

After previous Rabi-type GRS realisations, Ramsey spectroscopy of gravitationally bound ultracold neutrons has been realised for the first time. Due to the significant increase in size of the experimental setup, a new instrument was planned and designed.

The instrument consists of a large vacuum chamber (inner dimensions of $2100 \times 900 \times 780$ mm) featuring an automated vacuum system, an embedded magnetic shield (shielding factor ≈ 100) with a well levelled granite surface plate (tilt $\approx 0.1\,\mu$rad) inside. The instrument was set up at the UCN beam of the PF2 at the Institut Laue-Langevin in Grenoble, FR. The large setup that weighs around three tons, is earthquake safe and commissioned by the ILL. The instrument can readily be used for any UCN experiment that fits into the vacuum chamber. The corresponding velocity spectrum of the PF2 UCN beam (peaking at 8.0 m/s) was measured in the course of setting up the instrument.

For the realisation of Ramsey-type GRS within qBOUNCE, a novel five-part neutron mirror setup was planned and implemented within the instrument. Auxiliary components to monitor the behaviour of the experiment, like oscillation parameters and neutron mirror alignment, were described in the thesis. The most important experimental components were characterised, and the experiment put into initial operation. The necessary requirements for the first experimental runs are fulfilled by all components. Problems with the adjustment of neutron mirror heights via capacitive sensors were encountered, and a proper work around with sufficient precision via linear height gauges presented. A new experiment control via LabView was adapted and applied to all devices needed. This provides a convenient way to control the experiment and automate measurement schemes.

Several measurements with neutrons have been performed to characterise the experimental setup. The velocity spectrum within the experiment was measured in detail. The neutron counter tube was characterised, and a recurring exponential decay in the zero count rate was observed. This problem was solved later and future experiments will operate with a stable zero rate. The consistency of the measurements of occupation numbers after preparation and analyser regions was systematically tested and found to be good. The performance of the state preparation regions I and V, however, has been better before and systematic tests

10. Summary

will follow.

The theoretical description of the Ramsey-setup was presented, and a Monte-Carlo simulation for the classical expectation of measurement schemes was performed. The results were used to confirm the proof of principle measurement with the novel Ramsey setup within qBounce: A measurement of the relative transmission while sweeping the phase between the oscillating regions. The sinusoidal behaviour observed is evidence that Ramsey spectroscopy has been performed.

This marks the first experimental realisation of Ramsey-type spectroscopy without the use of electromagnetic radiation.

11. Outlook and Future Applications

The technique of Ramsey-type Gravity Resonance Spectroscopy is a powerful one and there are many applications the presented setup can be used for. Most obvious, the increased sensitivity in comparison to previous methods allows for more precise measurements of the differences of the eigenenergies of the Quantum Bouncer in the near future. This will not only lead to further checks of quantum mechanical predictions, but with it also to constraints for various hypothetical dark energy, dark matter, or gravity-like fifth force models, as has been the case with previous experiments (see section 3.3.1). For the Ramsey setup presented, the projected short term sensitivity is in the range of $\Delta E = 10^{-17}$ eV, and the long term goal is to reach $\Delta E = 5 \times 10^{-21}$ eV.

While not being an exhaustive list, some other possibilities for measurements and applications shall be shortly summarised in the following.

A way to drive transitions to higher states than currently possible with mechanical oscillations at fixed frequency are chirped-frequency oscillations. By varying the sinusoidal oscillation frequency (chirp) in a way that the UCNs go from one energy level to the next, the occupation of high states or a certain superposition of widely separated states can be achieved (**Manfredi et al.** (2017)). Techniques like this might be used to observe the limit between quantum and classical mechanics, as the neutron energies at higher energy levels naturally become larger and eventually reach the classical regime. Transitions between two widely separated energy states also increase the parameter space for the search of hypothetical forces.

In the current experimental setup, the maximally achievable flight time T of the neutrons through the propagation region is spatially limited. Because of the crucial dependence of the energy resolution on T, it is therefore natural to make efforts to store the neutrons in this region as proposed in **Abele et al.** (2010), shifting the spatial limitation to a temporal limitation due to the finite lifetime of the free neutron.

Other experiments that are being prepared for or are underway at the moment, are for example measurements of the neutron's electric charge (see **Durstberger-Rennhofer et al.** (2011)) or spin-dependent measurements. Storing neutrons in the propagation region III of a Ramsey GRS setup has the potential to improve the current best limit on the neutron charge of $10^{-21}e$. Spin-dependent measurements can (as they have before) potentially set new limits on spin-mass-couplings of hypothetical particles like the Axion — a promising dark matter

candidate (**Moody and Wilczek** (1984); **Jenke et al.** (2014)).

In principle, one can also think of experiments where proper time effects of the energy levels involved in a transition between two largely separated eigenstates could lead to measurable phase effects. This can readily be realised with a spatial resolution detector behind the coherent evolution of the superposition of two energy eigenstates behind region III. Doing so, this might also be used to study decoherence effects of energy superpositions by varying the length of region III and the neutron velocity spectrum used.

Appendices

A. Additional Figures and Photographs

Here, additional figures and photographs shall be placed. While some are referred to in the main part of the thesis, others are meant as a supplement to complete the presentation of the carried out work.

Table A.1.: Transition frequencies for the first 5 eigenstates of a neutron above a neutron mirror.

	1	2	3	4	5
1	0	254.535	462.925	647.101	815.462
2		0	208.39	392.566	560.927
3			0	184.176	352.537
4				0	168.361
5					0

Table A.2.: Overlap integrals Q_{mn} for the first 5 eigenstates of a neutron above a neutron mirror, in units of 1/m.

	1	2	3	4	5
1	0	97373.4	-53539.9	38301.5	-30393.7
2	-97373.4	0	118935.4	-63135.7	44185.7
3	53539.9	-118935.4	0	134571.9	-70304.5
4	-38301.5	63135.7	-134571.9	0	147213.0
5	30393.7	-44185.7	70304.5	-147213.0	0
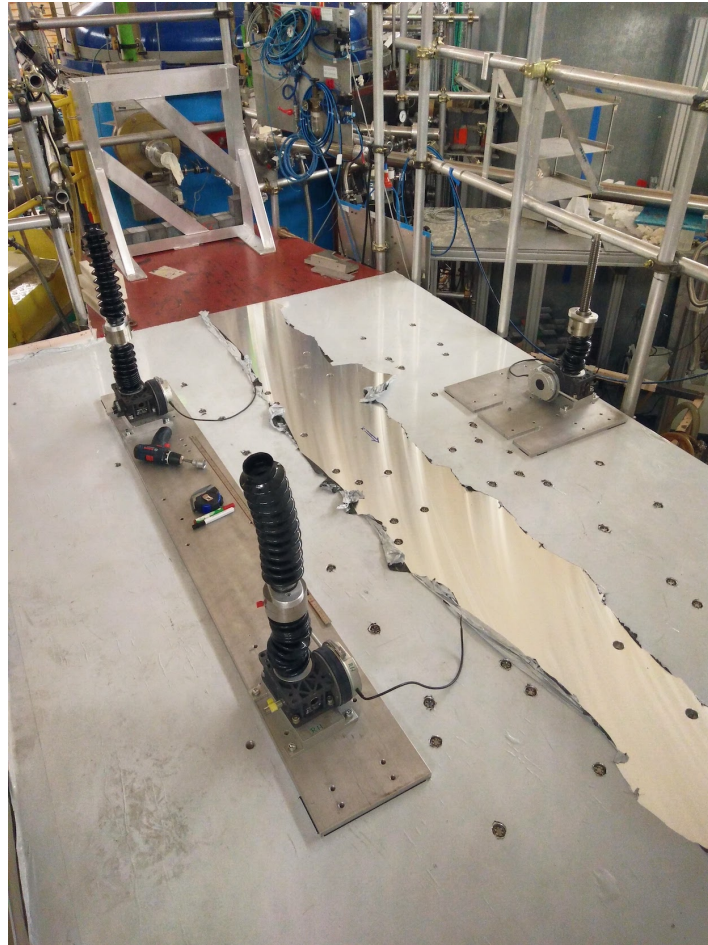
Figure A.1.: A continuous, 30 mm thick aluminium ground plate was placed on the UCN platform of PF2 (see section 7.1). The vacuum chamber is levelled via the three spindle drives visible.
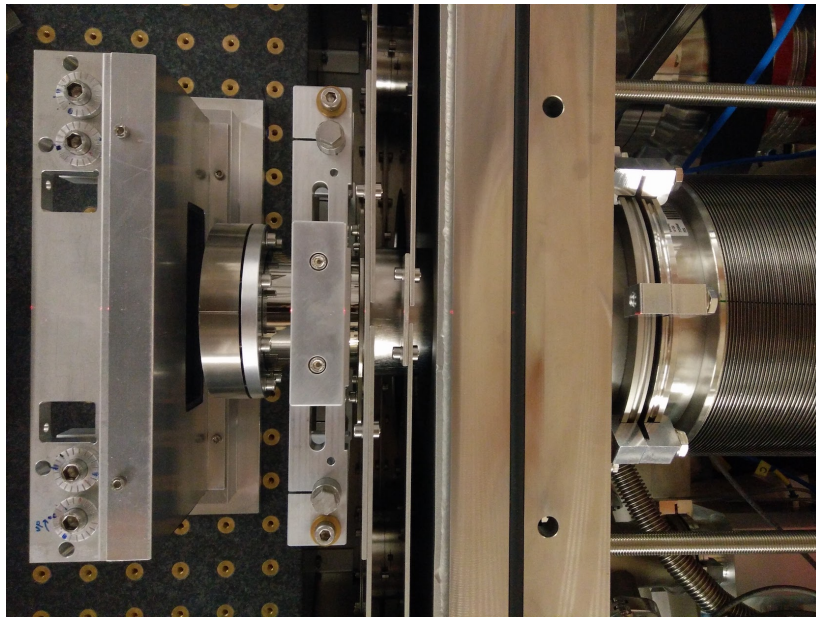
Figure A.2.: Top view on the entering of the neutron guide (from the right) through the flexible bellow, ending close to the velocity selector system mounted on the measurement granite. The double layer MuMetal and the adjustable beam guide holder, as well as the end cap on the glass beam guide can be seen.
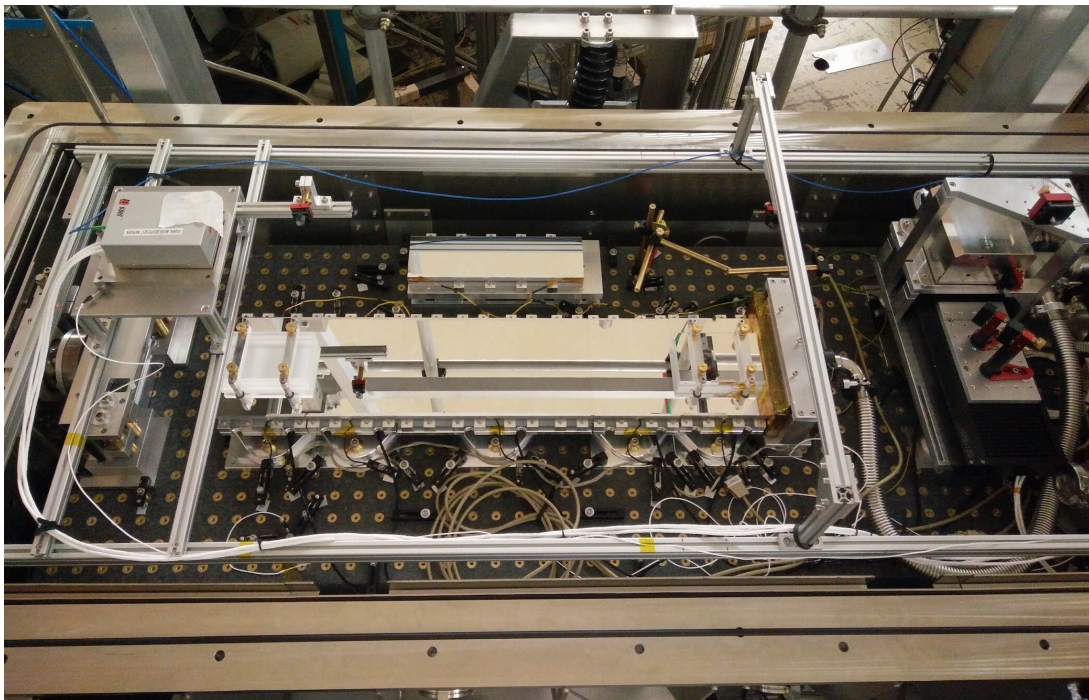
Figure A.3.: Five-part neutron mirror setup in Ramsey configuration within qBOUNCE. The large sensor gantry is missing in the photograph, offering a good view on the aligned mirror setup.

132
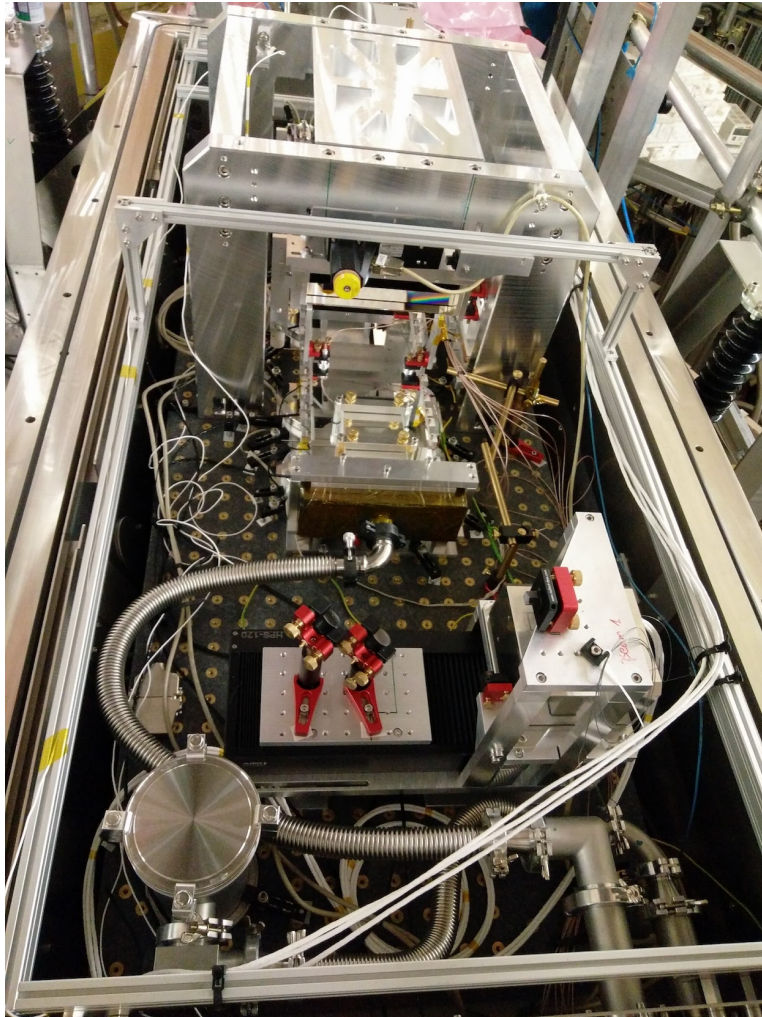
Figure A.4.: Usually, the sensor gantry covers most of the neutron mirrors.
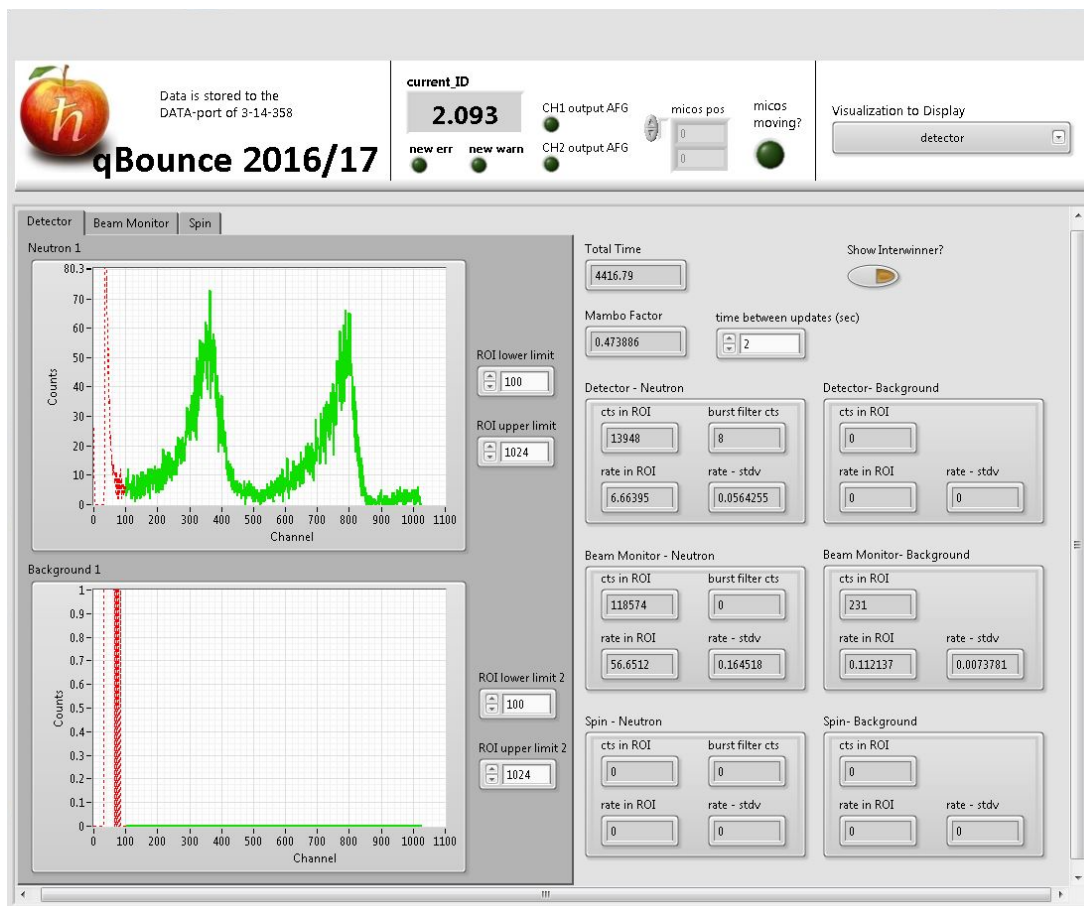
Figure A.5.: Exemplary screenshot of the LabVIEW visualisation of qBounce. Here, the detector tab is selected where the detector spectrum is updated continuously. A slight time delay is due to saving processing power, as there is no direct communication between detector and LabVIEW and the updates are generated by reading out detector text files. The detector was integrated into the visualisation in **Huber** (2017).

Bibliography

Abele, H., "The Neutron. Its Properties and Basic Interactions." *Progress in Particle and Nuclear Physics* 60 (2008), no. 1: 1–81. ISSN 0146-6410. doi: 10.1016/j.ppnp.2007.05.002.

Abele, H., S. Baeßler, and A. Westphal, "Quantum States of Neutrons in the Gravitational Field and Limits for Non-Newtonian Interaction in the Range between 1 μm and 10 μm." In D. J. W. Giulini, C. Kiefer, and C. Lämmerzahl, editors, *Quantum Gravity: From Theory to Experimental Search*, Lecture Notes in Physics, 355–366. Springer Berlin Heidelberg, Berlin, Heidelberg, 2003. ISBN 978-3-540-45230-0. doi:10.1007/978-3-540-45230-0_10.

Abele, H., T. Jenke, H. Leeb, and J. Schmiedmayer, "Ramsey's Method of Separated Oscillating Fields and Its Application to Gravitationally Induced Quantum Phase Shifts." *Physical Review D* 81 (2010), no. 6: 065019. doi: 10.1103/PhysRevD.81.065019.

Adam, R., P. a. R. Ade, N. Aghanim, Y. Akrami, M. I. R. Alves, F. Argüeso, M. Arnaud, F. Arroja, M. Ashdown, et al., "Planck 2015 Results - I. Overview of Products and Scientific Results." *Astronomy & Astrophysics* 594 (2016): A1. ISSN 0004-6361, 1432-0746. doi:10.1051/0004-6361/201527101.

Ahmed, S., E. Altiere, T. Andalib, B. Bell, C. Bidinosti, E. Cudmore, M. Das, C. Davis, B. Franke, et al., "First Ultracold Neutrons Produced at TRIUMF." *arXiv:1809.04071 [nucl-ex, physics:physics]* (2018).

Almasi, A., P. Brax, D. Iannuzzi, and R. I. P. Sedmik, "Force Sensor for Chameleon and Casimir Force Experiments with Parallel-Plate Configuration." *Physical Review D* 91 (2015), no. 10: 102002. doi:10.1103/PhysRevD.91.102002.

Baeßler, S., V. V. Nesvizhevsky, K. V. Protasov, and A. Y. Voronin, "Constraint on the Coupling of Axionlike Particles to Matter via an Ultracold Neutron Gravitational Experiment." *Physical Review D* 75 (2007), no. 7: 075006. doi:10.1103/PhysRevD.75.075006.

Banahene-Sabulsky, D., 2018. *Constraining Theories of Modified Gravity with Atom Interferometry.* Ph.D. thesis.

Baumann, J., R. Gähler, J. Kalus, and W. Mampe, "Experimental Limit for the Charge of the Free Neutron." *Physical Review D* 37 (1988), no. 11: 3107–3112. doi:10.1103/PhysRevD.37.3107.

Bibliography

Bison, G., M. Daum, K. Kirch, B. Lauss, D. Ries, P. Schmidt-Wellenburg, G. Zsigmond, T. Brenner, P. Geltenbort, et al., "Comparison of Ultracold Neutron Sources for Fundamental Physics Measurements." *Physical Review C* 95 (2017), no. 4: 045503. doi:10.1103/PhysRevC.95.045503.

Brax, P. and A.-C. Davis, "Atomic Interferometry Test of Dark Energy." *Physical Review D* 94 (2016), no. 10: 104069. doi:10.1103/PhysRevD.94.104069.

Brax, P. and S. Fichet, "Quantum Chameleons." *arXiv:1809.10166 [hep-ph]* (2018).

Brax, P. and M. Pitschmann, "Exact Solutions to Nonlinear Symmetron Theory: One- and Two-Mirror Systems." *Physical Review D* 97 (2018), no. 6: 064015. doi:10.1103/PhysRevD.97.064015.

Breit, G. and I. I. Rabi, "On the Interpretation of Present Values of Nuclear Moments." *Physical Review* 46 (1934), no. 3: 230–231. doi:10.1103/PhysRev.46.230.

Burrage, C., E. J. Copeland, and E. A. Hinds, "Probing Dark Energy with Atom Interferometry." *Journal of Cosmology and Astroparticle Physics* 2015 (2015), no. 03: 042. ISSN 1475-7516. doi:10.1088/1475-7516/2015/03/042.

Callin, P. and C. P. Burgess, "Deviations From Newton's Law in Supersymmetric Large Extra Dimensions." (2005). doi:10.1016/j.nuclphysb.2006.06.018.

Chadwick, J., "The Existence of a Neutron." *Proc. R. Soc. Lond. A* 136 (1932a), no. 830: 692–708. ISSN 0950-1207, 2053-9150. doi:10.1098/rspa.1932.0112.

——, "Possible Existance of a Neutron." *Nature* 129 (1932b): 312. doi:10.1038/129312a0.

Chastaing, J.-Y., E. Bertin, and J.-C. Géminard, "Dynamics of a Bouncing Ball." *American Journal of Physics* 83 (2015), no. 6: 518–524. ISSN 0002-9505, 1943-2909. doi:10.1119/1.4906418.

Chizhova, L. A., S. Rotter, T. Jenke, G. Cronenberg, P. Geltenbort, G. Wautischer, H. Filter, H. Abele, and J. Burgdörfer, "Vectorial Velocity Filter for Ultracold Neutrons Based on a Surface-Disordered Mirror System." *Physical Review E* 89 (2014), no. 3: 032907. doi:10.1103/PhysRevE.89.032907.

Clifton, T., P. G. Ferreira, A. Padilla, and C. Skordis, "Modified Gravity and Cosmology." *Physics Reports* 513 (2012), no. 1-3: 1–189. ISSN 03701573. doi:10.1016/j.physrep.2012.01.001.

Clowe, D., M. Bradač, A. H. Gonzalez, M. Markevitch, S. W. Randall, Christine Jones, and D. Zaritsky, "A Direct Empirical Proof of the Existence of Dark Matter." *The Astrophysical Journal Letters* 648 (2006), no. 2: L109. ISSN 1538-4357. doi:10.1086/508162.

Clowe, D., A. Gonzalez, and M. Markevitch, "Weak-Lensing Mass Reconstruction of the Interacting Cluster 1E 0657–558: Direct Evidence for the Existence of Dark Matter." *The Astrophysical Journal* 604 (2004), no. 2: 596. ISSN 0004-637X. doi:10.1086/381970.

Copeland, E. J., M. Sami, and S. Tsujikawa, "Dynamics of Dark Energy." *International Journal of Modern Physics D* 15 (2006), no. 11: 1753–1935. ISSN 0218-2718, 1793-6594. doi:10.1142/S021827180600942X.

Corbelli, E. and P. Salucci, "The Extended Rotation Curve and the Dark Matter Halo of M33." *Monthly Notices of the Royal Astronomical Society* 311 (2000), no. 2: 441–447. ISSN 0035-8711. doi:10.1046/j.1365-8711.2000.03075.x.

Cronenberg, G., 2016. *Frequency Measurements Testing Newton's Gravity Law with the Rabi-qBounce Experiment.* PhD Thesis, TU Wien.

Cronenberg, G., P. Brax, H. Filter, P. Geltenbort, T. Jenke, G. Pignol, M. Pitschmann, M. Thalhammer, and H. Abele, "Acoustic Rabi Oscillations between Gravitational Quantum States and Impact on Symmetron Dark Energy." *Nature Physics* (2018): 1. ISSN 1745-2481. doi:10.1038/s41567-018-0205-x.

Della Valle, G., M. Savoini, M. Ornigotti, P. Laporta, V. Foglietti, M. Finazzi, L. Duò, and S. Longhi, "Experimental Observation of a Photon Bouncing Ball." *Physical Review Letters* 102 (2009), no. 18: 180402. doi:10.1103/PhysRevLett.102.180402.

Döge, S., 2018. *Tba.* PhD Thesis, TU München, UGA Grenoble.

Dubbers, D. and M. G. Schmidt, "The Neutron and Its Role in Cosmology and Particle Physics." *Reviews of Modern Physics* 83 (2011): 1111–1171. ISSN 0034-6861. doi:10.1103/RevModPhys.83.1111.

Durstberger-Rennhofer, K., T. Jenke, and H. Abele, "Probing Neutron's Electric Neutrality with Ramsey Spectroscopy of Gravitational Quantum States of Ultra-Cold Neutrons." *Physical Review D* 84 (2011), no. 3. ISSN 1550-7998, 1550-2368. doi:10.1103/PhysRevD.84.036004.

Feichtinger, P., 2018. *Analyse der Stufenkontrolle des qBounce Experiments.* Bachelor Thesis, TU Wien.

Filter, H., 2018. *Interference Experiment with Slow Neutrons: A Feasibility Study of Lloyd's Mirror at the Institut Laue-Langevin.* PhD Thesis, TU Wien.

Fujii, Y., "Mass of the Dilaton and the Cosmological Constant." *Progress of Theoretical Physics* 110 (2003), no. 3: 433–439. ISSN 0033-068X. doi:10.1143/PTP.110.433.

Gibbs, R. L., "The Quantum Bouncer." *American Journal of Physics* 43 (1975), no. 1: 25–28. ISSN 0002-9505. doi:10.1119/1.10024.

Bibliography

Golub, R., D. J. Richardson, and S. K. Lamoreaux, *Ultra-Cold Neutrons.* Adam Hilger, IOP Publishing Ltd, Bristol, Philadelphia, New York, 1991. ISBN 0-7503-0115-5.

Golubich, R., 2017. *Analysis of the Velocity Spectra at the PF2 Located at the Institute Laue Langevin.* Project Thesis, TU Wien.

Gruber, A., 2016. *Automation of the qBounce Experiment's Vacuum System.* Bachelor Thesis, TU Wien.

Heiß, M., 2017. *Vorbereitung von Gravitationsexperimenten im Rahmen des qBounce-Experiments.* Master Thesis, TU Wien.

Heistracher, P., 2015. *Extension and Characterisation of the Neutron Detector within the qBounce Experiment.* Bachelor Thesis, TU Wien.

Herzinger, J., 2014. *Entwicklung einer Instrumentansteuerung für das qBounce Experiment.* Master Thesis, TU Wien.

Hinterbichler, K. and J. Khoury, "Screening Long-Range Forces through Local Symmetry Restoration." *Physical Review Letters* 104 (2010), no. 23: 231301. doi:10.1103/PhysRevLett.104.231301.

Huber, N., 2017. *Extending the Software Environment of the qBounce Platform.* Bachelor Thesis, TU Wien.

Ito, T. M., E. R. Adamek, N. B. Callahan, J. H. Choi, S. M. Clayton, C. Cude-Woods, S. Currie, X. Ding, D. E. Fellers, et al., "Performance of the Upgraded Ultracold Neutron Source at Los Alamos National Laboratory and Its Implication for a Possible Neutron Electric Dipole Moment Experiment." *Physical Review C* 97 (2018), no. 1: 012501. doi:10.1103/PhysRevC.97.012501.

Ivanov, A. N. and M. Wellenzohn, "Einstein–Cartan Gravity with Torsion Field Serving as an Origin for the Cosmological Constant or Dark Energy Density." *The Astrophysical Journal* 829 (2016a), no. 1: 47. ISSN 0004-637X. doi: 10.3847/0004-637X/829/1/47.

——, "Spin Precession of Slow Neutrons in Einstein-Cartan Gravity with Torsion, Chameleon, and Magnetic Field." *Physical Review D* 93 (2016b), no. 4: 045031. doi:10.1103/PhysRevD.93.045031.

Jaffe, M., P. Haslinger, V. Xu, P. Hamilton, A. Upadhye, B. Elder, J. Khoury, and H. Müller, "Testing Sub-Gravitational Forces on Atoms from a Miniature in-Vacuum Source Mass." *Nature Physics* 13 (2017), no. 10: 938–942. ISSN 1745-2481. doi:10.1038/nphys4189.

Jenke, T., 2008. *Weiterentwicklung eines Experiments zur Realisierung eines Quantum Bouncing Balls und Suche nach Extradimensionen der Raumzeit.* Master Thesis, Universität Heidelberg.

——, 2011. *qBounce - vom Quantum Bouncer zur Gravitationsresonanzspektroskopie.* PhD Thesis, TU Wien.

Jenke, T., G. Cronenberg, J. Burgdörfer, L. A. Chizhova, P. Geltenbort, A. N. Ivanov, T. Lauer, T. Lins, S. Rotter, H. Saul, U. Schmidt, and H. Abele, "Gravity Resonance Spectroscopy Constrains Dark Energy and Dark Matter Scenarios." *Physical Review Letters* 112 (2014), no. 15: 151105. doi:10.1103/PhysRevLett.112.151105.

Jenke, T., G. Cronenberg, H. Filter, P. Geltenbort, M. Klein, T. Lauer, K. Mitsch, H. Saul, D. Seiler, D. Stadler, M. Thalhammer, and H. Abele, "Ultracold Neutron Detectors Based on 10B Converters Used in the qBounce Experiments." *Nuclear Instruments & Methods in Physics Research. Section A, Accelerators, Spectrometers, Detectors and Associated Equipment* 732 (2013): 1–8. ISSN 0168-9002. doi:10.1016/j.nima.2013.06.024.

Jenke, T., P. Geltenbort, H. Lemmel, and H. Abele, "Realization of a Gravity-Resonance-Spectroscopy Technique." *Nature Physics* 7 (2011), no. 6: 468–472. ISSN 1745-2481. doi:10.1038/nphys1970.

Joyce, A., B. Jain, J. Khoury, and M. Trodden, "Beyond the Cosmological Standard Model." *Physics Reports* 568 (2015): 1–98. ISSN 0370-1573. doi:10.1016/j.physrep.2014.12.002.

Kahlenberg, J., D. Ries, K. U. Ross, C. Siemensen, M. Beck, C. Geppert, W. Heil, N. Hild, J. Karch, et al., "Upgrade of the Ultracold Neutron Source at the Pulsed Reactor TRIGA Mainz." *The European Physical Journal A* 53 (2017), no. 11. ISSN 1434-6001, 1434-601X. doi:10.1140/epja/i2017-12428-9.

Kapner, D. J., T. S. Cook, E. G. Adelberger, J. H. Gundlach, B. R. Heckel, C. D. Hoyle, and H. E. Swanson, "Tests of the Gravitational Inverse-Square Law below the Dark-Energy Length Scale." *Physical Review Letters* 98 (2007), no. 2: 021101. doi:10.1103/PhysRevLett.98.021101.

Khoury, J. and A. Weltman, "Chameleon Cosmology." *Physical Review D* 69 (2004), no. 4: 044026. doi:10.1103/PhysRevD.69.044026.

Kwan, J., C. Sánchez, J. Clampitt, J. Blazek, M. Crocce, B. Jain, J. Zuntz, A. Amara, M. R. Becker, et al., "Cosmology from Large-Scale Galaxy Clustering and Galaxy–Galaxy Lensing with Dark Energy Survey Science Verification Data." *Monthly Notices of the Royal Astronomical Society* 464 (2017), no. 4: 4045–4062. ISSN 0035-8711. doi:10.1093/mnras/stw2464.

Lamoreaux, S. K. and R. Golub, "Experimental Searches for the Neutron Electric Dipole Moment." *Journal of Physics G: Nuclear and Particle Physics* 36 (2009), no. 10: 104002. ISSN 0954-3899. doi:10.1088/0954-3899/36/10/104002.

Bibliography

Landau, L. D. and E. M. Lifshitz, *Quantum Mechanics Non-Relativistic Theory, Third Edition: Volume 3.* Butterworth-Heinemann, Oxford, 1981, 3rd edition. ISBN 978-0-08-029140-6.

Langhoff, P. W., "Schrödinger Particle in a Gravitational Well." *American Journal of Physics* 39 (1971), no. 8: 954–957. ISSN 0002-9505. doi:10.1119/1.1986333.

Lauss, B., "Ultracold Neutron Production at the Second Spallation Target of the Paul Scherrer Institute." *Physics Procedia* 51 (2014): 98–101. ISSN 1875-3892. doi:10.1016/j.phpro.2013.12.022.

Leung, K. K. H., S. Ivanov, F. M. Piegsa, M. Simson, and O. Zimmer, "Ultracold-Neutron Production and up-Scattering in Superfluid Helium between 1.1 K and 2.4 K." *Physical Review C* 93 (2016), no. 2: 025501. doi:10.1103/PhysRevC.93.025501.

LIGO and Virgo Collaboration, B. P. Abbott, R. Abbott, T. D. Abbott, M. R. Abernathy, F. Acernese, K. Ackley, C. Adams, T. Adams, et al., "Observation of Gravitational Waves from a Binary Black Hole Merger." *Physical Review Letters* 116 (2016), no. 6: 061102. doi:10.1103/PhysRevLett.116.061102.

Luschikov, V. and A. Frank, "Quantum Effects Occuring When Ultracold Neutrons Are Stored on a Plane." *Journal of Experimental and Theoretical Physics Letters* 28 (1978), no. 9: 559.

Luschikov, V. I., Y. N. Pokotilovskii, A. V. Strelkov, and F. L. Shapiro, "Observation of Ultracold Neutrons." *Journal of Experimental and Theoretical Physics* 9 (1969), no. 1: 23.

Manfredi, G., O. Morandi, L. Friedland, T. Jenke, and H. Abele, "Chirped-Frequency Excitation of Gravitationally Bound Ultracold Neutrons." *Physical Review D* 95 (2017), no. 2. ISSN 2470-0010, 2470-0029. doi:10.1103/PhysRevD.95.025016.

Mantry, S., M. Pitschmann, and M. J. Ramsey-Musolf, "Distinguishing Axions from Generic Light Scalars Using Electric Dipole Moment and Fifth-Force Experiments." *Physical Review D* 90 (2014), no. 5: 054016. doi:10.1103/PhysRevD.90.054016.

Mayr, S., 2016. *Nivellierung des qBounce-Experimentes.* Project Thesis, TU Wien.

Moody, J. E. and F. Wilczek, "New Macroscopic Forces?" *Physical Review D* 30 (1984), no. 1: 130–138. doi:10.1103/PhysRevD.30.130.

Mota, D. F. and D. J. Shaw, "Evading Equivalence Principle Violations, Cosmological, and Other Experimental Constraints in Scalar Field Theories with a Strong Coupling to Matter." *Physical Review D* 75 (2007), no. 6: 063501. doi:10.1103/PhysRevD.75.063501.

Nesvizhevsky, V. V., "Gravitational Quantum States of Neutrons and the New Granit Spectrometer." *Modern Physics Letters A* 27 (2012), no. 05: 1230006. ISSN 0217-7323. doi:10.1142/S0217732312300066.

Nesvizhevsky, V. V., H. G. Börner, A. M. Gagarski, A. K. Petoukhov, G. A. Petrov, H. Abele, S. Baeßler, G. Divkovic, F. J. Rueß, T. Stöferle, A. Westphal, A. V. Strelkov, K. V. Protasov, and A. Y. Voronin, "Measurement of Quantum States of Neutrons in the Earth's Gravitational Field." *Physical Review D* 67 (2003), no. 10: 102002. doi:10.1103/PhysRevD.67.102002.

Nesvizhevsky, V. V., H. G. Börner, A. K. Petukhov, H. Abele, S. Baeßler, F. J. Rueß, T. Stöferle, A. Westphal, A. M. Gagarski, G. A. Petrov, and A. V. Strelkov, "Quantum States of Neutrons in the Earth's Gravitational Field." *Nature* 415 (2002), no. 6869: 297. ISSN 1476-4687. doi:10.1038/415297a.

Nesvizhevsky, V. V., A. K. Petukhov, H. G. Börner, T. A. Baranova, A. M. Gagarski, G. A. Petrov, K. V. Protasov, A. Y. Voronin, S. Baeßler, H. Abele, A. Westphal, and L. Lucovac, "Study of the Neutron Quantum States in the Gravity Field." *The European Physical Journal C - Particles and Fields* 40 (2005), no. 4: 479–491. ISSN 1434-6052. doi:10.1140/epjc/s2005-02135-y.

Nesvizhevsky, V. V. and K. V. Protasov, "Constraints on Non-Newtonian Gravity from the Experiment on Neutron Quantum States in the Earth's Gravitational Field." *Classical and Quantum Gravity* 21 (2004), no. 19: 4557. ISSN 0264-9381. doi:10.1088/0264-9381/21/19/005.

Neuhuber, P., 2017. *Improvement of the Displacement Regulation Program for the Neutron Mirrors of the qBounce Experiment Series.* Bachelor Thesis, TU Wien.

Patrignani, C. and P. D. Group, "Review of Particle Physics." *Chinese Physics C* 40 (2016), no. 10: 100001. ISSN 1674-1137. doi:10.1088/1674-1137/40/10/100001.

Peccei, R. D. and H. R. Quinn, "CP Conservation in the Presence of Pseudoparticles." *Physical Review Letters* 38 (1977), no. 25: 1440–1443. doi:10.1103/PhysRevLett.38.1440.

Peebles, P. J. E., "Large-Scale Background Temperature and Mass Fluctuations Due to Scale-Invariant Primeval Perturbations." *The Astrophysical Journal* 263 (1982): L1–L5. ISSN 0004-637X. doi:10.1086/183911.

Pendlebury, J. M., S. Afach, N. J. Ayres, C. A. Baker, G. Ban, G. Bison, K. Bodek, M. Burghoff, P. Geltenbort, et al., "Revised Experimental Upper Limit on the Electric Dipole Moment of the Neutron." *Physical Review D* 92 (2015), no. 9: 092003. doi:10.1103/PhysRevD.92.092003.

Pitschmann, M., 2018. "Remarks on qBounce, Unplublished Notes."

Bibliography

Rabi, I. I., S. Millman, P. Kusch, and J. R. Zacharias, "The Molecular Beam Resonance Method for Measuring Nuclear Magnetic Moments. The Magnetic Moments of 3Li6, 3Li7 and 9F19." *Physical Review* 55 (1939), no. 6: 526–535. doi:10.1103/PhysRev.55.526.

Raffelt, G. G., "Axions—Motivation, Limits and Searches." *Journal of Physics A: Mathematical and Theoretical* 40 (2007), no. 25: 6607. ISSN 1751-8121. doi:10.1088/1751-8113/40/25/S05.

Ramsey, N. F., "A New Molecular Beam Resonance Method." *Physical Review* 76 (1949), no. 7: 996.

——, "A Molecular Beam Resonance Method with Separated Oscillating Fields." *Physical Review* 78 (1950), no. 6: 695.

——, *Molecular Beams.* Oxford University Press, 1986. ISBN 978-0-19-170632-5.

Rath, D., 2016. *Weiterentwicklung des Blendensystems für das qBounce Experiment.* Bachelor Thesis, TU Wien.

Reiter, R., B. Schlederer, and D. Seppi, 2009. *Quantenmechanisches Verhalten eines ultrakalten Neutrons im Gravitationsfeld.* Project Thesis, TU Wien.

Riehle, F., *Frequency Standards: Basics and Applications.* WILEY-VCH Verlag GmbH & Co. KGaA, Weinheim, 2004. ISBN 3-527-40230-6.

Schmidt, P., 2017. *Studien zur Ramsey-Spektroskopie ultrakalter Neutronen im Rahmen des qBounce Experiments.* Master Thesis, TU Wien.

Smith, J. H., E. M. Purcell, and N. F. Ramsey, "Experimental Limit to the Electric Dipole Moment of the Neutron." *Physical Review* 108 (1957), no. 1: 120–122. doi:10.1103/PhysRev.108.120.

Stangl, H.-G., 2016. *Characterisation of the Vacuum System of the qBounce Experiment.* Bachelor Thesis, TU Wien.

Steyerl, A., "Measurements of Total Cross Sections for Very Slow Neutrons with Velocities from 100 m/Sec to 5 m/Sec." *Phys.Lett.* 29B (1969): 33–35. doi:10.1016/0370-2693(69)90127-0.

——, "A "neutron Turbine" as an Efficient Source of Ultracold Neutrons." *Nuclear Instruments and Methods* 125 (1975): 461–469. doi:10.1016/0029-554X(75)90265-7.

Steyerl, A., H. Nagel, F. X. Schreiber, K. A. Steinhauser, R. Gähler, W. Gläser, P. Ageron, J. M. Astruc, W. Drexel, G. Gervais, and W. Mampe, "A New Source of Cold and Ultracold Neutrons." *Physics Letters A* 116 (1986), no. 7: 347–352. ISSN 0375-9601. doi:10.1016/0375-9601(86)90587-6.

Thalhammer, M., 2013. *Optimierung Der Detektorsignalverarbeitung Des Gravitationsexperiments qBounce.* Master Thesis, TU Wien.

——, 2019. *Tba.* PhD Thesis, TU Wien.

The ATLAS Collaboration, "Observation of a New Particle in the Search for the Standard Model Higgs Boson with the ATLAS Detector at the LHC." *Physics Letters B* 716 (2012), no. 1: 1–29. ISSN 03702693. doi:10.1016/j.physletb.2012.08.020.

Tisserand, P., L. L. Guillou, C. Afonso, J. N. Albert, J. Andersen, R. Ansari, E. Aubourg, P. Bareyre, J. P. Beaulieu, et al., "Limits on the Macho Content of the Galactic Halo from the EROS-2 Survey of the Magellanic Clouds." *Astronomy & Astrophysics* 469 (2007), no. 2: 387–404. ISSN 0004-6361, 1432-0746. doi:10.1051/0004-6361:20066017.

Wallis, H., J. Dalibard, and C. Cohen-Tannoudji, "Trapping Atoms in a Gravitational Cavity." *Applied Physics B: Lasers and Optics* 54 (1992): 407–419. ISSN 0946-2171. doi:10.1007/BF00325387.

Wautischer, G., 2015. *Realisation of Quantum Transport Measurements with UCNs within the qBounce Project.* Master Thesis, TU Wien.

Westphal, A., H. Abele, S. Baeßler, V. Nesvizhevsky, K. Protasov, and A. Voronin, "A Quantum Mechanical Description of the Experiment on the Observation of Gravitationally Bound States." *The European Physical Journal C* 51 (2007), no. 2: 367–375. ISSN 1434-6052. doi:10.1140/epjc/s10052-007-0283-x.

Wietfeldt, F. E. and G. L. Greene, "Colloquium: The Neutron Lifetime." *Reviews of Modern Physics* 83 (2011), no. 4: 1173–1192. doi:10.1103/RevModPhys.83.1173.

Will, C. M., *Theory and Experiment in Gravitational Physics.* 1993.

Zel'dovich, Y. B., "Storage of Cold Neutrons." *Journal of Experimental and Theoretical Physics* 9 (1959), no. 6: 1389–1390.

Zwicky, F., "Die Rotverschiebung von Extragalaktischen Nebeln." *Helvetica Physica Acta* 6 (1933): 110–127. ISSN 0018-0238.

Acknowledgements

Curriculum Vitae

Name	**Tobias Rechberger**
Date/Place of Birth	September 9th 1987, A-2620 Neunkirchen
Nationality	Austrian
Address	Stiegengasse 9/19, A-1060 Vienna
Mobile	+43676 72 95 722
Email	tobias.rechberger@gmail.com

Education

since 2014   **Doctoral Thesis** at Atominstitut TU Wien

Member of the doctoral program particles & interactions

2010 – 2013   **Master's degree** in technical physics, TU Wien

Thesis title: "Untersuchung von Ultrakleinwinkelstreuung an magnetischen Mikrostrukturen mit polarisierten Neutronen"

2011 – 2012   Exchange Semester at Loughborough University, United Kingdom

2006 – 2010   **Bachelor's degree** in technical physics, TU Wien

1998 – 2006   BG Zehnergasse, Wiener Neustadt, Austria

Grammar school with special emphasis on sports

Publications

T. Jenke, G. Cronenberg, M. Thalhammer, T. Rechberger, P. Geltenbort, H. Abele "Gravity experiments with ultracold neutrons and the qBounce experiment" arXiv: 1510.03078v1 [physics.ins-det]

Ch. Gösselsberger, H. Abele, G. Badurek, E. Jericha, W. Mach, S. Nowak, T. Rechberger: "*Neutron beam tailoring by means of a novel pulsed spatial magnetic spin resonator*", Journal of Physics: Conference Series, 340 (2012) 012028; 1 - 8.